# LARGE AREA PLASMONIC NANOSTRUCTURES DESIGN, FABRICATION AND CHARACTERIZATION BY LASER

**XU LE**

**NATIONAL UNIVERSITY OF SINGAPORE**

**2014**

# LARGE AREA PLASMONIC NANOSTRUCTURES DESIGN, FABRICATION AND CHARACTERIZATION BY LASER

**XU LE**

(*M. Eng, Xi'an Jiaotong University*)

**A THESIS SUBMITTED**

**FOR THE DEGREE OF DOCTOR OF PHILOSOPHY**
**DEPARTMENT OF ELECTRICAL AND COMPUTER ENGINEERING**
**NATIONAL UNIVERSITY OF SINGAPORE**

**2014**

# DECLARATION

I hereby declare that the thesis is my original work and it has been written by me in its entirety.

I have duly acknowledged all the sources of information which have been used in the thesis.

This thesis has also not been submitted for any degree in any university previously.

Xu Le

6th January 2014

# ACKNOWLEDGEMENTS

It would not have been possible to write this doctoral thesis without the help and support of kind people around me, to only some of whom it is possible to give particular mention here.

First and foremost I would like to express my sincere gratitude to my supervisors, Prof. Hong Minghui and Prof. Tan Leng Seow, for their invaluable guidance and great supports throughout my Ph.D. program. Without their persistent helps, this dissertation would not have been possible. In particular, I am truly thankful to Prof. Hong Minghui for his contributions of time, ideas, and the funding to make my Ph.D. experience productive and stimulating. His passion for the research inspires me, even during tough time in my Ph.D. pursuit.

I would also like to thank my colleagues, Dr. Ng Doris, Dr. Zhou Yi, Dr. Lin Ying, Dr. Huang Zhiqiang, Mr. Teo Honghai, Dr. Tang Min, Dr. Pan Zhenying, Dr. Yang Lanying, Dr. Liu Yan, Dr. Li Xiong, Dr. Zhang Ziyue, Mr. Chen Yiguo, Mr. Yang Jing, and Mr. Wang Dacheng. The group has been a source of the friendship as well as good advice and collaborations. I am especially grateful for Ms. Liu Caihong, Dr. Nguyen Thi Van Thanh, and Dr. Lim Chin Seong, who gave me precious experimental experience that I never touched before. I would like to acknowledge Mr. Ng Binghao, Dr. Chen Zaichun, Dr. Mohsen Rahmani, Dr. Kao Tsung Sheng, and Dr. Zhong Xiaolan, who offered insightful discussions on my research.

I gratefully acknowledge the funding source that makes my Ph.D. work possible. My scholarship was funded by National University of Singapore for four years.

Much of the research involved in this Ph.D. project is greatly relied on collaborations with many scientists from National University of Singapore (NUS), Data Storage Institute (DSI), National University Health System (NUHS), and Chinese Academy of Sciences (CAS). I would like to express my greatest thankful to my advisor Prof. Hong Minghui again who helped me to be attached to DSI as a research scholar, allowing me to access advanced equipment. Thanks should also be given to Dr. Ding Tao and Prof. Chester Lee Drum of NUHS for kind supports on microfluid chamber and materials.

My time at NUS was made enjoyable in large part due to many friends and groups that have become a part of my life. I am grateful for time spent with my roommates and friends, for my backpacking buddies, and for many other people and memories. Lastly, I am deeply thankful to my parents for giving birth to me at the first place and supporting me spiritually throughout my life. Their loves provide my inspirations and are my driving force to pursue my dreams.

*6th January 2014*

# TABLE OF CONTENTS

# SUMMARY

Plasmonics has recently been the subject of intense research efforts, owing to the fact that the strong optical interactions can be effectively confined in metallic nanostructures at nanoscale. The highly intense electromagnetic fields achieved by free electron oscillations at the metal surface can provide promising applications, of which plasmonic sensing is a prime example. However, the development of practical, low-cost nanoscale manufacturing tools and processes capable of realizing these advanced applications is still one of the greatest challenges, which hinders the pace of transfer from laboratory to the real fabrication in industry. Therefore, this thesis aims to design and fabricate desirable nanostructures over a large area by low-cost and flexible nanofabrication methods to accomplish and improve sensing sensitivities of plasmonic bio/chemical nanosensors.

This thesis involves theoretical and experimental studies of optical properties and near-field enhancement from random nanoparticles, quasi-ordered nanoparticles, and periodic arrays of nanostructures for plasmonic sensing, consisting of refractive index sensing and surface enhanced Raman spectroscopy (SERS). These nanostructures are patterned by low-cost and high-efficient nanofabrication tools: thermal annealing and laser interference lithography (LIL).

The fabrication and characterization of disordered nanodot array are investigated. The experimental results confirm that the nanodots formed by thermal annealing can excite localized surface plasmon resonances (LSPR),

whose resonance wavelength in the UV-Visible range can be flexibly tuned by the Au concentration in the Ag/Au nanodots. The uniformity of both size dimension and particle distribution of the nanodots can be improved by a novel hybrid nanofabrication technique that is a combination of LIL and thermal annealing. The fabricated nanodot array can provide higher refractive index sensitivity than that of nanodots formed only by thermal annealing. Moreover, LSPR of Ag/Au nanodot array can be also flexibly tuned by proper control of the Au concentration, which can achieve further enhancement in the Raman intensity of the molecule R6G, arising from the resonance wavelength of nanodot array matching well with the excitation wavelength of the laser and overlapping with an electronic absorption band of interest.

Finally, this thesis demonstrated the design and fabrication of a periodic array of Au nanorods that can produce an intense local electric field driven by the diffractive coupling of dipoles as a result of the enhancement in the refractive index sensitivities. The surface lattice resonance (SLR) of nanorod array is selected by the light polarization, which is confirmed both by simulation and experiment with a good agreement. The refractive sensing performance is predicted by FDTD simulation that is subsequently verified by the detailed experiment. In particular, the influence of varying the lattice constant of nanorod array is investigated theoretically and experimentally. It is found that SLR and LSPR can be dramatically tuned by the lattice constant of nanorod array for the further improvement of the refractive index sensitivity with an optimized distance between the nanorods.

# LIST OF FIGURES

# LIST OF TABLES

# LIST OF ABBREVIATIONS

| | | | |
|---|---|---|---|
| **2D** | Two-dimensional | **EIT** | Extraordinary induced transmission |
| **3D** | Three-dimensional | **EM** | Electromagnetic |
| **AFM** | Atomic force microscope | **FDTD** | Finite-difference time-domain |
| **Ag** | Silver | **FES** | Field emission source |
| **ATR** | Attenuated total reflection | **FESEM** | field emission scanning electron microscope |
| **Au** | Gold | **FIB** | Focused ion beam |
| **CD** | Coupled dipole | **FRET** | Forster resonance energy transfers |
| **Cr** | Chromium | **FTIR** | Fourier-transform infrared spectroscopy |
| **Cu** | Copper | **FWHM** | Full width at half maximum |
| **CW** | Continuous wave | **He-Cd** | Helium cadmium |
| **DDA** | Discrete dipole approximation | **HMDS** | Hexamethyldisilzane |
| **DI** | De-ionized water | **InGaAs** | Indium gallium arsenide |
| **EBL** | Electron beam lithography | **IPA** | Isopropyl alcohol |

| | | | |
|---|---|---|---|
| **ITO** | Indium tin oxide | **SEM** | Scanning electron microscope |
| **LIL** | Laser interference lithography | **SERS** | Surface enhanced Raman spectroscopy |
| **LSP** | Localized surface plasmons | **$SiO_2$** | Silicon dioxide |
| **LSPR** | Localized surface plasmon resonances | **SLR** | Surface lattice resonance |
| **$N_2$** | Nitrogen gas | **SNOM** | Scanning near-field optical microscope |
| **NIR** | Near-infrared | **SP** | Surface plasmon |
| **PML** | Perfectly matched layers | **SPP** | Surface plasmon polaritons |
| **PVB** | Polyvinyl butyral | **SPR** | Surface plasmon resonances |
| **R6G** | Rhodamine 6G | **TERS** | Tip-enhanced Raman spectroscopy |
| **RI** | Refractive index | **$TiO_2$** | Titanium dioxide |
| **RIE** | Reactive-ion etching | **UV** | Ultraviolet |
| **RIU** | Refractive index unit | **VASE** | Variable-angle spectroscopic ellipsometry |

# LIST OF SYMBOLS

| | | | |
|---|---|---|---|
| $a$ | Radius of the metallic nanosphere | $\varepsilon_{media}$ | Dielectric constant of the medium surrounding the nanosphere |
| $a_x$ | Lattice period along the *x* direction | $\varepsilon_r$ | Real part of the metal dielectric function |
| $a_y$ | Lattice period along the *y* direction | $\varepsilon_\infty$ | Permittivity of ionic background in the metal |
| $\alpha$ | Rotation angle | $I_r$ | Intensity of the beam spot |
| $c_{ij}$ | Dipolar interaction matrix without the phase term | $k_{in}$ | Incident wave vectors |
| $e$ | Free electron charge | $k_{out}$ | Scattered wave vectors |
| $E_0$ | Amplitude of the applied electric field | $k_x'$ | SPP wavelength |
| $E(\omega)$ | Local electric field enhancement factor at the incident frequency ω | $k_x''$ | Damping of the SPP |
| $\lvert E(\omega)\rvert'$ | Factor at the Stokes shifted frequency \|ω\|' | $m$ | Integer of the grating |
| $\varepsilon_d$ | Permittivity of the dielectric | $m_e$ | Effective free electron mass |
| $\varepsilon_i$ | Imaginary part of the metal dielectric function | $N$ | Total number of particles |
| $\varepsilon_m$ | Permittivity of the metal | $N_A$ | Real density of the nanoparticles |

| | | | |
|---|---|---|---|
| $n_m$ | Refractive index of the surrounding media | $\delta$ | Skin depth |
| $P_x$ | Lattice period along the short axis of the nanorod | $\varphi$ | Phase difference between two beams |
| $P_y$ | Lattice period along the long axis of the nanorod | $\Lambda$ | Period of the standing waves |
| $r_{ij}$ | Distance between the $i_{th}$ and $j_{th}$ particles | $\lambda$ | Wavelength |
| $r_s$ | Electron gas parameter | $\lambda_{max}$ | Wavelength of resonance |
| $\gamma_d$ | Collision frequency | $\lambda_p$ | Wavelength corresponding to the plasma frequency of the bulk metal |
| $S$ | Refractive index sensitivity | $\lambda_0$ | Excitation wavelength |
| $\omega$ | Frequency | $\lambda_1$ | Raman spectral wavelength |
| $\omega_p$ | Volume or bulk plasmon frequency | $\lambda_g$ | Transition wavelength |
| $\Delta\omega$ | Raman shift | $\lambda_{SLR}$ | Wavelength of surface lattice resonance |
| $\theta_1$ | Angle between the normal of the exposed surface and the beam 1 | | |

# LIST OF PUBLICATIONS

1. **Le Xu**, L. S. Tan, and M. H. Hong, "Tuning of localized surface plasmon resonance of well-ordered Ag/Au bimetallic nanodot arrays by laser interference lithography and thermal annealing", Appl. Opt. **50**, G74-G79 (2011).
2. **Le Xu**, F. F. Luo, L. S. Tan, X. G. Luo, M. H. Hong, "Hybrid plasmonic structures: design and fabrication by laser means", IEEE J. Sel. Topics Quantum Electron. **19**, 4600309 (2013).
3. **L. Xu**, C. H. Liu, H. W. Cheung, L. S. Tan, and M. H. Hong, "Flexible tuning surface plasmon resonance of metallic nanostructures fabricated by colloidal lithography", AIP Conf. Proc. **1328**, 19-23 (2011).

# Chapter 1 Introduction

## 1.1. Research background and literature review

Plasmonics has recently been the subject of intense research efforts, owing to the fact that the light can be controlled and manipulated on the length scales far below the wavelength [1]. This phenomenon arises from the excitation of surface plasmons (SP), which are collective charge oscillations occurring at the interface between a metal and a dielectric. They can take various forms, ranging from freely propagating electron density waves along metal surfaces to localized electron oscillations on metal nanoparticles [2]. Their unique properties enable a wide range of practical applications, including light guiding and manipulation at the nanoscale [3], near-field optical imaging below the diffraction limit [4], plasmonic light-emitting device [5], bio/chemical sensing [6], and medical therapy [7].

The modeling, making and measuring of noble metal nanostructures have recently become three key factors to the development of plasmonics. In particular, theoretical tools, including optimized electrodynamics calculation methods and improved computational resonances, are able to describe and predict the possible optical properties. The nanofabrication tools capable of generating the desirable nanostructures with sub-100 nm resolution have played an essential role to explore the new properties of surface plasmons. Characterization tools, such as near-field scanning optical microscope and dark-field microscope, have enabled us to directly observe surface plasmon

polariton waves or detect optical properties of tiny nanoparticles. Therefore, a chain process consisting of simulation-fabrication-characterization steps could be a feasible approach to investigate the potential functionalized plasmonic nanostructures whose working principle has been theoretically predicted, optimized and experimentally investigated.

Among these steps, extensive efforts have been devoted by various research groups around the world to the quest for high efficiency and low cost fabrication tools to pattern nanostructures over a large area, as the ability to achieve large-scale nanostructures through such patterning techniques is essential to practical industrial applications. The significance of large-scale and economical nanopatterning is that it provides numerous opportunities to transfer the technology from laboratory to the real fabrication industry. In particular, large-scale plasmonic nanostructures can provide the effective area large enough for characterization using common spectroscopes, resulting in a simplified configuration to excite or detect surface plasmons without employing dark-field microscope or highly sensitivity spectroscope. Moreover, using straightforward and economical nanopatterning tools to mass produce these nanostructures has a major impact in the field of industries, such as solar energy, bio/chemical sensing or medical therapy.

In this thesis, attention will be placed on the design of simple and easily fabricated structures' parameters, and the experimental implementations of these nanostructures using high-efficiency and low-cost nanofabrication tools. These nanostructures have unique optical properties through the excitation of surface plasmons for potential applications.

### 1.1.1. Overview of plasmonics and surface plasmons

Before scientists start to study the unique optical properties of metallic nanostructures, they were firstly employed by artists to generate the vibrant colors in glass artifacts. One of the most famous examples is the Lycurgus cup [8] dating back to the Byzantine Empire (4th century AD). The glass cup shows a striking red color when viewed in transmitted light, but it appears green color in reflected light. This distinct color variation is theoretically and experimentally investigated since the beginning of the twentieth century in which the first scientific studies of surface plasmon (SP) began. The first observation of SP is Robert Wood [9] who described unexplained optical reflection measurements on a metallic grating in 1902. Two years later, bright colors in metal-doped glasses were discovered by Maxwell Garnett [10], and their electromagnetic properties were derived by Mie [11] in the theory of light scattering by small spherical particles. In the year 1956, David Pines [12] theoretically described energy losses experienced by fast electrons travelling through metals, and attributed these losses to collective oscillations of free electrons in the metal. By comparison to earlier works on plasma oscillations in gas discharges, he defined these oscillations as ‘plasmons’. In 1957, Rufus Ritchie [13] presented a result of electron energy losses in thin films demonstrating the existence of plasmon mode near the surface of metal. This study represents the first theoretical description of surface plasmons. In 1958, John Joseph [14] introduced the term ‘polariton’ for the coupled oscillations of bound electrons and the light inside transparent media. In 1968, Rufus Ritchie [15] and coworkers explained the anomalous behavior of metal gratings, and

attributed it to the excitation of surface plasmon resonances on the gratings. A major contribution to the study of surface plasmons was made in 1968 when Andreas Otto [16] and Erich Kretschmann [17] demonstrated methods for the optical excitations of surface plasmons on metal films, making experiments on surface plasmons easily accessible to many researchers.

Surface plasmon resonances have become one of the most attractive research areas, enabling numerous fundamental studies and applications in a variety of disciplines [1-7]. In general, it has been shown that surface plasmon polaritons (SPP) can exist as propagating waves on planar metal films with amplitudes that extend further into the dielectric region compared with the metal region (Fig. 1.1 (a)). Metal particles can also interact strongly with light, and their plasmon resonances are confined within tens of nanometers of the particle surface. These resonant optical fields are called localized surface plasmons (LSP) (Fig. 1.1 (b)). These resonances are highly sensitive to the size, shape, and dielectric environment of the metal particles, thus providing the potentials to tune the resonances from ultraviolet (UV) to near-infrared (NIR) wavelengths [18,19].

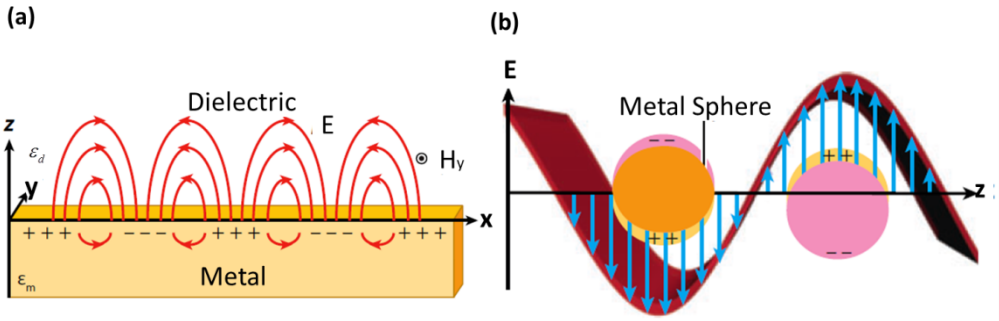


Figure 1.1 (a) Surface plasmon polaritons at a metal-dielectric interface and (b) localized surface plasmons on metal nanoparticles excited by free-space light. [19]

Localized plasmon resonances in small metallic nanostructures have attracted large interests in the scientific community for over a century, due to their capabilities of supporting collective electron oscillations (plasmons) at nanoscale [20]. The ability to spectrally tune resonance wavelengths, narrow spectral linewidth and confine the electromagnetic fields at the length scales much smaller than the optical diffraction limit remains challenging issues yet to be overcome [21]. This is an issue of particular importance since sensing sensitivity of nanosensors can be improved by the highly confined local field [22] and tuning localized surface plasmon resonances (LSPR) wavelength of nanostructures to a specific range can further enhance the Raman signals of the molecules [23]. Thus extensive research efforts have been established to investigate the interaction of light with single and coupled nanoparticles as well as a periodic array of nanoparticles.

The geometric structure control of nanostructures is one of the most straightforward strategies to tune the resonance spectra. It has been shown that fine tuning LSPR wavelength can be achieved by good control of the aspect ratio of nanorod using thermal reshaping technique in aqueous media [24]. The shape of the nanorod can be gradually transformed from a sphere to a rod with an increase in annealing time, leading to a continuous tuning of the longitudinal plasmon resonance wavelengths from 560 to 800 nm. Another example of tuning LSPR is to chemically synthesis a series of gradual variation in size dimension of gold nanospheres and nanorods [25], showing an intense red color (for particle less than 100 nm) or a yellowish color (for larger particles) in aqueous solution (Fig. 1.2). These interesting optical properties of the gold nanoparticles arise from the excitation of LSPR. The

LSPR wavelength of the gold nanospheres shifts towards a longer wavelength in the absorption spectra with an increase in the nanosphere size. Another report presents the result of the synthesis of gold-silica core shell particles demonstrating that the optical properties of core-shell can be adjusted by tuning the thickness of the silica layer outside the gold nanoparticles [26].

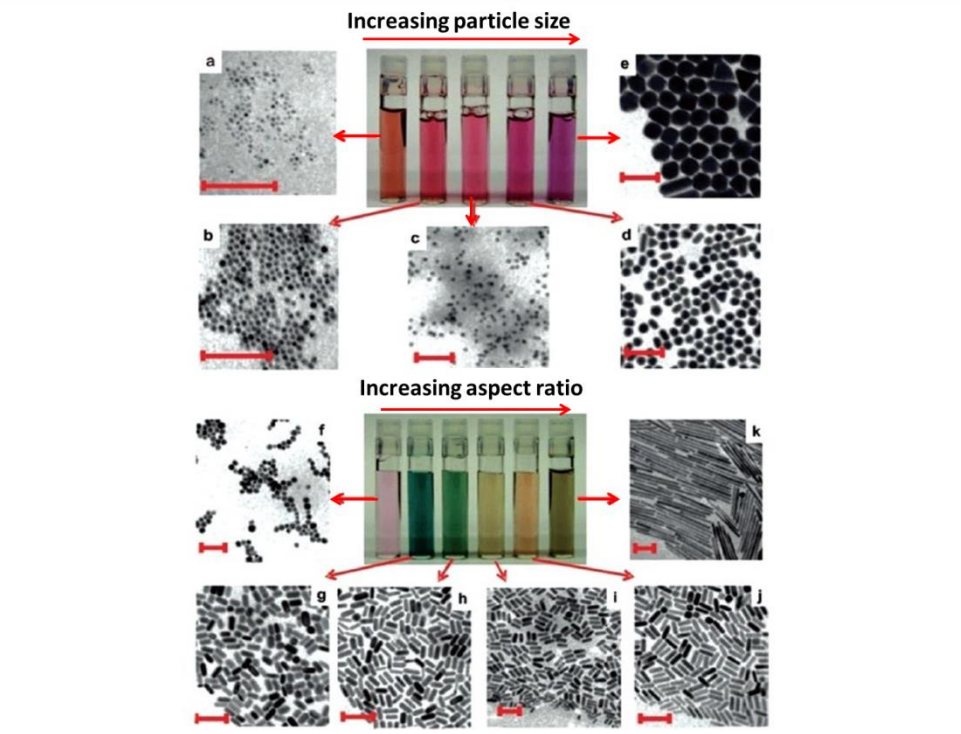


Figure 1.2 Photographs of gold nanospheres (upper panels) and gold nanorods (lower panels) in aqueous solutions as a function of increasing dimensions. The insets are their corresponding TEM images. The scale bar is 100 nm. [25]

For a single nanoparticle, the resonance spectral of the nanoparticle shifts with its size, shape and aspect ratio. On the other hand, coupling of two nanoparticles [27] can result in increased near-field intensity enhancement and confinement in the gap [28] (fig. 1.3 (a)), which extends a further degree of freedom in tuning the resonance frequency and a larger radiation efficiency. It has been shown that nanosphere and nanorod dimers can be physically small,

while they can provide high radiation efficiency due to the reduced current density inside the nanostructure. Another example of coupled nanoantennas is bow-tie dimer antennas, constituting of two triangles facing each other tip-to-tip [29] (fig. 1.3 (b)). In this case, higher field enhancement in the gap can be observed if compared with two-wire antennas, arising from the larger lightning-rod at the apex. Another report proposes the use of Yagi-Uda nanoantennas [30] for emission enhancement and broadband communication, providing the evidence that the inter-element distance is important to achieve the desired interference between direct and reflected radiation. This is because the neighboring elements may increase Ohmic losses and modify the resonance frequency of a nanoresonator via near-field coupling. Furthermore, symmetry breaking in the plasmonic clusters [31] supporting a Fano-like resonance is another way to modify the spectral shape, which is designed as a hemi-circular central disk surrounded by a circular ring of closely spaced, coupled nanodisks. These studies all confirm that near-field coupling can generate the large local field enhancement and modify the spectral shape. Good control of the interparticle distance, the geometry of nanoparticle dimer and the breaking of the symmetric geometry of nanostructures make it possible to flexibly tune the plasmon resonance in a wide range.

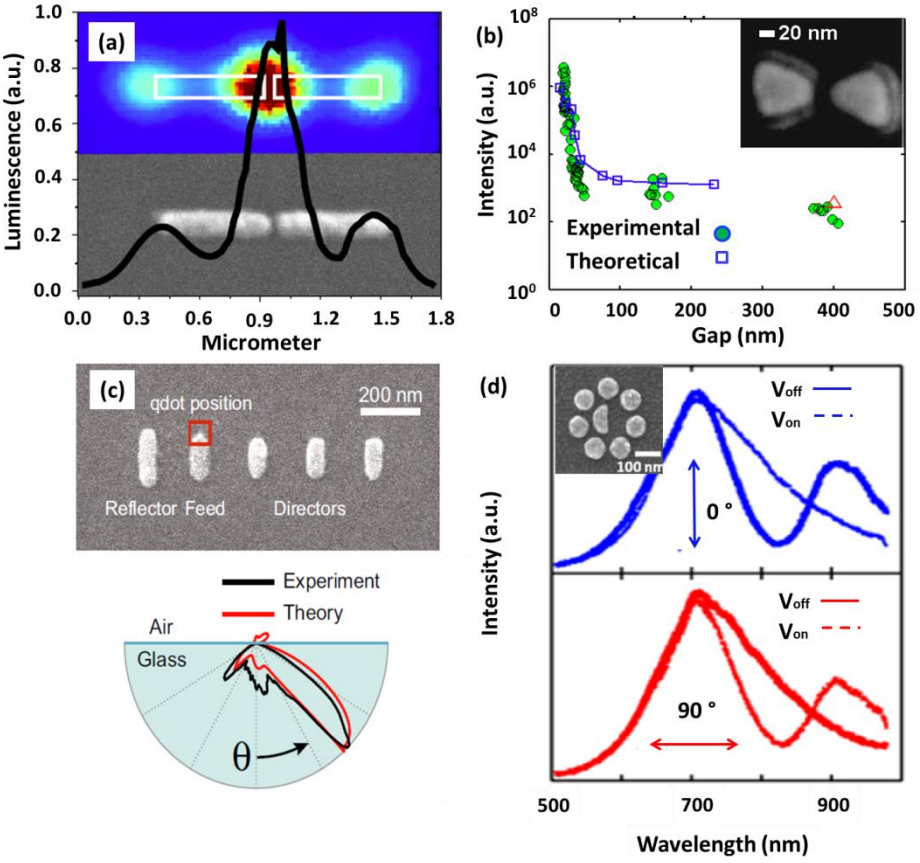


Figure 1.3 (a) Photon induced luminescence intensity distribution and SEM image of coupled gold nanoantennas with the dimension of 500×100×50 $nm^3$ and a gap of 40 nm [28]. (b) The intensity enhancement as a function of the gap ranging from 16 to 406 nm. SEM image of bow-tie with a gap of 22 nm is inserted in the top-left side [29]. (c) SEM image of the Yagi-Uda nanoantennas (upper panel) and angular radiation patterns for the antennas (bottom panel) [30]. (d) Scattering of an individual octamer with $V_{on}$ and $V_{off}$ detected for polarization direction of 0 °and 90 °.[31]

For a periodic array of nanoparticles, the far-field coupling [32, 33] is dominant when the interparticle spacing is greater than those of near-field coupling, e.g. in the sub-micrometer range (Figs. 1.4 (a) and (c)). Far-field coupling is able to generate a narrow line shape [34] in the spectra and provide strong field localization extending to the whole plane of nanostructures (Figs. 1.4 (b) and (d)). It has been reported that a waveguide consisting of a one-dimensional array of metallic nanoparticles can excite a dipole-dipole coupling, arising from the energy of excited dipole mode in a particle

transferred to neighboring particles (Fig 1.4 (a)). The collective plasmon resonances of the particle arrays can be measured by far-field polarization spectroscope. These studies provide a new opportunity to tune the optical properties of plasmon resonance and amplify the field intensity.

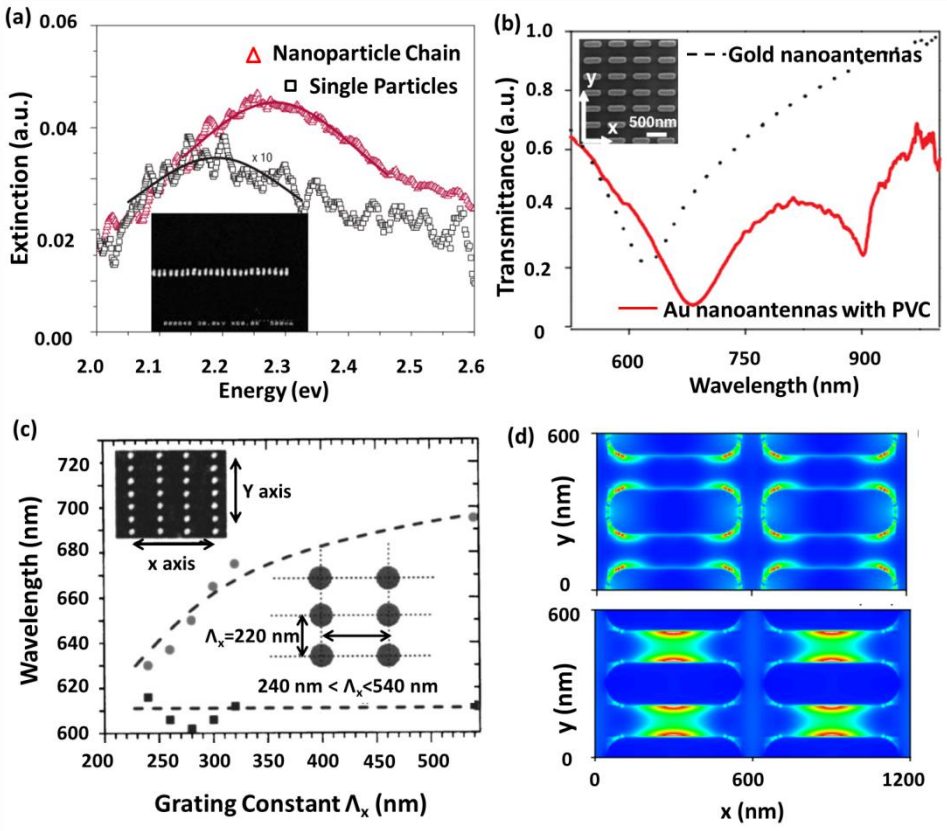


Figure 1.4 (a) Far-field extinction spectra of Ag nanoparticle chains and single particles [32]. The exciting light is polarized along the long axis of the nanorods, perpendicular to the particle chain axis. SEM image of the plasmon waveguide layout is inserted in the bottom-left side of the figure. (b) Particle plasmon wavelength as a function of the grating constant along *x* and *y* directions. SEM image of a grating with 220 and 540 nm in *x* and *y* directions is inserted in the top-left side of the figure. [34] (c) Measured transmission spectra of nanorod array on glass substrate (black dotted line) and covered by PVB layer (red solid line). [33] (d) Near-field intensity enhancements in 2D nanorod array are covered by PVB layer at wavelengths of 695 and 905 nm, respectively. [34]

### 1.1.2. Overview of nanofabrication techniques for plasmonic nanostructures

The development of nanofabrication techniques offers the ability to precisely control the geometry of nanostructures, providing the opportunity to tune the plasmon resonance in a wide range and also generate highly confined fields around nanoparticles. Attempts to engineer plasmonic nanostructures have been focused on both bottom-up and top-down nanofabrication techniques [35]. For example, chemical synthesis plays an active role to investigate plasmon properties of individual nanoparticles. By synthesizing different sizes, shapes, and materials of nanoparticles, properties of plasmon resonances of individual nanoparticles can be studied. When nanoparticles are self-assembled closely or almost touching each other, the coupling effects in pairs or among a cluster of nanoparticles have been studied. Large local field can be driven around metallic nanoparticles if compared to that induced only by individual nanoparticles. Alternatively, thermal annealing is a cost-effective method to form metallic nanoparticles with the diameter much smaller than light. Plasmon properties of these nanoparticles can be tuned by adjusting annealing temperature, thickness of metal films and applying the template before annealing.

It has been reported that a pairs of nanoparticles or periodic array of nanoparticles could excite highly intense local fields because of near-field and far-field coupling [28]. Scanning beam lithography, soft lithography and laser interference lithography are advanced top-down nanofabrication tools, which could precisely control size, shape and interparticle distance of nanoparticles.

In this section, state-of-art nanofabrication tools to form plasmonic nanostructures are reviewed as bellow.

#### 1.1.2.1 Chemical synthesis

Chemical synthesis is one of most common bottom-up nanofabrication techniques capable of patterning a wide variety of metal nanoparticle shapes (e.g. stars, rods, boxes and cages) by independently controlling reaction conditions such as temperature, surfactants, and precursors [36] (Fig. 1.5). Tailoring and fine-tuning optical resonance properties can be achieved through the precise control over the geometric structure parameters of metallic nanoparticles. Metal particles can also be assembled into two-dimensional or three-dimensional lattices on substrates, allowing the optical properties of the assemblies to be tuned by manipulating the interparticle distance and the geometry of the lattices.

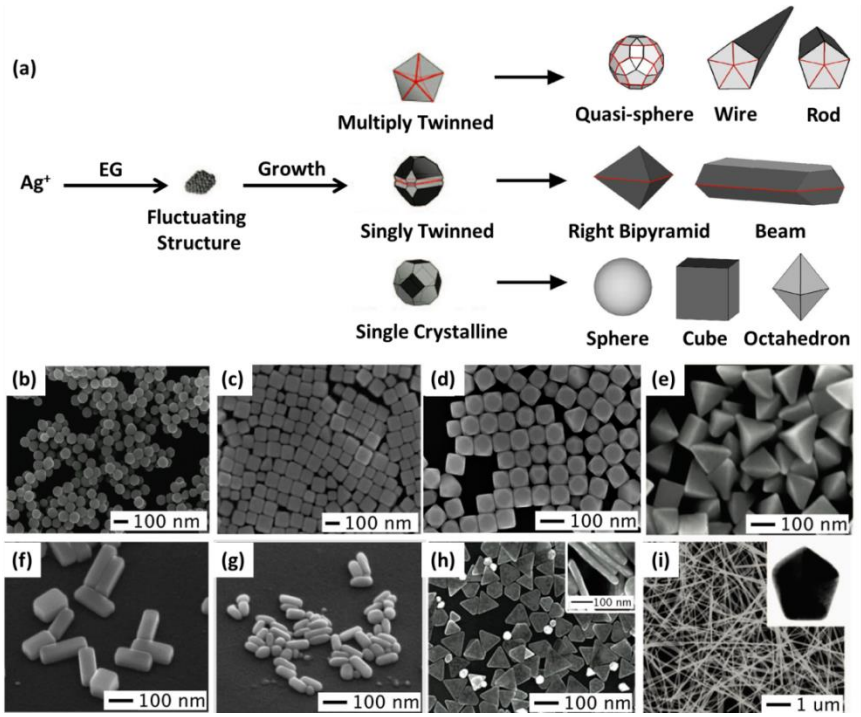


Figure 1.5 (a) Schematic diagram of the reduction of $Ag^{+}$ ions by ethylene glycol (EG). SEM images of different Ag nanoparticles grown by the reduction process: (b) spheres, (c) cubes, (d) truncated cubes, (e) right bipryamids, (f) bars, (g) spherodics, (h) triangular plates, and (i) wires. [36]

### 1.1.2.2. Thermal annealing

Recently, dewetting of ultrathin (<100 nm) polymer films [37] and their self-organization on physic-chemically patterned substrates has been extensively studied. It has been shown that thermal annealing is a simple method to prepare nanoparticles at the nanoscale level through the dewetting of thin films at elevated annealing temperatures. This approach can be applied to fabricate metallic nanoparticles on top of substrates, providing the opportunity to reduce the size down to sub-50 nm over a large area (Figs. 1.6 (a)-(b)) [38]. However, the main drawback of this approach is low uniformity, as the assembly consists of random size distribution and disorder arrangement

of patterned nanoparticles. The template-assisted wetting method [39] can reduce the degree of randomness and disorder (Figs. 1.6 (b)-(d)).

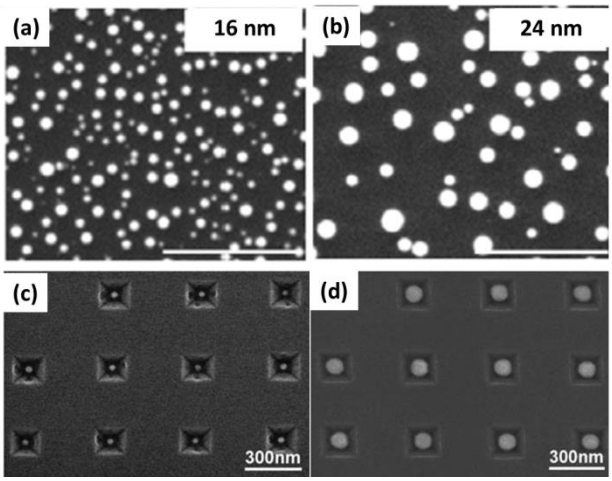


Figure 1.6 SEM images of gold nanoparticles obtained through the dewetting of continuous films at the thicknesses of (a) 16 and (b) 24 nm, respectively [38]. SEM images of gold nanoparticles obtained through the dewetting of Au films inside the inverted pyramids at the thickness of (c) 5 and (d) 20 nm, respectively [39].

### 1.1.2.3. Scanning beam lithography

Although chemical synthesis provides unique biomolecular control, biomimetic behavior, and the potential to create the materials with sophisticated properties, this work is limited to the inherent macroscopic disorder [35]. This disorder could lead to the generation of the complex metallic nanostructures, which brings about much difficulty in understanding and modeling the fundamentals of surface plasmon. Top-down nanopatterning is an alternative nanofabrication technique, which enables the disordered arrangement from the chemical synthesis to be avoided. It offers the capabilities of versatility, miniaturization, precision, reproducibility and batch fabrication, which have been applied to the semiconductor industry over a few decades.

Scanning beam lithography [40] as conventional top-down nanofabrication techniques, such as electron beam lithography (EBL) [41] and focused ion beam (FIB) [42], is able to achieve high density patterning of good uniform structural features with sub-10 nm gaps or sophisticated geometry (Fig. 1. 7). However, the main challenging issues for these nanofabrication tools are high operating cost, low throughput and the difficulty in accessing the facilities. Although multi-axis electron beam lithography and zone-plate-array lithography are developed to improve the throughput [43], they suffer from lens aberration and diffraction limit, respectively. Moreover, highly sensitive characterization facilities, such as dark-field microscope or spectroscope are required, as these nanostructures patterned by EBL and FIB possess the fabrication area with the size dimension of only a few hundred micrometers as a result of weak signals.

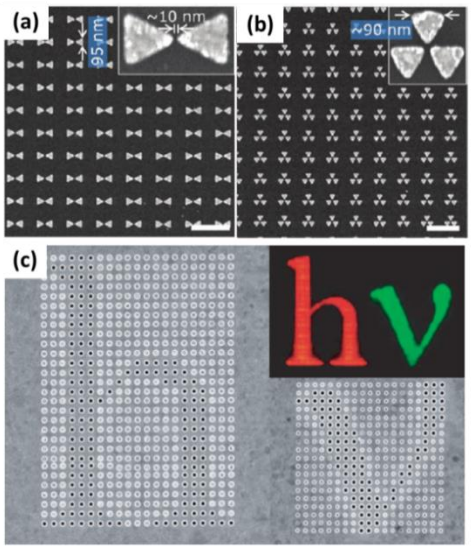


Figure 1.7 (a) Au bow-tie nanostructures with an edge length of ~95 nm and (b) Au trimer structures with an average triangle edge length of ~90 nm prepared by EBL [41]. (c) An array of nanoholes is prepared by focused-ion-beam milling of an Ag film [42].

#### 1.1.2.4. Soft lithography

Soft lithography [44] is a suite of techniques that uses organic materials to enable replication and pattern transfer on multiple length scales (from nanometers to centimeters). The strengths of these tools are high efficiency and low cost, allowing the production of numerous modes from the same master. However, the master is usually very expensive due to the conventional nanofabrication tool (e.g. EBL) employed. In addition, the replication of patterns on substrates experiences many steps, which makes it difficult to replicate nanoscale features with high aspect ratios.

#### 1.1.2.5. Laser interference lithography

Laser interference lithography (LIL) [45] is a promising top-down nanofabrication technique that serves as a large-area, maskless and noncontact nanopatterning technique. This technique can be used to pattern periodic nanolines and nanodisks on metallic thin films in a short time (only a few minutes exposure). In particular, LIL allows us to pattern nanostructures with the dimension of sub-micrometers. In the exposure process, the photoresist is usually exposed to the interference pattern of two coherent laser beams. Size dimension of nanostructures can be further decreased if the incident angle of the laser beam is increased. LIL exhibits better performance than EBL and FIB on low-cost, high-efficiency and large effective fabrication area, but it cannot pattern complex nanostructures.

## 1.2. Research objective

### 1.2.1. Research focus

In this thesis, effort will be focused on the design and fabrication of plasmonic nanostructures over a large area using scalable, rapid and inexpensive nanofabrication tools, such as laser nanofabrication and thermal annealing, with the aim of implementing the potential applications both in terms of refractive index sensing and surface enhanced Raman spectroscopy. However, a few key challenges in the development of the practical plasmonic sensing need to be described as listed below:

- Plasmonic nanostructures formed through some nanofabrication techniques suffer from small areas and high fabrication cost, for example EBL or FIB. These drawbacks could hinder the pace of transfer of technology from laboratory to the real fabrication in industry. Therefore, it is strongly required to employ a simple design and high-throughput nanofabrication tool for the realization of large area plasmonic nanostructures.
- The designed nanostructures need to provide the high intensity field, enabling to detect the refractive index change of the surroundings and enhance the Raman intensity of molecules.
- LSPR-based sensors are limited to a low sensitivity, arising from the excitation of the dipolar resonance as a result of large radiative damping from the individual nanostructure, which makes it difficult to detect the subtle variation of the refractive index change from small molecules. Hence,

plasmonic nanostructures with high performance sensitivity and narrow linewidth are highly desired.

- Tuning LSPR plays a critical role in enhancing the Raman intensity of the molecules, owing to the fact that the resonance wavelength needs to well match the excitation wavelength and also overlap with an electronic absorption band of interest. However, there is still a lack of knowledge on flexibly tuning LSPR wavelength of nanostructures by a simple and efficient approach.

### 1.2.2. Research contributions

The main contributions of this thesis can be summarized as following:

- A novel hybrid nanofabrication technique has been investigated. By the combination of LIL and thermal annealing, metallic nanodot array with a size dimension of sub-50 nm is fabricated for the first time. The significance of the nanofabrication method is that it provides the feasibility to realize plasmonic nanostructures over a large area with good uniformity and tunable plasmon resonance in UV-visible range.

- The refractive index sensitivity of the nanodot array has been improved when compared to that of nanodots formed only by thermal annealing. The enhancement in the response to the refractive index of the surroundings is attributed to the excitation of LSPR induced by nanodot array with a good uniformity both in terms of size dimension and particle distribution. This result provides the clear evidence that the fabricated nanodot array can be applied to serve as the refractive index sensors, and also confirms the point

that more intense near-field energy can be generated by nanostructures with more uniform geometries.

- Tuning LSPR has been achieved by arranging the concentration of the material, which is confirmed both by bimetallic nanodots and nanodot array. In particular, the resonance wavelengths of LSPR for these nanostructures are able to shift towards a longer wavelength with an increase of Au concentration. This finding provides a simple and easily-producible approach to tune the optical properties of LSPR in a wide range.

- The Raman intensity of the molecules R6G has been enhanced by bimetallic Ag/Au nanodot array. The tunable plasmon resonances can be applied to further enhance the Raman intensity, arising from a good matching condition occurring between the plasmon resonance wavelength of the nanostructures and the excitation wavelength. LSPR of nanodot array also overlaps a particular absorption band of the molecules R6G as a result of the enhancements in the molecule absorption and emission. This result indicates that the Raman scattering of the molecules can be dramatically amplified if the plasmon resonance can be engineered and optimized.

- The refractive index sensitivity has been improved by a periodic array of nanorods due to the excitation of surface lattice resonances, which provides the ability to shape a narrow linewidth and strong near-field spatial distributions. One of most significant advantages is the design of straightforward structural parameters, which can be patterned by the laser over a large area.

- Tuning the surface lattice resonance has been achieved by varying the lattice constant of gold nanorod array. In particular, the spectral wavelengths

and shapes of surface lattice resonances (SLR) and LSPR can be flexibly tuned due to the strong modification on the excitation condition of SLR. Such optimized nanostructures can provide an even higher refractive index sensing sensitivity for SLR mode due to much stronger near-field enhancements extending in the whole plane of nanorods.

### 1.3. Organization of thesis

The organization of this thesis addresses the objectives of this research.

**Chapter 2** covers the theoretical background of the fundamentals of surface plasmon, the prime applications of plasmonic sensing based on LSPR and nanofabrication techniques employed in this study.

**Chapter 3** presents the detailed experimental procedure employed in this study, consisting of the experimental setup, characterization method as well as the simulation tool.

**Chapter 4** reports a scalable, rapid and inexpensive method based on the combination of LIL and thermal annealing for the fabrication of disordered and quasi-ordered metallic nanodots on glass substrates with tunable LSPR. These nanostructures give the ability to detect the variation of the refractive index change from the surrounding media and to enhance the Raman intensity of molecules.

**Chapter 5** shows that the excitation of the surface lattice resonance in an array of nanorods can induce a strong modification in the transmission characteristics, leading to a narrow line shape and strong near-field spatial distributions extending in the plane of the array. This resonance has to be excited under the specific light polarization, which gives the ability to have

large refractive index sensitivity and high figure of merit confirmed both by simulation and experimental results.

**Chapter 6** studies the influence of varying the lattice constant of Au nanorod array on SLR. The optical properties and near-field intensity distributions at plasmon resonances for nanorod array with different lattice constants are investigated. It is found that tuning the lattice constant of nanorod array can modify the resonance wavelength and linewidth of SLR and LSPR.

**Chapter 7** gives an overall conclusion of the research project. The results of the design, fabrication and characterization of large area plasmonic nanostructures are summarized. The prospective developments of these nanostructures on the potential applications are also explored.

### 1.4. References


[1] S. A. Maier, M. L. Brongersma, P. G. Kik, A. A. G. Requicha, and H. A. Atwater, "Plasmonics – A route to nanoscale optical devices", Adv. Mater. **13**, 1501 (2001).

[2] H. Atwater, "The promise of plasmonics", Sci. Am. **296**, 56-63 (2007).

[3] E. Ozbay, "Plasmonics: merging photonics and electronics at nanoscale dimensions", Science **311**, 189-193 (2006).

[4] M. Moskovits, "Surface-enhanced spectroscopy," Rev. Mod. Phys. **57**, 783–826 (1985).

[5] A. Merlen, F. Lagugne-Labarthet and E. Harte, "Surface-enhanced Raman and fluorescence spectroscopy and dye molecules deposited on nanostructured gold surfaces," J. Phys. Chem. C **114**, 12878-12884 (2010).

[6] N. Liu, M. L. Mang, M. Hentschel, H. Giessen, A. P. Alivisatos, "Nanoantenna-enhanced gas sensing in a single tailored nanofocus," Nat. Mater. **10**, 631-636 (2011).

[7] Y. Z. Piao, A. Burns, J. Kim, U. Wiesner, and T. Hyeon, "Designed fabrication of silica-based nanostructured particle systems for nanomedicine applications", Adv. Funct. Mater. **18**, 3745-3758 (2008).

[8] British Museum. Lycurgus cup. http://www.britishmuseum.org, 2008.

[9] R. W. Wood, "On a remarkable case of uneven distribution of light in a diffraction grating spectrum," Philos. Mag. **4**, 396-402 (1902).

[10] J. C. Maxwell Garnett, "Colours in metal glasses and in metallic films," Phil. Trans. R. Soc. Lond. A. **203**, 359-371 (1904).

[11] G. Mie, "Beitrage zer Optik truber Meiden speziell kolloidaler Metallosungen," Ann. Phys. **25**, 377-445 (1908).

[12] D. Pines, "Collective energy losses in solids," Rev. Mod. Phys. **28**, 184-198 (1956).

[13] R. H. Ritchie, "Plasma losses by fast electrons in thin films," Phys. Rev. **106**, 874-881 (1957).

[14] J. J. Hopfield, "Theory of the contribution of excitations to the complex dielectric constant of crystals," Phys. Rev. **112**, 1555 (1958).

[15] R. H. Ritchie, E. T. Arakawa, J. J. Cowan, R. N. Hamm, "Surface-plasmon resonance effect in grating diffraction," Phys. Rev. Lett. **21**, 1530-1533 (1968).

[16] A. Otto, "Excitation of nonradiative surface plasma waves in silver by the method of frustrated total reflection," Z. Phys. **216**, 398-410 (1968).

[17] E. Kretschmann and H. Raether, “Radiative decay of nonradiative surface plasmon excited by light,” Z. Naturf. A **23**, 2135-2136 (1968).

[18] T. Endo, S. Yamamura, N. Nagatani, Y. Morita, Y. Takamura and E. Tamiya, “Localized surface plasmon resonance based optical biosensor using surface modified nanoparticle layer for label-free monitoring of antigen-antibody reaction,” Sci. Technol. Adv. Mater. **6**, 491 (2005).

[19] J. Henzie, J. Lee, M. H. Lee, W. Hasan, and T. W. Odom, “Nanofabrication of plasmonic structures,” Annu. Rev. Phys. Chem. **60**, 147-165 (2009).

[20] L. B. Sagle, L. K. Ruvuna, J. A. Ruemmele, R. P. Van Duyne, “Advances in localized surface plasmon resonance spectroscopy biosensing,” Nanomedicine **6**, 1447-1462 (2011).

[21] K. L. Kelly, E. Coronado, L. L. Zhao, and G. C. Schatz, “The optical properties of metal nanoparticles: the influence of size, shape, and dielectric environment”, J. Phys. Chem. B **107**, 668-677 (2003).

[22] J. N. Anker, W. P. Hall, O. Lyandres, N. C. Shah, J. Zhao, and R. P. Van Duyne, “Biosensing with plasmonic nanosensors,” Nat. Mater. **7**, 442-453 (2008).

[23] N. Guillot, H. Shen, B. Fremaux, O. Peron, E. Rinnert, T. Toury, and M. Lamy de la Chapelle, “Surface enhanced Raman scattering optimization of gold nanocylinder arrays: influence of the localized surface plasmon resonance and excitation wavelength,” Appl. Phys. Lett. **97**, 023113 (2010).

[24] K. C. Ng and W. Cheng, “Fine-tuning longitudinal plasmon resonances of nanorods by thermal reshaping in aqueous media,” Nanotechnology **23**, 105602 (2012).

[25] L. M. Liz-Marzan, M. Giersig, and P. Mulvaney, “Synthesis of nanosized gold-silica core-shell particles,” Langumir **12**, 4329-4335 (1996).

[26] A. Dmitriev, T. Pakizeh, M. Kall, and D. S. Sutherland, “Gold-silica-gold nanosandwiches: tunable bimodal plasmonic resonators,” Small **3**, 294-299 (2007).

[27] A. M. Funston, C. Novo, T. J. Davis, and P. Mulvaney, “Plasmon coupling of gold nanorods at short distances and in different geometries,” Nano Lett. **9**, 1651-1658 (2009).

[28] P. Ghenuche, S. Cherukulappurath, T. H. Taminiau, N. F. van Hulst, and R. Quidant, “Spectroscopic mode mapping of resonant plasmon nanoantennas,” Phys. Rev. Lett. **101**, 116805 (2008).

[29] P. J. Schuck, D. P. Fromm, A. Sundaramurthy, G. S. Kino, and W. E. Moerner, “Improving the mismatch between light and nanoscale objects with gold bowtie nanoantennas,” Phys. Rev. Lett. **94**, 017402 (2005).

[30] J. Dorfmuller, D. Dregely, M. Esslinger, W. Khunsin, R. Vogelgesang, K. Kern, and H. Giessen, “Near-field dynamics of optical Yagi-uda nanoantennas,” Nano Lett. **11**, 2819-2824 (2011).

[31] W. S. Chang, J. B. Lassiter, P. Swanglap, H. Sobhani, S. Khatua, P. Nordlander, N. J. Halas, and S. Link “A plasmonic fano switch,” Nano Lett. **12**, 4977-4982 (2012).

[32] S. A. Maier, P. G. Kik, H. A. Atwater, S. Meltzer, E. Harel, B. E. Koel, and A. A. G. Requicha, “Local detection of electromagnetic energy transport below the diffraction limit in metal nanoparticle plasmon waveguides,” Nat. Mater. **2**, 229-232 (2003).

[33] B. Auguie, and W. L. Barnes, “Collective resonances in gold nanoparticle Arrays,” Phys. Rev. Lett. **101**, 143902 (2008).

[34] G. Vecchi, V. Giannini, and J. G. Rivas, “Shaping the fluorescent emission by lattice resonances in plasmonic crystals of nanoantennas,” Phys. Rev. Lett. **102**, 146807 (2009).

[35] D. Mijatovic, J. C. T. Eijkel, and A. V. den Berg, “Technologies for nanofluidic systems: top-down vs. bottom-up – a review,” Lab Chip **5**, 492-500 (2005).

[36] G. A. Ozin, K. Hou, B. V. Lotsch, L. Cademartiri, D. P. Puzzon, F. Scotognella, A. Ghadimi, J. Thomson, “Nanofabrication by self-assembly,” Mater. Today **12**, 12-23 (2009).

[37] L. J. Xue, Y. C. Han, “Inhibition of dewetting of thin polymer films,” Prog. Mater. Sci. **57**, 947-979 (2012).

[38] P. Farzinpour, A. Sundar, K. D. Gilroy, Z. E. Eskin, R. A. Hughes, and S. Neretina, “Altering the dewetting characteristics of ultrathin gold and silver films using a sacrificial antimony layer,” Nanotechnology **23**, 495604 (2012).

[39] W. K. Choi, T. H. Liew, H. G. Chew, F. Zheng, C. V. Thompson, Y. Wang, M. H. Hong, X. D. Wang, L. Li, and J. Yun, “A combined top-down and bottom-up approach for precise placement of metal nanoparticles on silicon,” Small **4**, 330-333 (2008).

[40] M. Geissler and Y. N. Xia, “Patterning: principles and some new developments,” Adv. Mater. **16**, 1249-1269 (2004).

[41] H. Duan, H. Hu, K. K. Kumar, Z. Shen, and J. K. W. Yang, “Direct and reliable patterning of plasmonic nanostructures with sub-10-nm gaps,” ACS Nano **5**, 7593-7600 (2011).

[42] C. Genet, T. Ebbesen, “Light in tiny holes,” Nature **445**, 39-46 (2007).

[43] R. F. Pease, L. Han, G. I. Winograd, W. D. Meisburger, D. Pickard and M. A. McCord, “Prospects for charged particle lithography as a manufacturing technology,” Microelectron. Eng. **53**, 55-60 (2000).

[44] B. D. Gates, Q. B. Xu, J. C. Love, D. B. Wolfe and G. M. Whitesides, “Unconventional nanofabrication,” Annu. Rev. Mater. Res. **34**, 339-372 (2004).

[45] I. Byun and J. Kim, “Cost-effective laser interference lithography using 405 nm AlInGaN semiconductor laser,” J. Micromech. Microeng. **20**, 055024 (2010).

# Chapter 2 Theoretical Background

This chapter reviews the fundamentals of localized surface plasmon resonances (LSPR) and the nanofabrication technique employed in this study. Firstly, the basic concepts of surface plasmon polaritons and localized surface plasmon resonances induced by a single nanoparticle as well as an array of nanoparticle will be described. Secondly, the working principle of LSPR-based nanosensors will be discussed, with special attention on refractive index sensing and surface enhanced Raman spectroscopy (SERS). Thirdly, we will explain how laser interference lithography can be applied to generate large area plasmonic nanostructures and the related factors that affect the patterns.

## 2.1. Physics of localized surface plasmon resonances

Localized surface plasmons have been drawing great attention of research recently due to the interaction between the light and nanoparticles of the dimension much smaller than the incident wavelength. This leads to plasmon that oscillates locally around nanoparticles with a frequency known as the localized surface plasmon resonance (LSPR). The LSPR is sensitive to changes in the local environment, which can be used for refractive index sensing through a LSPR wavelength-shift measurement. The LSPR wavelength is also determined by the geometric parameters of metallic nanoparticles, involving the sizes, shapes, materials and local dielectric properties.

### 2.1.1. Theoretical background of surface plasmon polaritons

#### 2.1.1.1. Equations of surface plasmon polaritons

A plasmon can be described as an oscillation of free electron density with respect to the fixed positive ions in a metal [1]. To explain the physics behind free electron oscillations, the Drude model, as one of the simplest models, can be used to describe the response of a metallic particle exposed to an external electric field. This model is proposed by Paul Drude [2] at the beginning of the 20$^{th}$ century. The Drude model assumes that the electron dynamics in metal can be described in a microscopic view and treated classically. These plasmon oscillations therefore can be explained by mechanical oscillations of the electron gas in a metal. The presence of an external electric field can cause displacements of the electron gas with respect to the fixed ionic cores. The Drude-Sommerfeld model of a free electron gas is given by [3]

$$m_e \frac{\partial^2 \boldsymbol{r}}{\partial t^2} + m_e \gamma_d \frac{\partial \boldsymbol{r}}{\partial t} = e E_0 e^{-i\omega t} \,, \qquad \text{(Eq. 2.1)}$$

where $\gamma_d$ describes a damping term, $m_e$ the effective free electron mass, $e$ the free electron charge, $\omega$ the frequency, $E_0$ amplitude of the applied electric field and $\boldsymbol{r}$ position of the negative charge center, respectively. The dielectric function of the Drude mode is derived by solving Eq. 2.1:

$$\varepsilon_d(\omega) = \varepsilon_\infty - \frac{\omega_p^2}{\omega^2 + i\gamma_d \omega}, \text{ with } \omega_p = \sqrt{\frac{4\pi n_e e^2}{m_e}} \,. \qquad \text{(Eq. 2.2)}$$

Here $\omega_p$ is the volume or bulk plasmon frequency (electron density $n_e = 3/4\pi {r_s}^3$), $r_s$ is the electron gas parameter, $\varepsilon_\infty$ is the permittivity of ionic background in the metal, and $\gamma_d$ is the collision frequency. For larger frequencies close to $\omega_p$ , $\gamma_d$ and $\varepsilon_\infty$ can be ignored due to negligible damping. The Drude dielectric function of the undamped free electron plasma can be simplified as $\varepsilon_d = 1 - \omega_p^2/\omega^2$ . There are two distinguishable frequency regions: if $\omega > \omega_p$ , $\varepsilon_d$ is positive and the corresponding refractive index $n = \sqrt{\varepsilon_d}$ is a real quantity [4]. On the other hand, if $\omega < \omega_p$ , $\varepsilon_d$ becomes negative and $n$ is imaginary, which implies an electromagnetic wave cannot propagate inside the medium.

#### 2.1.1.2. Dispersion curve of surface plasmon polaritons

In order to understand the properties of surface plasmon polaritons (SPPs), the derivation of the dispersion relation is required. The simplest geometry sustaining SPPs is that of a flat interface between a dielectric, non-absorbing half space (z > 0) with positive real dielectric constant $\varepsilon_2$ and an adjacent conducting half space (z < 0) described through a dielectric function $\varepsilon_1(\omega)$ (Fig. 2.1 (a)). A complex parallel wavenumber is $k_x = k_x' + ik_x''$, in which the real part $k_x'$ determines the SPP wavelength and the imaginary part $k_x''$ represents the damping of the SPP, as it propagates along the interface. The real and imaginary parts of $k_x$ can be obtained from the equation [5,6]:

$$k_{sp} = k_0 \sqrt{\frac{\varepsilon_d \varepsilon_m}{\varepsilon_d + \varepsilon_m}}, \qquad \text{(Eq. 2.3)}$$

where $k_0 = \omega/c$ , $\varepsilon_m$ and $\varepsilon_d$ are the metal and dielectric permittivities, respectively. The important feature of surface plasmons [7] is that for the same frequency, the momentum ($\hbar k_{spp}$) of the SPP wave is always larger than that of the light in free space photon ($\hbar k$) (Fig 2.1 (b)). In other words, there is a momentum mismatch between light (yellow solid line) and SPP (red solid line). The surface plasmon polaritons can be excited only when one can provide the missing momentum through tilting the light line to a certain angle in a dielectric medium (yellow dashed line).

The skin depth and propagation length are the basic properties of surface plasmons. They are determined by the imaginary part of the dielectric function that is related to energy dissipation of the material. The skin depth $\delta$ is defined as the distance, where the exponentially decreasing evanescent field $e^{-|k_z||z|}$ falls to 1/e of its value at the surface [6].

$$\delta = \frac{1}{|k_{zi}|} \text{ or } \begin{cases} \delta_d = \frac{\lambda}{2\pi}\sqrt{\frac{\varepsilon_m+\varepsilon_d}{\varepsilon_d^2}} & in\ medium\ with\ \varepsilon_d \\ \delta_m = \frac{\lambda}{2\pi}\sqrt{\frac{\varepsilon_m+\varepsilon_d}{\varepsilon_m^2}} & in\ metal\ with\ \varepsilon_m \end{cases}. \qquad \text{(Eq. 2.4)}$$

Since the dielectric constant $\varepsilon_d$ is usually much smaller than the real part of $\varepsilon_m$, Eq. 2.4 can be replaced with the approximation $\delta_m \approx \lambda/(2\pi\varepsilon_m')$, where $\varepsilon_m = \varepsilon_m' + i\varepsilon_m''$. If a surface plasmon propagates along a smooth surface, the intensity decrease with $x$ as $e^{-2k_x''x}$ where $k_x = k_x' + ik_x''$. The length $\delta = 1/(2k_x'')$ is defined as the propagation length that the intensity has fallen to 1/e.

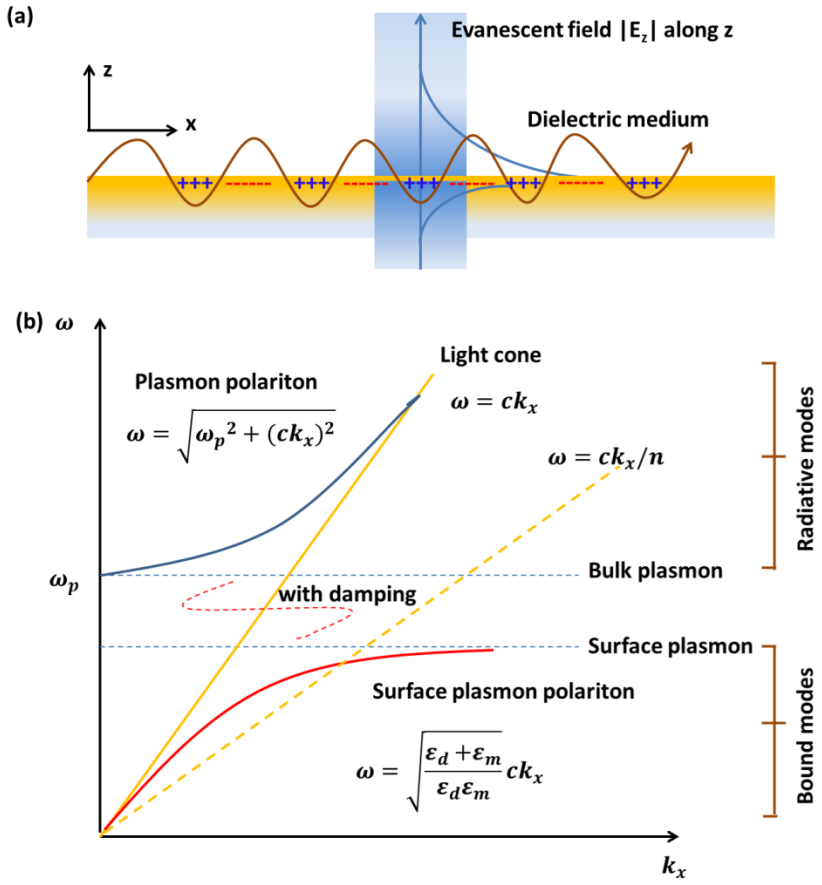


Figure 2.1 (a) Surface plasmon polaritons at a dielectric-metal interface. (b) Plasmon dispersion curves at a metal/air interface. The dispersion curves of plasmons (red solid line for surface plasmon and blue solid line for free electrons) do not cross the light cone (yellow solid line) at any point. [7]

### 2.1.1.3. Excitation of surface plasmons

The excitation of a surface plasmon polariton by light is only possible if the wavevector of the exciting light can be increased over its free-space value. The momentum of light and SPP can be matched using different coupler configurations such as prism couplers, grating couplers, fibre and waveguide couplers.

Prism couplers are the most frequently used methods to excite surface plasmons. Using the attenuated total reflection (ATR) method, the Kretschmann configuration can achieve the excitation (Fig 2.2 (a)). A light

wave passes through a high refractive index prism and is totally reflected at the base of the prism, resulting in an evanescent wave penetrating into a thin metal film. By controlling the angle of the incidence, the light wavevector in the prism can match with the SPP wavevector on an air-metal surface.

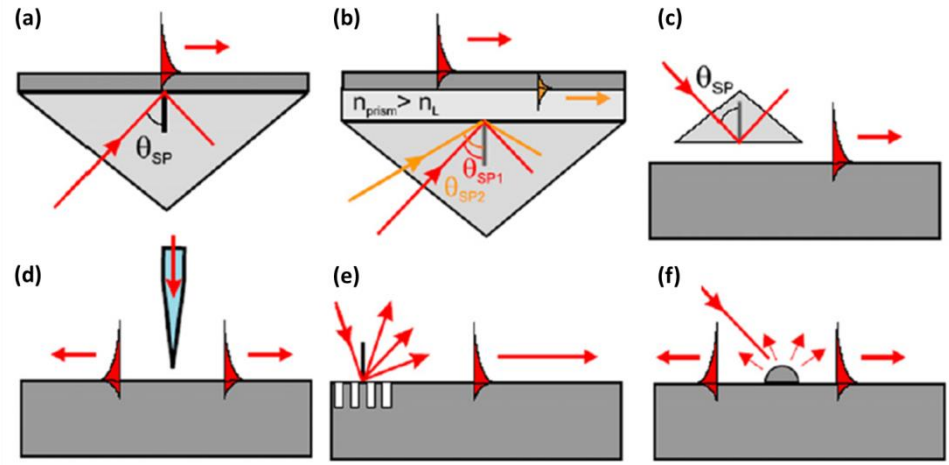


Figure 2.2 SPP excitation configurations: (a) Kretschmann geometry, (b) two-layer Kretschmann geometry, (c) Otto geometry, (d) excitation with an SNOM probe, (e) diffraction on a grating and (f) diffraction on surface features. [7]

A two-layer geometry Kretschmann configuration is applied when the tunneling distance is increased (Fig 2.2 (b)). This is because the increased distance can affect the efficiency of the SPP excitation. This configuration includes a dielectric layer which is deposited between the prism and the metal film. The refractive index of the dielectric is smaller than that of the prism. Thus, the light tunneling through this dielectric layer excites SPPs on an internal metal interface at different incident angles.

If the metal film is too thick, the Kretschmann configuration cannot be used to excite SPPs. An Otto configuration can overcome the problem by

placing the prism close to the metal surface (Fig. 2.2 (c)). In this case, the light tunneling occurs through the air gap between the prism and the surface.

It is also possible to excite SPPs locally at a given place on a surface by using scanning near-field optical microscope (SNOM) (Fig. 2.2 (d)). A near-field coupling occurs between the light and the sub-wavelength aperture of the fiber tip.

Diffraction is another example to provide the wavevector conservation for the SPP excitation (Figs. 2.2 (e) and (f)). The diffracted orders of the periodically corrugated metal-dielectric interface can exhibit larger wavevectors in the magnitude than those of the incident light, leading to the light coupled to the SPP through the metal grating. A rough surface can also allow the SPPs to be excited on both the air-metal and glass-metal interfaces (Fig. 2.2 (f)).

### 2.1.2. Theoretical background of localized surface plasmon resonances: single nanoparticles and a periodic array of nanoparticles

Surface plasmons can be localized in geometries [8], such as metallic particles [9], or voids of various topologies [10]. Such surface excitations in bounded geometries are called localized surface plasmons (LSPs). These resonances induced by the noble metal nanostructures, can create sharp spectral absorption and scattering as well as strong electromagnetic near-field enhancements.

#### 2.1.2.1. Single metallic nanoparticles

For a spherical metallic nanoparticle of radius $a$ embedded in a non-absorbing surrounding medium of dielectric constant $\varepsilon_{media}$, the interaction between light and nanoparticle can be analyzed using the simple quasi-static approximation, giving the particle polarizability $\alpha$ [11]:

$$\alpha = 4\pi a^3 \frac{\varepsilon - \varepsilon_{media}}{\varepsilon + 2\varepsilon_{media}}, \quad \text{(Eq. 2.5)}$$

where the complex $\varepsilon = \varepsilon(\omega)$ describes the dispersive dielectric response of the metal. This equation indicates that the polarizability experiences a resonant enhancement under the condition that $|\varepsilon + 2\varepsilon_{media}|$ is a minimum. The resonance is simplified as:

$$Re[\varepsilon(\omega)] = -2\varepsilon_{media}\,. \quad \text{(Eq. 2.6)}$$

This relationship is called the Fröhlich condition. For a sphere located in air consisting of a Drude metal with a dielectric function:

$$\varepsilon(\omega) = 1 - \frac{\omega_p^2}{\omega^2}, \quad \text{(Eq. 2.7)}$$

the Fröhlich condition is satisfied at the frequency $\omega_0 = \omega_p/\sqrt{3}$. It implies the strong dependence of the resonance frequency on the dielectric environment.

Mie theory can be applied to explain the extinction coefficient $E(\lambda)$ in the long-wavelength limit [12]:

$$E(\lambda) = \frac{24\pi N_A a^3 \varepsilon_{media}^{3/2}}{\lambda In(10)} \times [\frac{\varepsilon_i}{(\varepsilon_r + 2\varepsilon_{media})^2 + \varepsilon_i^2}] \,, \qquad \text{(Eq. 2.8)}$$

where $N_A$ describes the real density of the nanoparticles, $a$ the radius of the metallic nanosphere, $\varepsilon_{media}$ the dielectric constant of the medium surrounding the nanosphere (assumed to be a positive, real number), λ the wavelength, and $\varepsilon_r$ and $\varepsilon_i$ the real and imaginary parts of the metal dielectric function, respectively. This equation indicates that a resonant peak is generated under the condition that $\varepsilon_r = -2\varepsilon_{media}$. When one considers spheroidal-shape particles, the term $\varepsilon_r + 2\varepsilon_{media}$ is replaced by $\varepsilon_r + \chi\varepsilon_{media}$, where χ is a parameter that depends on the shape of the spheroid, increasing from 2 for a sphere to 17 for a spheroid with an aspect ratio of 5:1 [13-15].

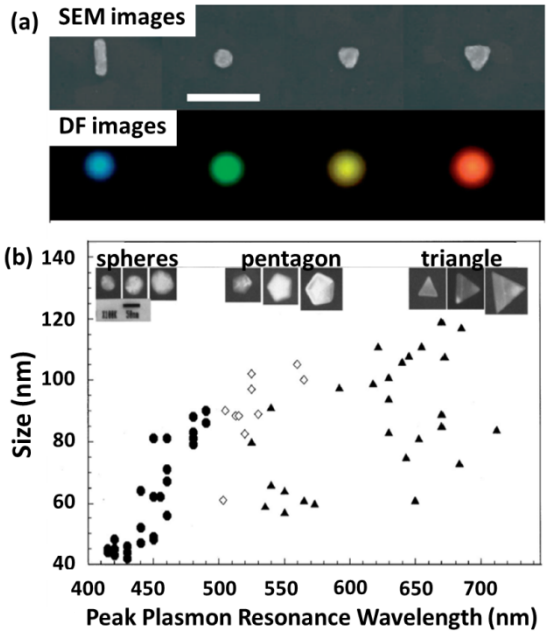


Figure 2.3 (a) SEM and dark-field images of several metallic nanoparticles made by e-beam lithography. From left to right, the shapes are a rod, a disc, and two triangles. The thickness of these particles was 30 nm and the substrate was silica glass coated with 20 nm of ITO. The scale bar is 300 nm. [15] (b) TEM images and lateral size as a function of spectral peak wavelength for a diverse collection of individual silver nanoparticles. [16]

This fact implies that $\lambda_{res}$ is highly dependent on particle shape and size [16], which is shown in Fig. 2.3. It is clearly observed that the geometrical shape of a nanoparticle plays a key role in determining the plasmon resonance and the spectrum is red-shifted with increase in the particle size. When the particle size is comparable to or larger than the wavelength, the retardation effect and the excitation of higher-order (quadruple and higher) mode should be considered.

#### 2.1.2.2. A periodic array of nanoparticles

Based on the previous studies of LSPR for a single particle, it is observed that the plasmon resonance strongly depends on the geometric details of the particle as well as the dielectric properties of the particle material and the surrounding medium. For an ensemble of particles, the individual plasmon resonance is additionally modified by the electromagnetic particle interaction. Typically, two types of interactions can be distinguished: near-field coupling and far-field (dipolar) interaction. Near-field coupling is related to nearly touching particles due to the short range of the electromagnetic near fields in the order of some tens of nm [17]. It is found that near-field dipolar interaction between adjacent particles is dominated by a distance dependence of $d^{-3}$ [18]. These strongly distance-dependent interactions can be attributed to Coulombic force interactions between the electrons in neighboring particles.

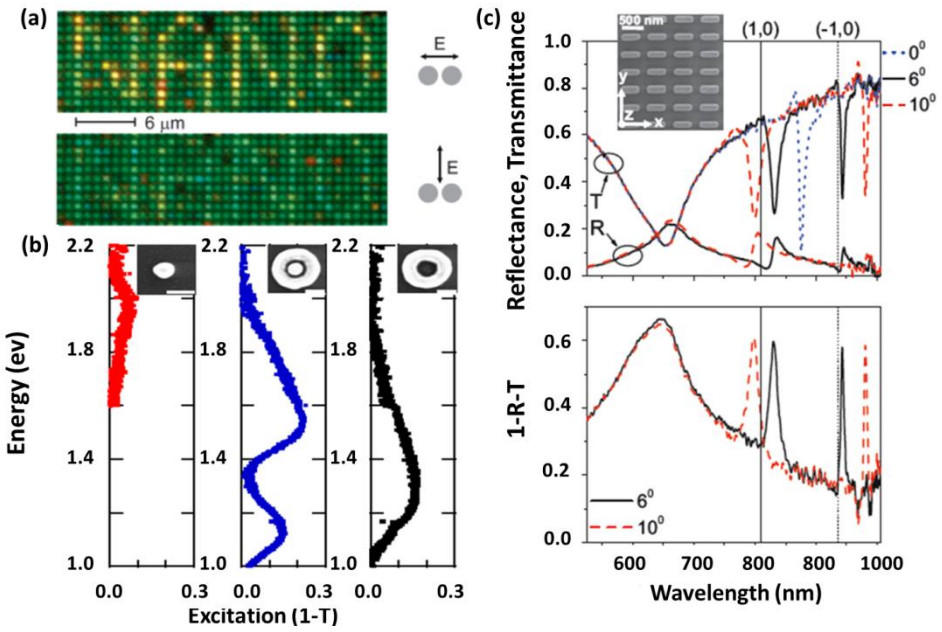


Figure 2.4 (a) Dark-field images of an array of silver particles (80-nm diameter and 25-nm height) in two orthogonal polarization configurations. The text "NANO" is written with pairs of such particles with an interparticle distance of approximately 110 nm. [18] (b) Experimental extinction measurement of single structures, a disk (red solid line), a concentric ring/disk cavity (blue solid line), and ring (black solid line). D_out = 250 nm, D_in = 100 nm, D_disk ≈ 75 nm. The insets show SEM images of the structures, with a scale bar of 100 nm. [20] (c) Transmittance (T) and reflectance (R) from a plasmonic crystal of nanoantennas as a function of wavelength for different angles of incidence, θ = 6 ° (black solid line) and θ=10° (red dashed line), respectively. Inset: SEM image of a plasmonic crystal of nanoantennas. The bottom of the plot is 1-R-T as a function of wavelength for 6 º(black solid line) and 10 ° (red dashed line). [21]

On the other hand, far-field interaction can be generated by the nanostructures' scattered light fields [19]. Nanoparticles forming an array with the interparticle distance exceeding those allowing near-field coupling are thus interacting through their dipolar fields [20], giving rise to the collective radiation. When the plasmon resonance is driven by a periodic array of nanostructures, a strong modification in transmission/extinction characteristics can be observed. A special case can occur under the condition that the distance between nanostructures is equal to the light wavelength. In this case, far-field dipolar interaction acts effectively as a grating, leading to the increased

radiation damping of the collective resonances where the diffraction order changes from the evanescent to the radiative in characteristics [21].

### 2.2. LSPR-based sensors

It has been shown that plasmonic sensing [22] relies either on surface plasmons or localized surface plasmons based on continuous or nanostructured noble metal surfaces to detect molecular-binding events. The exploration and the development of plasmonic sensing are highly desired arising from its promising advantages over other sensing techniques. For example, compared to other molecular sensors, such as nuclear magnetic resonance [23] or x-ray diffraction [24], plasmonic sensors are compatible with liquid environments. Moreover, relative to other single-molecule techniques, such as Forster resonance energy transfers (FRET) between organic dyes, plasmonic sensors are considerably photo-stable, and cover large detection areas, as well as strong optical signals.

The development of LSPR-based sensors has recently attracted considerable attention. The main reason is that these sensors provide simplified detection schemes, accurate sensing sensitivity, and high density multiplexed array configurations [25]. Moreover, LSPR sensors outperform SPR sensors in three aspects. Firstly, the molecules can be easily detected by naked eyes if the resonance shifts of the nanosensors are positioned in UV-visible range of the spectrum. Secondly, the detection limits can be improved by manipulating sizes, shapes, materials and interparticle distances of nanostructures. Thirdly, LSPR-based sensors do not need large sample volumes and could be integrated into a nanochip, which has overcome the

challenging issues that SPR sensors are facing. In this section, we focus on theoretical discussion of the localized surface plasmon sensing and spectroscopy, with special attention on refractive index sensing and surface enhanced Raman spectroscopy (SERS).

### 2.2.1. Refractive index sensing

LSPR-based refractive index sensing is based on the assumption that the LSPR peak wavelength is highly dependent on the dielectric function of the medium. This assumption has been confirmed using the analytical, frequency-dependent form for $\varepsilon$ based on the Drude model [26]. Therefore, the dependence of LSPR peak wavelength on the refractive index needs to be approximately linear at optical frequencies, which can be expressed by the following equation:

$$\lambda_{max} = \lambda_p \sqrt{2{n_m}^2 + 1}\,, \qquad \text{(Eq. 2.9)}$$

where $\lambda_{max}$ is the LSPR peak wavelength, $\lambda_p$ is the wavelength corresponding to the plasma frequency of the bulk metal, and $n_m$ is the refractive index of the surrounding media. The refractive index sensitivity S of a particular nanoparticle type is usually reported in nanometers of peak shift per refractive index unit (nm/RIU) [27].

$$\mathrm{S} = \frac{d_{\lambda_p}}{d_n}\,. \qquad \text{(Eq. 2.10)}$$

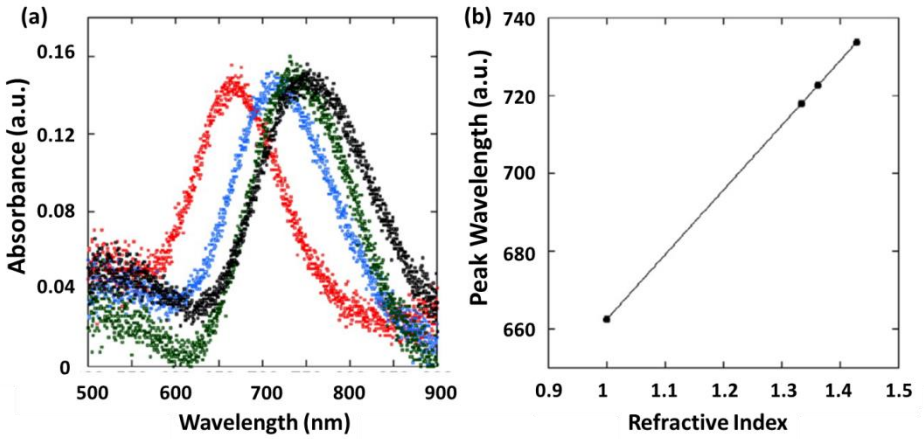


Figure 2.5 (a) Measured optical absorbance of gold nanorod films in air (red dot line), water (blue dot line), ethanol (green dot line), and formamide (black dot line). (b) Plasmon resonance wavelength as a function of the refractive index. The sensitivity (slope) of nanorod film is 170 nm/RIU [28].

An example of this type of sensing [28] is shown in Fig. 2.5 (a) for a gold nanorod film in a series of solvents with different refractive indices: air ($n$ =1.000), water ($n$ =1.333), ethanol ($n$ =1.361), and formamide ($n$ =1.428). It is clearly observed that LSPR resonances can gradually red-shift as the refractive index of the surroundings increases from 1.000 to 1.428. The sensitivity of gold nanorod substrates is calculated by fitting the variation of spectral shifts, which is shown in Fig. 2.5 (b).

### 2.2.2. Surface enhanced Raman spectroscopy

Label-free LSPR sensing is a very useful technique for measuring protein binding kinetics, while it fails to identify bound molecules because they only record refractive index changes. Raman spectroscopy is able to identify unknown bio/chemical molecules in many applications which are highly desired, such as diagnosis, medical therapy and environmental sensing. Surface enhanced Raman spectroscope [29] is firstly applied to observe the

molecules on the roughened silver electrodes. It has been found that a wide variety of substrates can serve as the surface enhanced substrates, consisting of electrochemically modified electrodes, colloids [30], island films [31], and regular particle arrays [32]. Moreover, Raman spectroscopy possesses some distinct advantages compared with other vibrational spectroscopies such as Fourier-transform infrared spectroscopy (FTIR) because Raman transitions that are not IR-active can be probed by using Raman spectroscopy [33]. When Raman spectroscopy is combined with near-field scanning optical microscope (NSOM) for the chemical imaging of a sample, a high-resolution Raman imaging can be obtained, known as tip-enhanced Raman spectroscopy (TERS) [34]. In addition, Raman spectroscopy can perform well in water. On the other hand, there is a strong absorption in the water at the mid-IR range, which may affect the bio/chemical detection in FTIR. For these reasons, Raman spectroscopy has been a valuable analytical technique in physical, chemical and material science.

The challenging issue in Raman spectroscopy is that Raman scattering itself is a very feeble phenomenon, since a typical non-resonant Raman scattering cross-section ($\sim 10^{-30}$ $cm^2$) is about 14-15 orders of magnitude lower than that of fluorescence ($\sim 10^{-15}$ $cm^2$) [35]. However, it has been shown that the Raman signal can be greatly increased (usually around $10^4$ to $10^9$ times) when a molecule is very close to a roughened or nanostructured noble metal substrate. The surface enhanced Raman spectroscopy (SERS) can support both a ‘chemical’ enhancement of roughly 10-100 times and an ‘electromagnetic’ enhancement, due to the excitation of LSPR and large field intensity around metal substrates [33].

The electromagnetic enhancement mechanism can be explained by modeling the roughness as small metallic nanoparticles whose diameters are much smaller than the wavelength of the incident light (Fig 2.6). Under the influence of an external electromagnetic field, the strong local field can be generated due to free electron oscillations from metallic nanoparticles. Such strong field can result in the enhanced Raman signals by many orders of magnitude. In this process, the nanoparticle acts as both a receiver and a transmitter as a result of the intensity being enhanced twice. In particular, the incident field is localized and intensified by the nanoparticle, leading to the intense field seen by the Raman-active molecules (Fig. 2.6 (a)). The nanoparticle provides the strong scattered field (Fig. 2.6 (b)), which can be detected by a Raman spectroscope. Thus, the nanoparticle enhances both incoming and scattered light, resulting in the SERS signal proportional to the fourth power of the electric field.

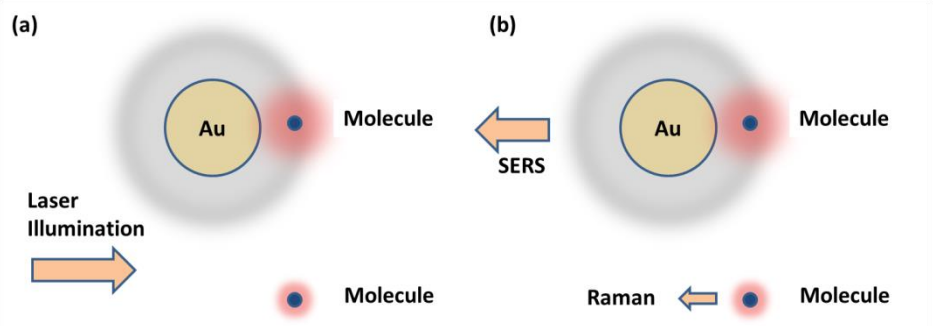


Figure 2.6 A gold nanoparticle enhances both (a) the incident field and (b) the scattered field, greatly increasing the Raman signal from a proximate molecule.

According to the electromagnetic (EM) enhancement, the enhancement factor EF at each molecule is (approximately) given by [33]:

$$EF = |E(\omega)|^2 |E(\omega)'|^2 \,, \qquad \text{(Eq. 2.11)}$$

where $E(\omega)$ is the local electric field enhancement factor at the incident frequency $\omega$ and $|E(\omega)|'$ the corresponding factor at the Stokes shifted frequency $\omega'$. The equation predicts that there is a well-defined relationship between the LSPR spectrum and the surface enhanced Raman excitation spectrum of a SERS active surface. In particular, the magnitude of the enhancement factor can be optimized by tailoring the size, shape, interparticle distance and local dielectric environment of the nanoparticles [36]. One of the most effective approaches to optimize the magnitude of the Raman scattering is to ensure that the LSPR wavelength can match well with the excitation wavelength of the laser beam and also overlap with an electronic absorption band of interest [37]. The Raman scattering intensity of this vibration mode can be effectively amplified by metallic nanostructures. Therefore, tuning LSPR resonance wavelength of SERS substrates in a specific range is of great importance to enhance Raman scattering of the molecules.

### 2.3. Laser interference lithography (LIL)

In this section, we explain how the plasmonic nanostructures can be prepared by laser interference lithography (LIL) over a large area. In this maskless lithography technique, the standing wave pattern is used to expose a photoresist layer. We will introduce the fundamental concepts on the interference lithography and then discuss some important factors that can be applied to complex plasmonic nanostructures.

### 2.3.1. Working principle

LIL is a maskless and non-contact nanofabrication technique. With only a few minutes of the light exposure followed by photoresist develop and chemical etching, periodic nanoline and nanodot array can be created over a large area on the centimeter scale [38]. The principle of this technique is based on the interference of two coherent light beams to form a horizontal standing wave pattern, as shown in Fig. 2.7 (a).

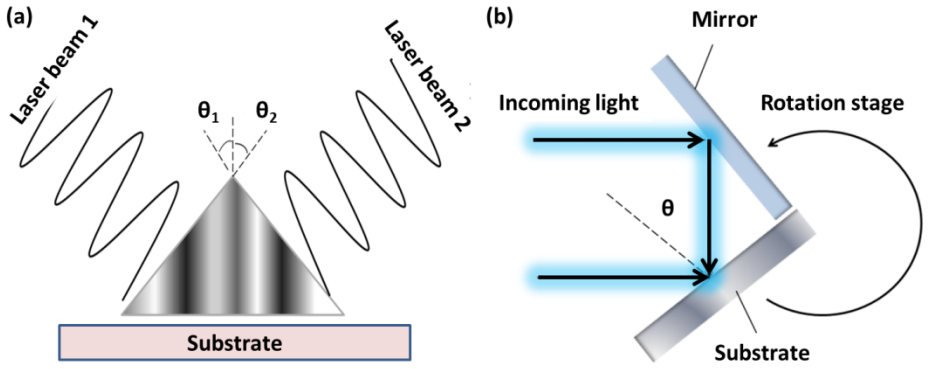


Figure 2.7 (a) Principle of two laser beam interference. (b) Schematic diagram of Lloyd's mirror interferometer.

The intensity and phase relation result in a holographic pattern consisting of dark and bright spots which can be expressed as [39]:

$$I_r = I_1 + I_2 + 2\sqrt{I_1 I_2} \times cos\varphi \ , \qquad \text{(Eq. 2.12)}$$

where $I_r$ is the intensity of the beam spot, and $\varphi$ is the phase difference between the two beams. The phase difference $\varphi$ is due to the angle between the two coherent laser beams. For the two-beam interference, the standing wave forms a grating pattern with a well-defined spacing $\Lambda$:

$$\Lambda = \frac{\lambda}{\sin(\theta_1)+\sin(\theta_2)}, \quad \text{(Eq. 2.13)}$$

where λ is the laser wavelength, $\theta_1$ and $\theta_2$ are angles between the normal of the exposed surface and the beams 1 and 2.

A simple setup to realize LIL is a two-beam Lloyd's mirror interferometer[39], which is shown in Fig. 2.7 (b). It allows for the large scale fabrication of nanostructures combined with the fast alignment and easily adjustable pattern sizes compared to other interferometers. For the Lloyd's mirror interferometer, the period (Λ) of the standing wave is given as below:

$$\Lambda = \frac{\lambda}{2sin\theta}, \quad \text{(Eq. 2.14)}$$

where λ is the light wavelength, and $\theta$ is the half angle at which the two beams intersect. This equation indicates that the period of nanostructures can be controlled and reduced by increasing the incident angle during the LIL exposure.

### 2.3.2. Multi-exposure

Using a two-beam Lloyd's interferometer, a single exposure creates a line pattern. To form a more complex pattern, more than one exposure is needed. Combining the Lloyd's mirror interferometer with a rotating substrate holder opens a new opportunity to make a variety of nanostructures. Rotating the substrate over an angle α and then exposing the substrate a second time can create new patterns, like two dimensional (2D) structures of pillars or holes in

square [40] or hexagonal lattices [41]. The substrate can be exposed two times, or even many times. Therefore, exposure time, incidence angle $\theta$, and rotation angle $\alpha$, are important factors that affect the pattern. For example, a grating pattern can be generated under a single exposure, while 2D nanodisk or nanohole patterns require double exposures. Moreover, adjustment of the incidence angle can be used to control the period of the pattern (Eq. 2.14), showing that the period is inversely proportional to the incidence angle. In addition, the rotation angle of the substrate holder can be used to control the lattice shape. The experiment to pattern complicate nanostructures will be described in detail in Chapter 3.

## 2.4. Summary

To sum up, this chapter has reviewed the fundamentals of surface plasmons and the localized surface plasmons excited by the single nanoparticle or an array of nanoparticles. The localized surface plasmon-based sensing and spectroscopy are also presented, with special attention on refractive index sensing and surface enhanced Raman spectroscopy. In the latter part of the chapter, a patterning technique, laser interference lithography, is introduced. We describe the working principle of LIL and important factors that influence the patterned structures.

## 2.5. References

[1] R. Zia, J. A. Schuller, A. Chandran and M. L. Brongersma, "Plasmonics: the next chip-scale technology," Mater. Today **9**, 20-27 (2006).

[2] P. Drude, “Zur elektronentheorie der metalle,” Ann. Phys. **3**, 566-613 (1900).

[3] P. Durde, “Zur elektronentheorie der metalle; II teil. galvanomagnetische und thermomagnetische effecte,” Ann. Phys. **3**, 369-402 (1900).

[4] J. B. Pendry, “Negative refraction makes a perfect lens,” Phys. Rev. Lett. **85**, 3966 (2000).

[5] J. Henzie, J. Lee, M. H. Lee, W. Hasan, and T. W. Odom, “Nanofabrication of plasmonic structures,” Annu. Rev. Phys. Chem. **60**, 147-165 (2009).

[6] H. Raether, *Surface plasmons on smooth and rough surface and on grating*, Vol. 111 of Springer tracts in modern physics, Springer-Verlag, Berlin (1988).

[7] A. V. Zayats, and I. I. Smolyaninov, “Near-field photonics: surface plasmon polaritons and localized surface plasmons,” J. Opt. A: Pure Appl. Opt. **5**, S16 (2003).

[8] B. Hecht, H. Bielefeldt, L. Novotny, Y. Inouye, and D. W. Pohl, “Local excitation, scattering and interference of surface plasmons,” Phys. Rev. Lett. **77**, 1889-1892 (1996).

[9] W. Rechberger, A. Hohenau, A. Leitner, J. R. Krenn, B. Lamprecht, F. R. Aussenegg, “Optical properties of two interacting gold nanoparticles,” Opt. Comm. **220**, 137-141 (2003).

[10] U. Kreibig and M. Vollmer, *Optical properties of metal clusters*, Springer Series in Materials Science 25, Springer-Verlag, Heidelberg (1995).

[11] S. A. Maier, *Plasmonics: fundamentals and applications*, Springer, New York (2007).

[12] B. Hecht, H. Bielefeldt, L. Novotny, Y. Inouye, and D. W. Pohl, “Local excitation, scattering, and interference of surface plasmons,” Phys. Rev. Lett. **77**, 1889-1892 (1996).

[13] Z. M. Wang and A. Neogi, *Nanoscale photonics and optoelectronics: science and technology*, Spinger, New York (2010).

[14] J. Homola, “Surface plasmon resonance sensors for detection of chemical and biological species”, Chem. Rev. **108**, 462-493 (2008).

[15] W. A. Murray and W. L. Barnes, “Plasmonic materials,” Adv. Mater. **19**, 3771-3782 (2007).

[16] J. J. Mock, M. Barbic, D. R. Smith, D. A. Schultz, and S. Schultz, “Shape effects in plasmon resonance of individual colloidal silver nanoparticles,” J. Chem. Phys. **116**, 6755 (2002).

[17] J. Homolar, S. S. Yee and G. Gauglitz, “Surface plasmon resonance sensors: review”, Sens. Actuat. B Chem. **54**, 3-15 (1999).

[18] N. A. Janunts, K. S. Baghdasaryan, Kh. V. Nerkarayan, and B. Hecht, “Excitation and superfocusing of surface plasmon polaritons on a silver-coated optical fiber tip”, Opt. Commun. **253**, 118-124 (2005).

[19] L. Salomon, G. Bassou, H. Aourag, J. P. Dufour, F. de Fornel, F. Carcenac, and A. V. Zayats, “Local excitation of surface plasmon polaritons at discontinuities of a metal film: theoretical analysis and optical near-field measurements”, Phys. Rev. B **65**, 125409 (2002).

[20] A. J. Haes, C. L. Haynes, A. D. McFarland, G. C. Schatz, R. P. V. Duyne, and S. Zou, “Plasmonic materials for surface-enhanced sensing and spectroscopy,” MRS Bull. **30**, 368-375 (2005).

[21] G. Vecchi, V. Giannini, and J. G. Rivas, “Surface modes in plasmonic crystals induced by diffractive coupling of nanoantennas,” Phys. Rev. B **80**, 201401 (2009).

[22] T. Endo, K. Kerman, N. Nagatani, H. M. Hiepa, Do-Kyun Kim, Yuji. Yonezawa, K. Nakano, and E. Tamiya, “Multiple label free detection of antigen-antibody reaction using localized surface plasmon resonance-based core-shell structured nanoparticle layer nanochip,” Anal. Chem. **78**, 6465-6475 (2006).

[23] D. R. Bundle, H. Baumann, J. R. Brisson, S. M. Gagne, A. Zdanov, and M. Cygler, “The solution structure of a trisaccharide-antibody complex: comparison of NMR measurements with a crystal structures,” Biochemistry **33**, 5183-5192 (1994).

[24] J. X. Wang, X. W. Sun, A. Wei, Y. Lei, X. P. Cai, C. M. Li and Z. L. Dong, “Zinc oxide nanocomb biosensor for glucose detection,” Appl. Phys. Lett. **88**, 233106 (2006).

[25] A. V. Kabashin, P. Evans, S. Pastkovsky, W. Hendren, G. A. Wurtz, R. Atkinson, P. Pollard, V. A. Podolskiy and A. V. Xayats, “Plasmonic nanorod metamaterials for biosensing,” Nat. Mater. **8**, 867-871 (2009).

[26] K. M. Mayer, and J. H. Hafner, “Localized surface plasmon resonance sensors,” Chem. Rev. **111**, 3828-3857 (2011).

[27] K. M. Mayer, S. Lee, H. W. Liao, B. C. Rostro, A. Fuentes, P. T. Scully, C. L. Nehl, and J. H. Hafner, “A label-free immunoassay based upon localized surface plasmon resonance of gold nanorods,” ACS Nano **4**, 687-692 (2008).

[28] P. K. Jain, W. Y. Huang, and M. A. EI-Sayed, “On the universal scaling behavior of the distance decay of plasmon coupling in metal nanoparticles paris: a plasmon ruler equation,” Nano Lett. **7**, 2080-2088 (2007).

[29] D. L. Jeanmaire and R. P. Van Duyne, “Surface Raman electrochemistry. Part 1. Heterocyclic, aromatic and aliphatic amines adsorbed on the anodized silver electrode,” J. Electroanal. Chem. **84**, 1-20 (1977).

[30] J. A. Creighton, C. G. Blatchford, and M. G. Albrecht, “Surface enhanced Raman scattering (SERS) by molecules adsorbed at spherical particles: errata,” J. Chem. Soc. **75**, 790 (1980).

[31] D. A. Weitz, S. Garoff, and T. J. Gramila, “Excitation spectra of surface-enhanced Raman scattering on silver-island films,” Opt. Lett. **7**, 168 (1982).

[32] N. Felidj, J. Aubard, G. Levi, J. R. Kreen, G. Schilder, A. Leitner, and F. R. Aussenegg, “Enhanced substrate-induced coupling in two-dimensional gold nanoparticle arrays,” Phys. Rev. B **66**, 245407 (2002).

[33] M. Moskovits, “Surface-enhance spectroscopy,” Rev. Mod. Phys. **57**, 783 (1985).

[34] S. Kawata and V. M. Shalaev, *Tip enhancement, Advances in nano-optics and nano-photonics*, Elsevier, Amsterdam (2007).

[35] C. L. Haynes, A. D. McFarland, R. P. Van Duyne, “Surface-enhanced Raman spectroscopy,” Anal. Chem. **77**, 338a-346a (2005).

[36] S. Lal, N. K. Grady, J. Kundu, C. S. Levin, J. B. Lassiter, and N. J. Halas, “Tailoring plasmonic substrates for surface enhanced spectroscopies,” Chem. Soc. Rev. **37**, 898-911 (2008).

[37] N. Felidj, J. Aubard, and G. Levi, J. R. Krenn, A. Hohenau, G. Schider, A. Leitner, and F. R. Aussenegg, "Optimized surface-enhanced Raman scattering on gold nanoparticle arrays," App. Phys. Lett. **82**, 3095 (2003).

[38] J. D. Boor, N. Geyer, U. Gosele, and V. Schmidt, "Three-beam interference lithography: upgrading a Lloyd's interferometer for single-exposure hexagonal patterning," Opt. Lett. **34**, 1783-1785 (2009).

[39] S. C. Kitson, W. L. Barnes, and J. R. Sambles, "The fabrication of submicron hexagonal arrays using multiple-exposure optical interferometry," IEEE Photon. Technol. Lett. **8**, 1662-1664 (1996).

[40] C. H. Liu, M. H. Hong, H. W. Cheung, F. Zhang, Z. Q. Huang, L. S. Tan, and T. S. A. Hor, "Bimetallic structure fabricated by laser interference lithography by tuning surface plasmon resonance," Opt. Express **16**, 10701-10709 (2008).

[41] T. B. O'Reilly, and Henry I. Smith, "Linewidth uniformity in Lloyd's mirror interference lithography systems," J. Vac. Sci. Technol. B **26**, 2131-2134 (2008).

# Chapter 3 Experimental Techniques

In this chapter, the experimental procedures carried out in this research will be described in detail. This chapter is divided into three main parts: fabrication, characterization and simulation. In particular, laser interference lithography (LIL), as one of the most important steps in the fabrication process, will be described. Secondly, the methods employed for the characterization of the structure will be discussed, namely scanning electron microscope (SEM), atomic force microscopy (AFM), UV-Vis-NIR spectroscopy, variable angle spectroscopic ellipsometry (VASE), and Raman spectroscopy. The simulation presented in the third part is carried out using the finite difference time domain (FDTD) method (Lumerical software).

## 3.1. Fabrication techniques

### 3.1.1. Fabrication Process

It has been shown that top-down lithography plays an important role in the fabrication of two-dimensional (2D) nanostructures in parallel. In general, the fabrication process is commonly separated into five main steps: (1) coating a substrate with the photoresist, (2) exposing the photoresist to the interference pattern of two coherent laser beams, (3) developing the patterned photoresist with a developer, (4) depositing metals on the patterned photoresist, and (5) transferring the pattern to the substrate by lift-off or metal etching. This

procedure is schematically illustrated in Fig. 3.1. In the following section, critical issues and the related experimental results will be described.

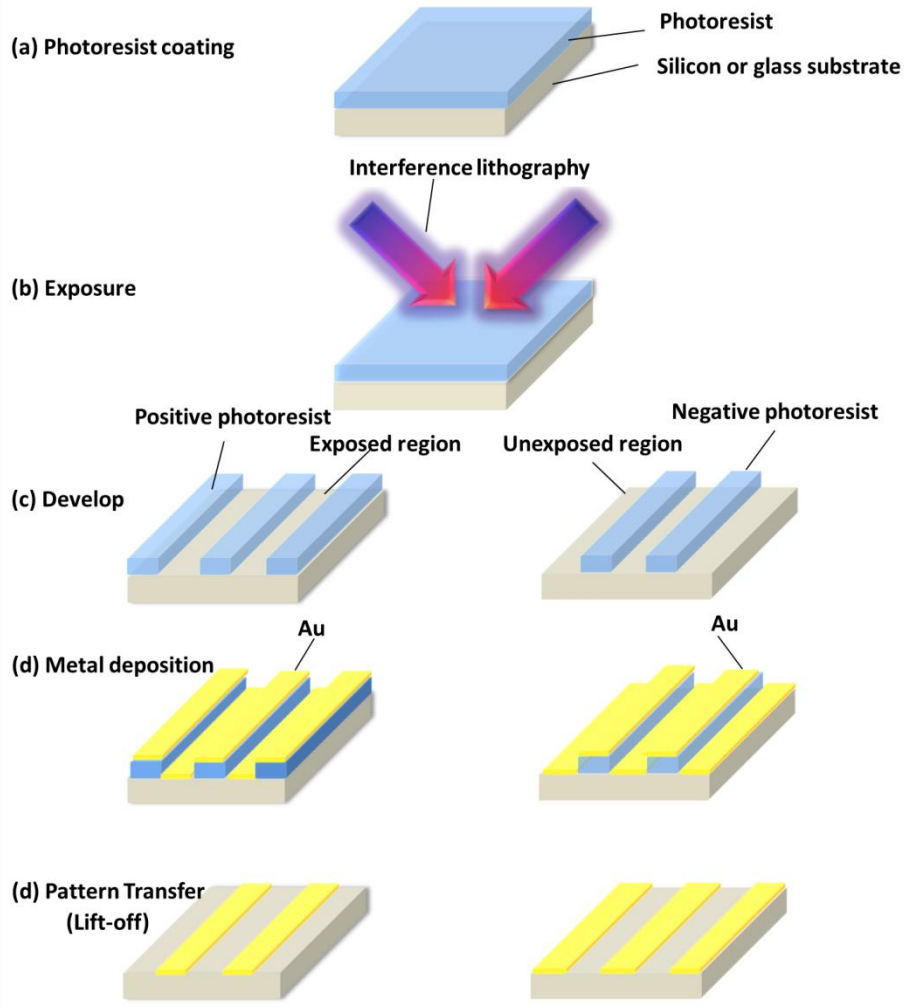


Figure 3.1 Schematic diagram of the fabrication process of metallic nanostructures.

### 3.1.2. Sample cleaning

The objective of sample cleaning is to remove organic and inorganic dust particles or other debris from the substrate, providing a clean surface for the photoresist coating process. Sample cleaning is of great importance for the photoresist coating. It determines the uniformity of the generated

nanostructures. The photoresist may be peeled off from the substrate if the substrate surface is not clean enough. Therefore, the standard wafer cleaning process is applied to clean the substrates. The substrate is processed in sequence for 30 minutes of cleaning by using acetone, isopropyl alcohol (IPA) and de-ionized (DI) water in an ultrasonic bath to remove the contaminants, and then dried by blowing with pure nitrogen ($N_2$) gas.

### 3.1.3. Photoresist coating

Photoresist coating is the process of uniformly covering a substrate with a light sensitive film. Typically, the function of the photoresist is to generate a pattern precisely under the illumination of light (e.g., UV light, or laser beam), and to serve as a mask for the metal pattern transferred to the substrate. A difference is made between (1) positive photoresist where the exposed area is removed by the developer and (2) negative photoresist where the exposed area is retained by the developer. The photoresists used in this study are N1405 (negative photoresist) and S1805 (positive photoresist).

The photoresist coating process follows the protocol provided by the manufacture, Microchemicals [1]. It consists of three main steps: (1) HMDS coating to improve the adhesion of photoresist to the substrate; (2) spin coating a uniform resist layer; and (3) soft baking to further increase the adhesion and also to remove solvents.

Coating a uniform layer of the photoresist needs two steps: (1) low spin speed (500 rpm) with short spinning time (5 s) as the first step, which can prevent the resist from tearing off the substrate. The next step is to (2) use a high spining speed (5000 rpm) for a long spinning time (50 s), which can lead

to the solvent being evaporated completely so as to obtain the desirable thickness of the film. In this study, the resist thickness is measured by using a surface profile to ensure the consistency in the thickness.

A soft-baking process follows the spin coating. This process prevents the popping or foaming of the resist, improves the adhesion to the substrate, and minimizes dark erosion during the photoresist development [2]. In our study, the hotplate's temperature is fixed at 100 $^{0}$C and the duration of the soft baking is 60 s. The baking time is adjusted depending on the substrate type (e.g. silicon or glass substrates).

### 3.1.4. Laser interference lithography

Laser interference lithography (LIL) provides rich opportunities to fabricate periodic micro/nano-structures over large areas [3]. When compared to other top-down nanofabrication techniques, such as EBL or FIB, the advantages of LIL are low cost, high speed and large fabrication areas. In this study, the exposure process is performed via a standing wave formed by the interference of two coherent laser beams. The bright fringes are then recorded on the coated photoresist layer. The Lloyd's mirror setup is applied to generate plasmonic nanostructures because of the fast alignment and easily adjustable pattern sizes compared to other interferometers.

#### 3.1.4.1. Lloyd's mirror setup

In this work, Lloyd's mirror interferometer is used for the lithographic exposure. The interferometer consists of an aluminum mirror (5 cm × 5 cm)

with a high reflectivity (> 92%) for the Helium-Cadmium (He-Cd) laser, which is mounted perpendicular to the sample holder. The aluminum mirror is selected because of its enhanced UV reflectivity compared to other mirrors. Our interferometer is designed for substrates with a dimension of 2 cm × 2 cm. One could expect large exposure areas up to 4 or 8 inches if a large mirror and a high power laser are used.

A simplified diagram of the optical setup is shown in Fig. 3.2. In this work, the continuous wave (CW) He-Cd laser has an average output power of 40 mW and a long coherence length of 10 cm. The laser is optically filtered through a UV objective lens and a pinhole with a diameter of 5 μm, which removes high spatial-frequency noise, thus forming a near-Gaussian beam. Lloyd's mirror interferometer consists of three parts: (1) a mirror, (2) a rotation stage and (3) a sample holder, which is placed in a distance of around 1 meter away from the spatial filter. The whole setup is built on an actively damped optical table of 1.5 m × 2.5 m to avoid vibrations.

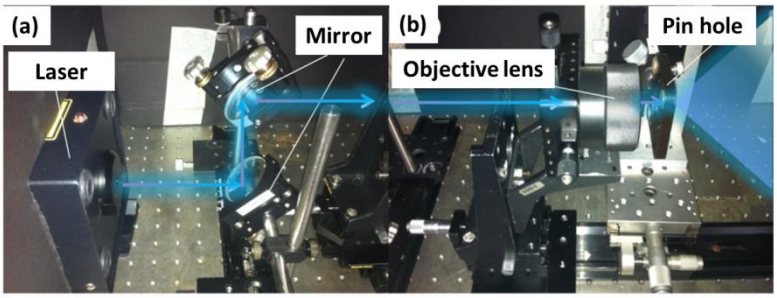


Figure 3.2 Photographs of (a) He-Cd laser, mirrors and (b) the spatial filter (objective lens and pinhole with 5 μm in a diameter).

The expanded laser beam is spatially filtered through a pinhole in order to generate a coherent beam with a diameter of 8 cm at the interferometer. The light illuminates both the mirror and the sample. One part of the beam is

reflected from the mirror surface and interferes with the other part of the beam that is directly illuminating the sample. This interference provides a pattern with a periodicity given by $\lambda/2\sin(\theta)$, where λ is the wavelength of the laser beam (325 nm for He-Cd laser), and $\theta$ is the incidence angle between the incident light and the sample normal. By tuning the angle $\theta$ the rotation stage, the periodicity of the pattern is easily varied from 500 nm to 1.5 μm.

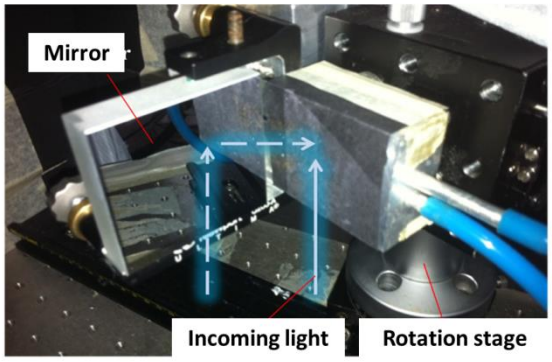


Figure 3.3 Photograph of Lloyd's mirror interferometer setup. The angle between the mirror and sample stage is fixed at 90 °.

### 3.1.4.2. LIL exposure

The objective of LIL exposure is to directly transfer a geometric pattern to a light-sensitive photoresist. Double exposure is applied to form periodic nanodisk arrays. The subsequent cross exposure of the photoresist can generate nano-hole arrays on the substrate surface by rotating the sample by 90 ° when the negative photoresist is applied. The geometry of the patterned nanohole arrays is highly dependent on not only the incident angle of the incoming beam, but also the exposure dose which is given by the product of the exposure intensity and the exposure time. The exposure time of the photoresist layer has to be well controlled. The reason is that different

exposure time generates different shapes of photoresist (Fig 3.4), which displays the SEM images of a negative photoresist. The photoresist has been exposed by LIL at the incident angle of 18 ° for 120 s. The main figure shows the top-view of the patterned photoresist, while the cross-sectional view is inserted in the bottom-left side to indicate the sidewall profile of the exposed photoresist. It can be seen that the morphology of the photoresist (top-view) indicates that the exposed area is cross-linked and retained on the substrate, while the unexposed area is removed by the developer, leaving a periodical nanohole array on the glass substrate. In this case, the period of the nanohole array is ~ 520 nm as an incident angle of 18 ° is used. The nanoholes have a diameter of around 250 nm, which is almost a half-size of the period. Furthermore, SEM image of nanohole arrays (cross-sectional view) displays the trapezoid shape with three ripples on the sidewall of the resist with a height of around 300 nm. The sidewall profile of the photoresist can be further improved by adding an extra anti-reflection layer between the glass surface and the photoresist. This process can suppress the secondary reflection and enable a steep resist profile in the photoresist [4].

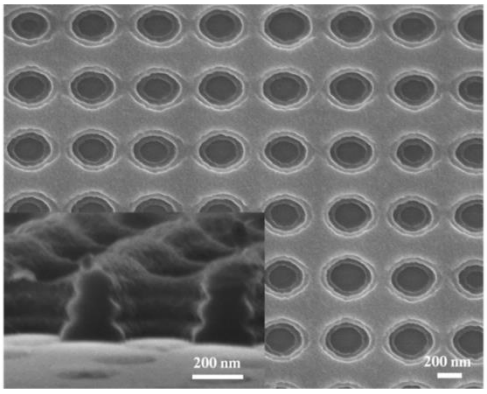


Figure 3.4 Morphology of the negative photoresist formed by LIL at an incident angle of 18 °with a rotation angle of 90 °for the second exposure. The main figure shows the SEM image of the patterned nanohole arrays (top-view), and its SEM image (cross-sectional view) is inserted in the bottom-left side.

There is another situation that a short exposure time is used. In this case, the photoresist is cross-linked and only the area where two intensity maxima overlap receives a total dose that exceeds the threshold value of the resist. This phenomenon results in “saddle points” in the patterned photoresist [4], leaving the rest of the negative resist as sharp edged nanopillar arrays on the substrate.

Figure 3.5 displays the difference in the geometry of Au nanostructures transferred by the negative photoresist with good-exposure (120 s) and short-exposure time (30 s), respectively. The exposure intensity is simulated by using Matlab, which is plotted in Fig. 3.5 (a). When the negative resist is exposed well, Au nanodisk arrays can be obtained (Fig. 3.5 (c)). On the contrary, when the exposure time is not long enough, the area of medium intensity is developed by chemicals, forming nanodiamond pillars on the substrate shown in Fig. 3.5 (b). After the metal transfer, Au nanodiamond hole arrays with sharp edges can be generated via a lift-off process (Fig. 3.5 (d)).

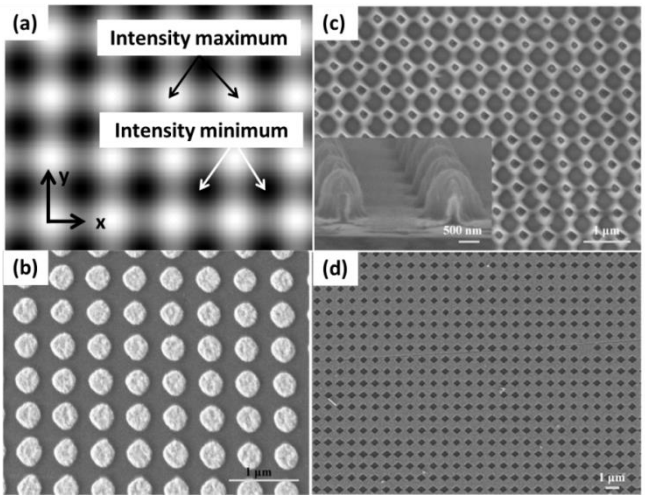


Figure 3.5 (a) Simulated intensity distribution of UV light exposed to the photoresist layer twice with the rotation angle (α) of $90^0$. (b) SEM image of Au nanodisk arrays exposed twice by LIL for 120 s each. (c) SEM images of negative photoresist exposed twice by LIL for 30 s each. The cross-sectional view of the resist sidewall is inserted in the bottom-left side. (d) SEM image of Au nanodiamond arrays obtained by the resist exposed twice by LIL for 30 s each.

### 3.1.4.3. Photoresist development

The objective of the photoresist development is to pattern the photoresist coated on the glass surface by removing the exposed area (positive photoresist) or the unexposed area (negative photoresist) with chemicals. In our experiment, the development is carried out using md-533s for negative resist N1405, or md-319s for positive resist S1805. During the development process, the exposed sample is immersed inside the developer for 30 s, moved out and then flushed by DI water. Finally, the sample is dried with nitrogen ($N_2$) gas.

### 3.1.4.4. Tuning the period of nanohole arrays in the photoresist

The period of the nanohole arrays in the photoresist can be adjusted through tuning the incident angle of the incoming beam. Figure 3.6 shows the

approach used to generate nanorod hole arrays with two different lattice periods in *x* and *y* directions. In Fig. 3.6 (a), the dark area indicates the minimum intensity exposed by LIL, while the bright area indicates the maximum intensity exposed by LIL. The incident angle ($\theta$) is reduced for the second exposure through tuning the rotation stage (Fig 3.6 (b)), leading to a larger lattice period of nanohole arrays in *y* direction (Fig. 3.6 (c)). Therefore, Au nanorod array with two different lattice periods in *x* and *y* directions is formed (Fig. 3.6 (d)).

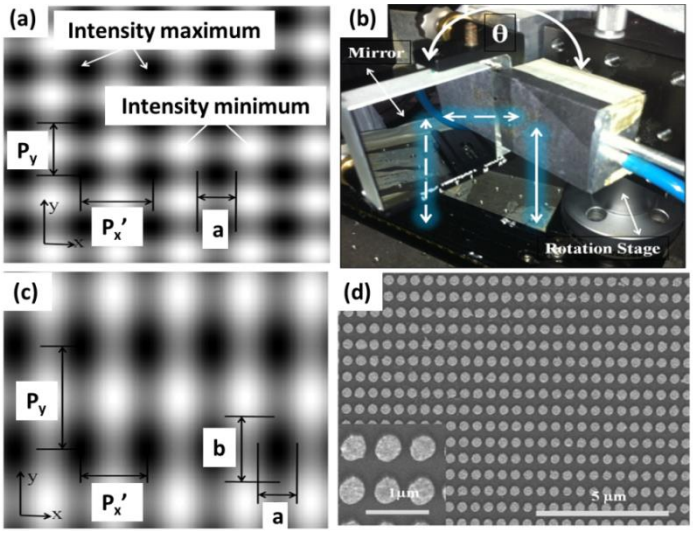


Figure 3.6 (a) Simulated intensity distribution of UV light in photoresist layer exposed twice to form a fringe pattern under the same incident angle ($\theta$). (b) Photograph of Lloyd's mirror interferometer to tune the incident angle of the incoming beam. (c) Simulated intensity distribution of UV light in photoresist layer exposed twice under incident angles ($\theta$ and $\theta'$, where $\theta < \theta'$). (d) SEM image of Au nanorod array formed by LIL after the pattern transfer via the lift-off process.

### 3.1.4.5. Tuning the lattice shape of photoresist by the rotation angle

Reducing the incidence angle at the second exposure to the Lloyd's mirror interferometer can form an array of nanorod arranged in the rectangular lattice

shape. Sometimes hexagonal lattice arrangement is required in the study of spin-coupling. Tuning the rotation angle ($\alpha$) of the sample for the second exposure by LIL can achieve this target.

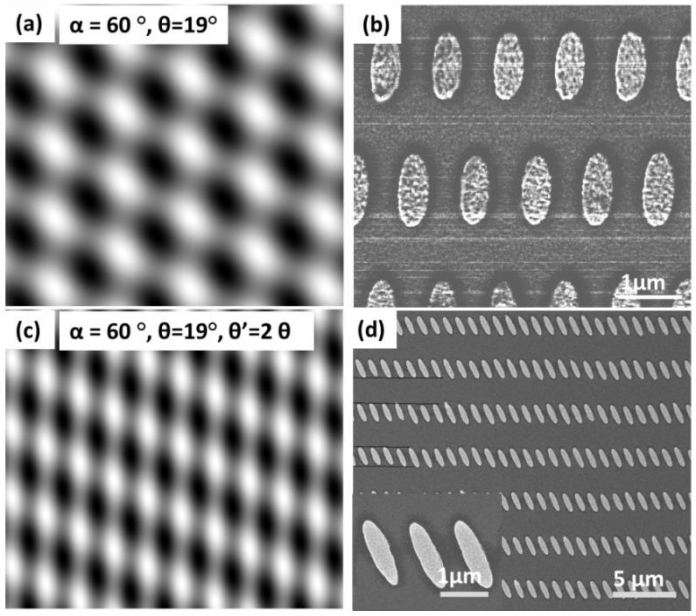


Figure 3.7 (a) Simulated intensity distribution of the photoresist layer exposed twice under the rotation angle ($\alpha$) of 60 °. (b) Corresponding SEM image of nanorod array with hexagonal lattice formed by LIL: $\theta$ = 19 °, $\alpha$ = 60 ° (c) Simulated intensity distribution of the photoresist exposed twice under different incident angles ($\theta$ and $\theta'$) and the rotation angle: $\theta$ = 19 °, $\theta'$ = 38 °, and $\alpha$ = 60 °. (d) Corresponding SEM image of Au nanorod array after the pattern transfer: $\theta$ = 8 °, $\theta'$ = 12 °, and $\alpha$ = 60 °.

The rotation angle in our study is defined as the angle that is used to place the sample on the sample holder for the second exposure through the Lloyd's mirror interferometer. Typically, the rotation angle is 90 ° to form nanodisk arrays in the square lattice arrangement. One can expect to use the rotation angle of 60 °in order to generate nanodisk arrays in hexagonal lattice shape. In this case, the simulated intensity distribution and the corresponding SEM image are shown in Figs 3.7 (a) and (b). Moreover, a complex nanorod array

with a special lattice arrangement can be formed by tuning both the incidence angle ($\theta$) and the rotation angle ($\alpha$) together (Figs. 3.7 (c) and (d)).

### 3.1.5. RIE etching

Reactive-ion etching (RIE) [5] is one of most popular dry plasma etching processes that include the plasma and the sputter etching processes together. Plasma systems are used to ionize reactive gasses and accelerate ions to bombard the surface. Highly anisotropic etching occurs together with the chemical reaction and the momentum transfer process from the etching species. By introducing an asymmetry into the system, a self-bias between the electrodes is produced, which provides the acceleration potential to direct the ions towards the wafer surface. In Fig. 3.8, the surface area of the upper electrode is made larger than one of the lower electrodes. The bottom electrode is now grounded and the wafer is placed on the electrode, which is driven by the RF source.

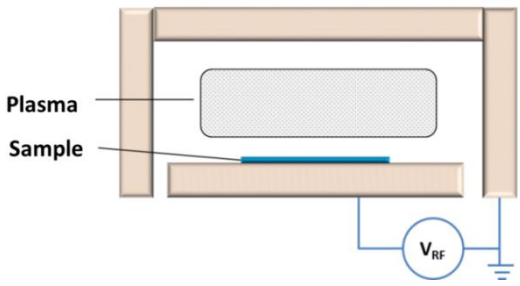


Figure 3.8 Schematic diagram of the reactive ion etching (RIE) system.

In our research, RIE is used to modify sidewall profile of the photoresist after LIL multi-exposure. As seen in Fig. 3.4, a ragged line edge of the

sidewall is shown due to the internal reflection from the bottom layer of the substrate. RIE etching is required for the patterned resist, resulting in two benefits for the fabrication process [6,7]: (1) improving the resist sidewall profile, and (2) removing the unexposed resist from substrate. Figure 3.9 shows a fabrication process of the photoresist etching after LIL exposure. According to our experience, the sidewall of the photoresist has a trapezoid shape with a base angle of around 80 °, which is shown in Fig. 3.4. For nanostructures of a period smaller than 800 nm, the exposure intensity is dramatically decreased with an increase of the incidence angle. The reduced exposure intensity can lead to the worst sidewall performance of the resist, leading the resist being difficult to be lifted off. Therefore, using RIE to etch the unexposed resist using $O_2$ gas is necessary. The etching time is from 15 to 30 s.

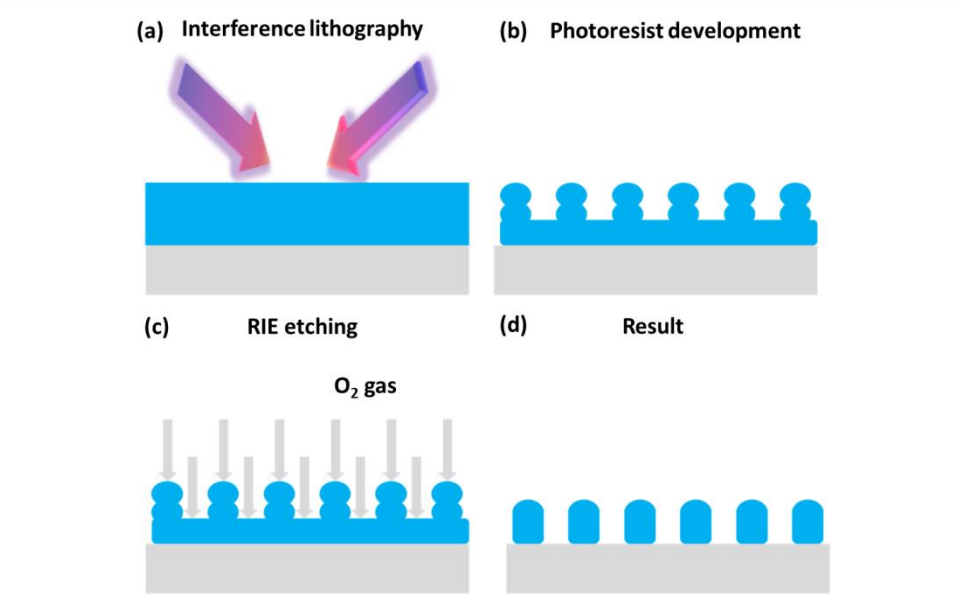


Figure 3.9 Process steps for photoresist lithography with RIE etching. The photoresist is exposed by LIL, developed, and then reactive ion etched in $O_2$ gas.

### 3.1.6. Electron beam evaporation

In our experiment, electron beam evaporation is a process employed to deposit metal films on the patterned photoresist, which is one step in the pattern transfer process. The electron beam evaporation process uses a focused electron beam to heat the metal for the deposition [8,9]. A wide variety of materials can be deposited using solid sources, including metals (e.g. Au, Ag, Al, Cr, and Cu), alloys or dielectric materials (e.g. $SiO_2$, $TiO_2$, and Si). A controlled deposition of thin films is achieved. In our study, a 2 nm thick Cr film is firstly coated on the photoresist mask, which offers a good adhesion between the metal layer and glass substrate. Au or Ag films are coated subsequently. In order to obtain a smooth film surface, coating rates of metallic thin films are fixed at around 0.02-0.04 nm/sec in our experiment.

Figure 3.10 displays a schematic diagram of the deposition process using an electron beam evaporator. Firstly, the pressure of the chamber should be pumped to a pressure of $10^{-6}$ Torr or lower. A tungsten filament inside the electron beam gun is heated. Electrons are then emitted from the filament until its temperature is high enough. These electrons are deflected and accelerated towards the material under a magnetic or electric field. When the electron beam strikes the target surface, the kinetic energy is transformed into the thermal energy (heat), allowing the target material to be vaporized. This vaporized beam travels towards the substrate and is then condensed to form a thin coating film.

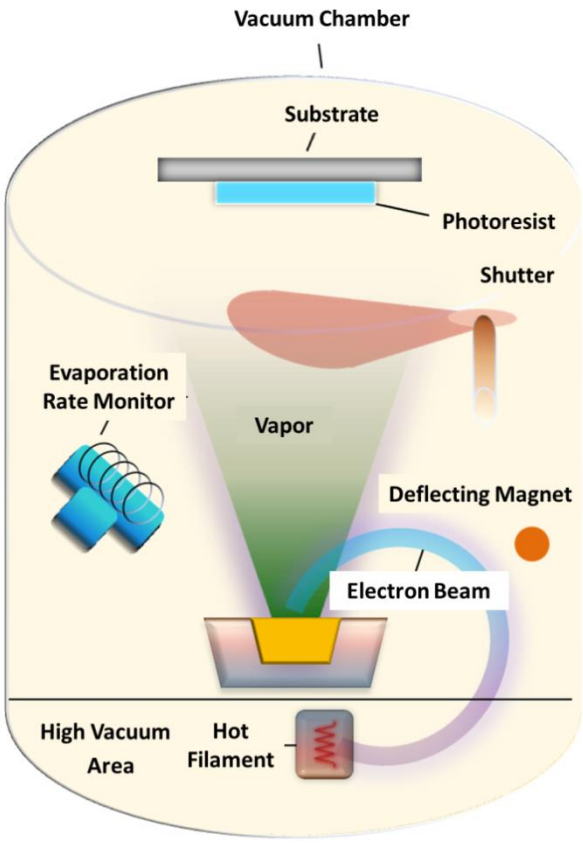


Figure 3.10 Schematic diagram of an electron beam evaporator.

### 3.1.7. Lift-off

Lift-off is a technique to pattern metallic multilayers (such as Cu, Au, Cr, and Ag) in the semiconductor industry due to its promising advantages over other metal pattern techniques [10]: (1) composite layers consisting of several different materials can be deposited at once and transferred to the substrate with a single ‘lift-off’; (2) residues (e.g. the resist or polymer) that are difficult to be removed due to their oxidation in the dry etching process, can be easily avoided in the lift-off; (3) sloped sidewalls become possible. The lift-off process is illustrated in Fig. 3.1. In this drawing, an inverse pattern is formed as a sacrificial layer deposited on a substrate. The metal film is then deposited

both over the layer and in the opening of the pattern by the electron beam evaporation process. Those portions of the metal film deposited on the sacrificial layer are removed, when the substrate is immersed in a suitable solvent, leaving behind the desired metal patterns.

In our experiment, nanodisk or nanorod array are desired. The negative photoresist is selected to form an inverse mask (nanohole arrays), and then metal films (e.g. Cr/Au and Cr/Ag/Au) are deposited by the electron beam evaporator. Lift-off is then performed using acetone and PG remover at room temperature with the help of ultrasonic agitation for a few minutes, leaving metallic nanodisk or nanorod array on the substrates. In the process, in order to obtain a successful lift-off, the ability to ensure the existence of a distinct break is important [11]. The break is a separation between the layer material deposited on top of the resist and the layer material deposited on top of the wafer substrate. Such a separation allows the dissolving liquid to reach and attack the resist. To ensure this distinct break, a thick mask having openings with steep and high sidewalls is highly demanded. Therefore, N1405 with a thickness of 500 nm is used to generate nanodisk or nanorod array with the thickness of metal films in the range from 10 to 40 nm, allowing a good distinct break for a clean lift-off.

### 3.1.8. Thermal annealing

Thermal annealing is a process used for the intrinsic stress liberation, the improvement of structures, and the control of the surface roughness in the material [12]. In recent nanofabrication techniques, thermal annealing is a straightforward method to pattern isolated islands or metallic nanoparticles

from a continuous film through the dewetting of thin films at elevated annealing temperatures [13,14]. When a metallic thin film is heated up until the temperature is high enough to reach the melting point, the metal layer becomes the nucleation of holes, which extends through the film to the substrate surface [15]. In this step, the heating process provides the thermal energy to form the agglomeration of thin metal film. It plays an important role in the fabrication, since the control of the related dewetting parameters (e.g. annealing ambient, temperature and duration) can directly affect size and distribution of metallic nanoparticles [16,17].

In this study, thermal annealing is carried out either in a room environment by a high-temperature furnace (HTCT 01/14 of Nabertherm, Germany) or in argon gas ambient by a horizontal tube vacuum furnace (Carbolite 1200C burn-off furnace). The heating temperature is varied from 200 to 800 ℃. This technique is applied as a post-process to generate quasi-ordered nanodot array after the LIL, which will be demonstrated in Chapter 4.

### 3.2. Characterization

In this thesis, the characterization involves two main types: imaging and spectroscopy. For the imaging part, scanning electron microscopy (SEM) and atomic force microscopy (AFM) are applied to obtain two-dimensional (2D) and three-dimensional (3D) images of the fabricated nanostructures. It provides the detailed information about the geometry of the prepared plasmonic nanostructures and interparticle distances among them. The geometric data obtained by SEM or AFM is necessary for the simulation. The other type is spectroscopies, which are used to measure the optical properties

of plasmonic nanostructures. These methods provide information related to resonance wavelength, intensity, and linewidth of the spectrum. In particular, transmission spectra of nanodisk and nanodot structures are measured by UV-Visible Near-Infrared spectroscopy (UV-Vis-NIR spectroscopy), while variable angle spectroscopic ellipsometry (VASE) is employed to measure nanorod array under different light polarizations. Raman spectroscopy is also used to observe vibrations of the chemical molecules. Brief introductions of these devices are summarized in this section.

### 3.2.1. Scanning electron microscopy

SEM is one of the most frequently used techniques to retrieve the samples' surface morphology information using electrons [18]. It provides a highly magnified view of a surface topology down to the nanoscale. In general, in order to generate a large and stable current in a small beam, two classes of emission sources are discussed here: thermionic emitter and field emitter. Thermionic emitter uses electrical current to heat up a filament. The electrons escape from the filament when the heat is high enough. Thermionic sources have some drawbacks, such as low brightness, evaporation of the cathode materials and thermal drift during the operation. Field emission is an alternative way to overcome these issues. A field emission source (FES) (called as a cold cathode field emitter) does not heat the filament. The emission is performed by placing the filament in a huge electrical potential gradient. The FES is usually a wire of Tungsten (W) fashioned into a sharp point. The significance of the small tip radius (~100 nm) is to concentrate an electric field at an extreme level so that these electrons can leave the cathode.

FESEM can produce a clean image, less electrostatic distortion and spatial resolution reaching to 2 nm [19].

Figure 3.11 displays a schematic diagram of FESEM. The setup comprises of two main parts: an electron column and an electron detection. In the electron column, an electron cathode generates an electron beam. The beam is collimated by electromagnetic condenser lenses, focused by an objective lens, and then rastered across the sample surface by the scanning coils. Secondary electrons and backscattered electrons are emitted from the specimen at the irradiated spot of the primary electron beam, so they are collected by the detector and form the specimen image on the screen of the microscope [20].

The field emission scanning electron microscope (FESEM JSM-7401F) was used to characterize the high resolution topography images of interested samples. The sample is firstly loaded inside the chamber and the vacuum pressure is pumped down to $2.8 \times 10^{-4}$ Torr. The accelerating voltage can be tuned in a range from 5 to 30 kV, and the magnification factor can vary from 20 to 300, 000. As the image of samples is captured by the reflected electrons, a low accelerating voltage (1~3 kV) and a long working distance (8 mm) are applied for non-conductive materials (e.g. quartz). It helps to suppress charging from the surface of the specimen where the irradiated electrons are accumulated. On the other hand, a high accelerating voltage (10 kV) and a short working distance (6 mm) are used for a conductive substrate (e.g. silicon wafer) to obtain a high resolution image with resolution up to a few nanometers. Alternatively, coating a thin Pt or Au film at a thickness of ~5 nm on the sample by a sputtering machine or an electron beam evaporator can

avoid the charging effect, but these samples are contaminated by adding an extra-layer of other metal thin films.

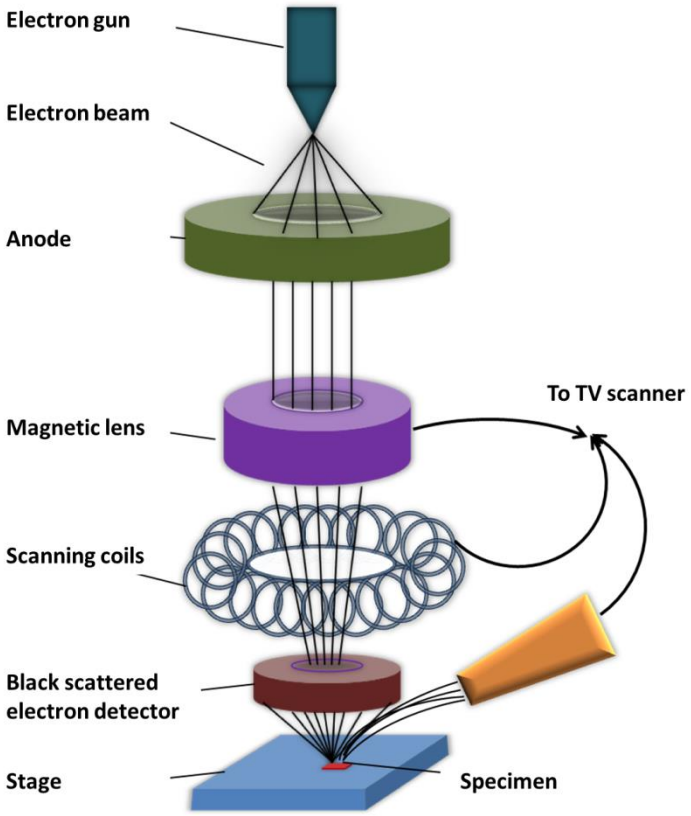


Figure 3.11 Schematic drawing of a scanning electron microscope.

### 3.2.2. Atomic force microscopy

SEM can be a good technique to image 2D samples, but may be not helpful in characterization of samples in three-dimension (3D). Atomic force microscopy (AFM) can provide measurements in all three dimensions, including height information with a vertical resolution of 0.5Å. AFM operates by using attractive or repulsive forces between a tip and the sample. The tips typically have an end radius of 2 to 20 nm, depending on the tip type [21]. During sample scanning, the AFM tip is able to probe an extremely small

interaction area by using a tip radius, which gives a high sensitivity to small forces. To make these forces accessible, the tip is suspended on a soft spring, known as the AFM cantilever. In AFM imaging modes, the cantilever is usually scanned over the surface to produce a 3D image of the surface. In our study, AFM is used to obtain the height information of plasmonic nanostructures. The model used in this project is DI 3100 from Veeco instrument, which allows a vertical resolution of 1 Å.

### 3.2.3. UV-Vis-NIR spectroscopy

Plasmonic nanostructures can generate intense electromagnetic fields propagating or localized around nanostructures, arising from the strong light-matter interaction induced by the incident light. These optical properties consisting of resonance intensity, resonance wavelength and the spectral shape can be systematically explored by a UV-Vis-NIR spectroscope. Recording down the transmission, absorbance or reflectance of the nanostructures helps us to understand the physics better, thus allowing us to design the functionalized nanostructures. Therefore, a UV-Vis-NIR spectroscope is necessary in this work [22]. It features three detectors and a high-performance double beam to ensure good sensitivity, reduced noise and ultra-low stray light. The schematic diagram is shown in Fig. 3.12. The basic part of the spectrophotometer consists of a light source, a focusing lens, a holder for the sample, a diffraction grating to separate different wavelengths of light, and three detectors. One photomultiplier tube is mainly used for the ultraviolet and visible regions, while InGaAs and PbS detectors for the near infrared region.

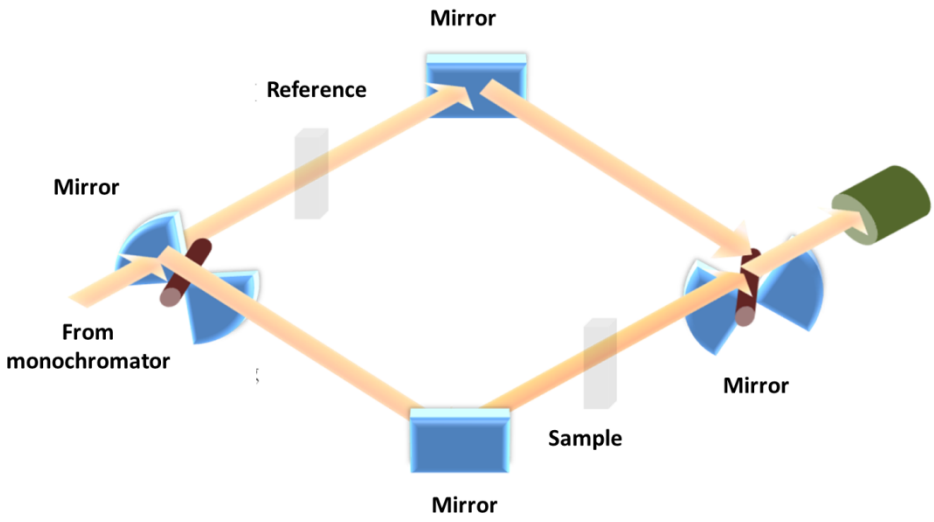


Figure 3.12 Schematic drawing of a dual-beam UV-Vis-NIR spectrophotometer

The light absorbance is expressed as the ratio between the incident radiation ($I_o$) and the transmitted radiation (I), usually expressed as (T%). The absorbance, **A**, is based on the transmittance: $A = -\log(\%T)$. As seen in Fig. 3.12, the light is split into two beams before it reaches the sample. One beam is used as the reference, while the other beam passes through the sample.

For the measurement of reflectance (R%), the reflectance is calculated from the strength ratio after comparing the light reflected from the reference sample with the light reflected from the measurement sample. The reflectance of the reference sample is taken to be 100%, and the reflectance of the sample with respect to this reference is measured.

The measuring mode includes absorbance (Abs), transmittance (T%), reflectance (R%) and energy. The equipment used in our study is UV3600 (Shimadzu), with the working wavelength from 185 nm to 3600 nm.

### 3.2.4. Variable angle spectroscopic ellipsometry

Variable angle spectroscopic ellipsometry (VASE) has been recognized as a highly precise and accurate analytical tool to calculate material parameters from the optical measurement data [23]. The numerous applications of VASE have been explored in the areas of thin films thickness, optical constants (refractive index and extinction coefficient), surface roughness, composition, and the transmission or reflection in variable incident angles. The advantages of VASE measurements are non-contact, non-destructive, and accurate because they measure a ratio quantity (defined as $\tan(\psi) \cdot e^{i\Delta} = \frac{r_p}{r_s}$), where $r_p$ and $r_s$ are the complex Fresnel reflectivities for the p- and s- polarized light. Moreover, the ellipsometry is a polarization-based measurement, providing highly accurate ellipsometric data over a wide spectral and angle range [24].

In our study, the ellipsometer (VASE ellipsometer, J.A. Woollam Co., Inc.) is employed to measure optical properties of nanorod array under the polarized light. This is because both the long and short axes of nanorods can excite longitudinal and transversal resonances, which brings complex spectral information under the un-polarized light. Therefore, VASE is necessary to study the coupling effect for nanorod array under different light polarizations and incident angles. Working wavelength provided by the ellipsometer is from 230 to 1700 nm.

### 3.2.5. Raman spectroscopy

Raman spectroscopy is an important analytical and research tool with wide applications ranging from pharmaceuticals, forensic science, polymers, thin films, and semiconductors [25]. It is a spectroscopic technique to observe vibration, rotation, and other low-frequency modes in systems. Raman scattering occurs when the light interacts with the molecules or is reflected, absorbed or scattered in some manner. Elastic scattering occurs when the photons are scattered with unchanged energy and frequency. On the other hand, inelastic scattering is found when a small number of photons are scattered with diminished or increased energy, hence with lower or higher frequency. The energy associated with the Raman shift is recognized to be the energy responsible for transitions between different rotational and vibrational states of the scattering molecules. In particular, Raman shift can be calculated from the equation $\Delta\omega = (\frac{1}{\lambda_0} - \frac{1}{\lambda_1})$, where $\Delta\omega$ is the Raman shift expressed in wavenumber, $\lambda_0$ is the excitation wavelength, and $\lambda_1$ is Raman spectral wavelength [26]. One of the most challenging issues is that it is hard to observe or detect Raman scattering of the molecules on the substrate. Plasmonic nanostructures can generate intense electromagnetic fields by the excitation of a specific light, allowing the enhancement in Raman intensities of the molecules on the metal surface, which is one of the major applications in the field of plasmonic sensing.

## 3.3. Simulation tool

### 3.3.1. FDTD

In this research, simulation is a useful tool to better understand the interaction between the light and nanostructures, helping us to design nanostructures with desirable optical properties. Several simulation tools, such as effective-medium theory [27], quasi-static calculations [28], or discrete dipole approximation (DDA) [29], have been applied to discover absorption and localized near field energy. Among these simulation, finite-difference time-domain (FDTD) has been well recognized as a good simulation tool to solve the most challenging photonic design problems by solving Maxwell's equations in three dimensions, thus enabling us to analyze the interaction of UV, visible, and IR radiations with complicated structures. Lumerical FDTD software provides graphical user interface (GUI) to set up the same environment with experiment so as to solve different types of problems in electromagnetics and photonics. In addition, it can also obtain frequency solution by exploiting Fourier transforms, thus complex Poynting vector and the transmission/reflection of the light can be calculated. Therefore, FDTD is used to simulate transmittance, reflectance and absorbance of the interested samples. The spatial electric field intensity distribution can also be easily calculated under different light polarizations.

### 3.4. Summary

In this research, laser interference lithography is applied to prepare plasmonic nanostructures. The fabricated nanostructures are then characterized by SEM and AFM for better understanding of their morphologies. The optical properties of nanostructures are measured by two types of spectroscopes: UV-Vis-NIR spectroscope (e.g. under unpolarized light) and VASE (e.g. under different light polarizations). FDTD simulation is carried out to calculate the spectra of resonances, analyze optical responses, and specify electric field intensity distributions.

### 3.5. References

[1] H. Lorenz, M. Despont, N. Fahrni, J. Brugger, P. Vettiger, P. Renaud, "High-aspect-ratio, ultrathick, negative-tone near-UV photoresist and its applications for MEMS", Sensor Actuat. A: Phys. **64**, 33-39 (1998).

[2] E. H. Conradi and D. F. Moore, "SU-8 thick photoresist processing as a functional material for MEMS applications", J. Micromech. Microeng. **12**, 368 (2002).

[3] T. C. Chong, M. H. Hong, L. P. Shi, "Laser precision engineering: from microfabrication to nanoprocessing," Laser & Photon. Rev. **4**, 123-143 (2010).

[4] Q. Xie, M. H. Hong, H. L. Tan, G. X. Chen, L. P. Shi, T. C. Chong, "Fabrication of nanostructures with laser interference lithography," J. Alloy. Compd. **449,** 261-264 (2008).

[5] R. C. Jaeger, *Introduction to microelectronic fabrication: volume 5 of modular series on solid state devices*, 2nd ed., Prentice Hall, New York (2001).

[6] E. H. Anderson, C. M. Horwitz, and H. I. Smith, "Holographic lithography with thick photoresist," Appl. Phys. Lett. **43**, 873 (1983).

[7] H. C. Guo, D. Nau, A. Radke, X. P. Zhang, J. Stodolka, X. L. Yang, S. G. Tikhodeev, N. A. Gippius, and H. Giessen, "Large-area metallic photonic crystal fabrication with interference lithography and dry etching," Appl. Phys. B **81**, 271-275 (2005).

[8] C. A. Pan, and T. P. Ma, "High-quality transparent conductive indium oxide films prepared by thermal evaporation," Appl. Phys. Lett. **37**, 163-165 (1980).

[9] D. Finlayson, "Vacuum vapour deposition as a high rate coating process for sheet steel," Vaccum **21**, 35-39 (1971).

[10] S. Wolf, and R. N. Tauber, *Silicon processing for the VLSI Era, Vol. 2: process integration*, 2nd Ed., Lattice Press, California (1990).

[11] P. A. Farrar, "Forming submicron integrated-circuit writing from gold, silver, copper and other metals," U.S. Patent US6208016 B1 (2001).

[12] G. M. A. Medina, A. G. González, J. L. Sacedón, and A. I. Oliva, "Understanding the thermal annealing process on metallic thin films," IOP Conf. Ser.: Mater. Sci. Eng. **45,** 012013 (2013).

[13] S. Strobel, C. Kirkendall, J. b. Chang, and K. K. Berggren, "Sub-10 nm structures on silicon by thermal detwetting of platinum," Nanotechnology **21**, 505301 (2010).

[14] F. Ruffino, and M. G. Grimaldi, "Template-confined dewetting of Au and Ag nanoscale films on mica substrate," Appl. Surf. Sci. **270**, 697-706 (2013).

[15] J. Y. Kwon, T. S. Yoon, and K. B. Kim, "Comparison of the agglomeration behavior of Au and Cu films sputter deposited on silicon dioxide," J. Appl. Phys. **93**, 3270-3278 (2003).

[16] A. Sundar, R. A. Hughes, P. Farzinpour, K. D. Gilroy, G. A. Devenyi, J. S. Preston, and S. Neretina, "Manipulation the size distribution of supported gold nanostructures," Appl. Phys. Lett. **100**, 013111 (2012).

[17] A. L. Giermann, and C. V. Thompson, "Solid-state dewetting for ordered arrays of crystallographically oriented metal particles," Appl. Phys. Lett. **86**, 121903 (2005).

[18] L. W. Swanson, and G. A. Schwind, "A review of field electron source use in electron microscopes," Microsc. Microanal. **11**, 864-865 (2005).

[19] "Scanning electron microscopy," http://cmrf.research.uiowa.edu/scanning-electron-microscopy.

[20] J. Goldstein, D. E. Newbury, D. C. Lyman, C. E. Lyman, P. Echlin, E. Lifshin, L. Sawyer, J. R. Michael, *Scanning electron microscopy and X-ray microscopy*, 2nd Ed., Plenum Press, New York (1992).

[21] P. Russell, "Scanning electron microscopy (SEM) and atomic force microscopy (AFM): complementary techniques for high resolution surface investigations," Surf. Mod. Technol. **2001**, 109-118 (2002).

[22] "UV-3600 UV-Vis-NIR Spectrophotometer", http://www.ssi.shimadzu.com/products/product.cfm?product=uv3600.

[23] H. G. Tompkins, W. A. McGahan, *Spectroscopic ellipsometry and reflectometry: a user's guide*, John Wiley & Sons, New York (1999).

[24] B. Johs, J. A. Woollam, C. M. Herzinger, J. Hilfiker, R. Synowicki, and C. L. Bungay, "Overview of variable angle spectroscopic ellipsometry (VASE),

part II: advanced applications", Crit. Rev. Opt. Sci. Technol. **CR72**, 29-58 (1999).

[25] A. Campion and P. Kambhampati, "Surface-enhanced Raman scattering," Chem. Soc. Rev. **27**, 241-250 (1998).

[26] E. L. Ru, and P. Etchegoin, *Principles of surface-enhanced Raman spectroscopy: and related plasmonic effects*, Elsevier, Amsterdam (2009).

[27] D. E. Aspnes, "Local-field effects and effective-medium theory: a microscopic," Am. J. Phys. **50**, 704 (1982).

[28] R. D. Averitt, S. L. Westcott, and N. J. Halas, "Linear optical properties of gold nanoshells," J. Opt. Soc. Am. B **16**, 1824-1832 (1999).

[29] B. T. Draine and P. J. Flatau, "Discrete-dipole approximation for scattering calculations," J. Opt. Soc. Am. A **11**, 1491-1499 (1994).

# Chapter 4 Tuning Localized Surface Plasmon Resonances for Plasmonic Sensing: from Nanodots to Nanodot Array

This chapter will present a scalable, rapid and inexpensive method based on laser interference lithography (LIL) and thermal annealing for the fabrication of disordered and quasi-ordered metallic nanodots on glass substrates with tunable localized surface plasmon resonances (LSPR). These nanostructures give the ability to detect the variation of the refractive index change from the surrounding media and to enhance the Raman intensity of the molecules R6G. It is found that the sub-50 nm quasi-ordered nanodot array can provide better refractive index sensitivity than disorder nanodots. In addition, the tunable LSPR is achieved by controlling the Au concentration in Ag/Au nanodots, resulting in the enhancement of the Raman intensity of the molecules R6G due to the optimal coupling between localized plasmon and the incident laser beam.

In Section 4.1, localized surface plasmon resonances induced by metallic nanoparticles and their potentials to deliver plasmonic sensing applications are introduced. In Section 4.2, we employ a simple and inexpensive approach to fabricate large-scale metallic nanoparticles arranged in disordered and quasi-ordered arrays on glass substrates, which gives the capabilities to tune the localized LSPR by varying the Au concentration of Ag/Au bimetallic nanoparticles. In Section 4.3, the fabricated nanodots are applied for plasmonic sensing, involving the refractive index (RI) sensing and the surface

enhanced Raman spectroscopy (SERS). At the end of this chapter in Section 4.4, the conclusions of this work will be summarized.

## 4.1. Introduction

Plasmonics has recently been the subject of intense research efforts due to its unique ability to concentrate the incident light into metallic structures [1]. It has been shown that coherent free-electron oscillations driven by the incident electric field can form two types of oscillations [2]: surface plasmon resonances (SPR) and localized surface plasmon resonances (LSPR). Plasmonic sensing [3] based on LSPR has attracted much research attention arising from its promising advantages, such as being label-free, simple, cost-effective and suitable for measuring the local refractive index change. Plasmonic sensing applied to surface-enhanced spectroscopy [4] has also been studied recently because the resonant excitation of plasmons in metallic nanostructures can provide large field enhancements on the surface of metals, which in turn can provide dramatic increase in the detected spectroscopic signals from molecules absorbed on their surfaces [5]. A recent report has presented that the large field enhancements in plasmonics can form the ultrasensitive infrared spectrum and enable the detection of vibrational signatures of proteins [6]. Furthermore, in the field of plasmonic sensing, it is prudent to employ a simple and high-throughput approach to implement plasmonic nanostructures, which gives the potentials to transfer the technology from laboratory to the real fabrication in industry.

Over the last few decades, attempts to generate plasmonic nanostructures are focused on bottom-up and top-down nanofabrication techniques [7]. In

general, bottom-up nanofabrication provides unique biomolecular control, biomimetic behavior and the potential to create the material with sophisticated properties, but this work is limited to the inherent macroscopic disorder. This disorder could lead to the generation of complex metallic nanostructures, which brings with the difficulties in understanding and modeling the fundamental physics. Alternatively, top-down nanopatterning is a good candidate to avoid this issue [8]. The top-down nanofabrication method offers versatility, miniaturization, precision, reproducibility and batch fabrication capabilities, and has been applied to the semiconductor industry over a few decades. Laser interference lithography (LIL) [9] is a promising top-down nanofabrication technique that serves as a large-area, maskless and noncontact nanopatterning method, which can be used to pattern periodic nanolines and nanodisks on metallic thin films in a short time (only a few minutes exposure), but the dimension of the nanostructures is of the sub-micrometer scale. In addition, we also note that the thermal annealing of continuous metallic thin films can act as a simple approach to pattern large-area metallic nanostructures at a particle size down to sub-50 nm [10]. Such small feature size can let the plasmon resonance be positioned in the UV-visible range, providing an opportunity to detect the configuration of the molecules based on color observation [11]. But the challenging issue of this technique is that the formed metallic nanoparticles have a disordered distribution in size and interparticle distance, which may affect the properties and quality of the resonant features due to the important influence determined by size and interparticle distance in the excitation of LSPR [12]. If LIL is combined with thermal annealing, the uniformity of nanoparticles can be significantly improved. This idea will be

realized in this chapter.

Tuning the localized surface plasmon resonance of metallic nanoparticles remains a challenging issue in surface enhanced spectroscopy [13]. The Raman intensity of the bio/chemical molecules can be enhanced if the plasmon resonance of metallic nanoparticles matches the excitation of the incoming light and overlaps the absorption of the vibration of the interested band [14]. Therefore, this critical condition drives a strong desire to investigate the strategy of tuning the localized surface plasmon resonances over a broad band. In this chapter, we focus on innovation of a scalable, rapid and inexpensive method based on laser interference lithography (LIL) and thermal annealing to pattern metallic nanodots on glass substrates with tunable LSPR in UV-Visible range. These nanostructures give the ability to detect the variation of the refractive index change from the surrounding media and to enhance the Raman intensity of the molecules R6G.

## 4.2. Experimental details

### 4.2.1. Fabrication and characterization of bimetallic Ag/Au nanodots formed by thermal annealing

Thermal annealing of 200 nm-thickness Au thin films has been reported recently, demonstrating the potential to modify the surface and to control well the grain size between 100 and 160 nm [15]. Another report proposed the annealing of Au thin film sputtered on glass substrate and emphasized the important role played by the thickness of the Au film; however this work only focused on the morphology study of the annealed film [16]. We also note that

the average size of Au nanostructures becomes bigger when the thickness of the Au film is increased. It is also observed that the absorption coefficients of Au nanostructures are slightly varied accompanying a gradual increase of the thickness of Au film [17]. Considering the difference in the dielectric constants between Ag and Au, tuning LSPR could be achieved by changing the Au concentration of bimetallic Ag/Au nanostructures, resulting in the spectrum tunabilities in UV-visible range. This idea will be demonstrated bellow.

#### 4.2.1.1. Fabrication procedures

Quartz substrates are firstly cleaned in an ultrasound bath with acetone and isopropyl alcohol solution for 30 min each and finally rinsed with DI water. The cleaned glass slides are dried in an oven prior to metal deposition. The bimetallic Ag/Au metal films are deposited using an electron beam evaporator at a deposition rate of 0.02 nm/sec. In the film deposition, the total thickness remains at 8 nm. The variation of Au concentration is achieved by tuning the thickness of the Au thin film during the film coating process. The deposited samples are put inside a furnace for annealing at 500 ℃. The annealing process is divided into three steps: (1) during the initial stage, the temperature is set to gradually increase from room temperature to the target temperature at a rate 25 ℃/min, (2) constant heating at the target temperature for 1 hr., and (3) cooling for 8 hrs. from the target temperature to room temperature.

When metal thin films deposited on the substrates are annealed at high temperatures, it leads to the formation of the agglomeration of the nanoparticles. It arises from the relaxation of the thermal stress during the

annealing process, accounting for the metal and the substrate having different thermal expansion coefficients [18]. Figure 4.1 shows the morphology of Ag/Au nanoparticles on quartz substrate formed by the annealing of Ag/Au bimetallic thin films of a thicknesses of 4/4 nm and at annealing temperature of 500 ℃ for 1 hr.. It is clearly observed that nanoparticles with round shape are randomly distributed on the substrate. While the diameter of particle size plays an important role in the optical properties of noble nanoparticles. Thus the effective diameters of the annealed nanoparticles are measured using ImageJ [19]. The SEM image of Ag/Au nanoparticles is analyzed and the corresponding size distribution is shown in the inset in the bottom-left side of Fig. 4.1. It is shown that the average size of nanoparticle is below 50 nm.

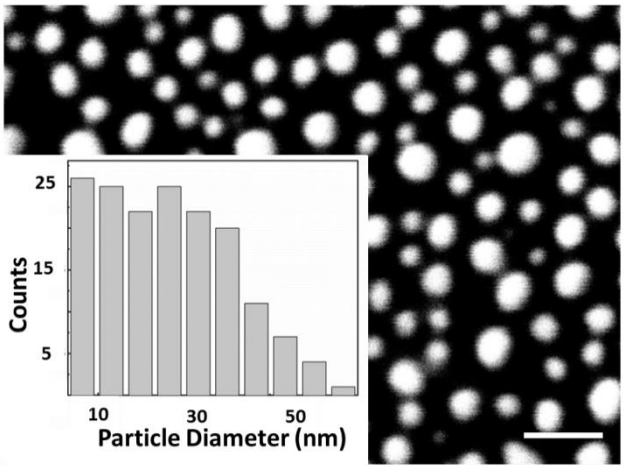


Figure 4.1 SEM image of Ag/Au nanoparticles on quartz substrate formed by the thermal annealing of Ag/Au thin films of thickness of 4 and 4 nm. The scale bar is 100 nm. Size distribution of Ag/Au nanodots is shown in the inset in the bottom-left of the figure.

#### 4.2.1.2. Optical characterization of Ag/Au nanoparticles with different Au concentrations

To realize the plasmonic nanoparticles over a large area, thermal annealing has been confirmed to be a cheap and simple method to generate metallic nanoparticles on the substrate with a spherical shape. A recent article proposed the use of thermal annealing to form gold nanoparticles so as to excite the localized plasmon resonance [19]. However, in this work, the resonance wavelength of Au nanoparticles is tuned from 542 to 558 nm by controlling the thickness of the Au film before thermal annealing, which provides only a limited range to tune the resonance. To overcome this shortcoming, we propose to tune the LSPR of nanoparticles by precisely controlling the Au concentration in Ag/Au nanodots, which can be achieved by controlling the thickness of the Au film during coating of Ag/Au bimetallic films.

Figure 4.2 (a) displays the measured transmission spectra of the annealed bimetallic Ag/Au films with various thicknesses of the Au film and the inset shows a SEM image of the Ag/Au nanoparticles generated by the annealing of Ag/Au (4/4 nm) film. The transmission spectra are normalized in order to focus on the spectral shift. LSPR resonance corresponds to a transmission dip in the spectra. The series of LSPR with different Au concentrations indicate that the dielectric constant of the nanostructures is changed. The spectral shift is plotted in Fig. 4.2 (b) with a linear fitting. It reveals that tuning LSPR can be easily achieved by varying the Au concentration of the nanoparticles. This result demonstrates that LSPR can be tuned over a wide range with a simple approach, without using a complex design of nanostructures.

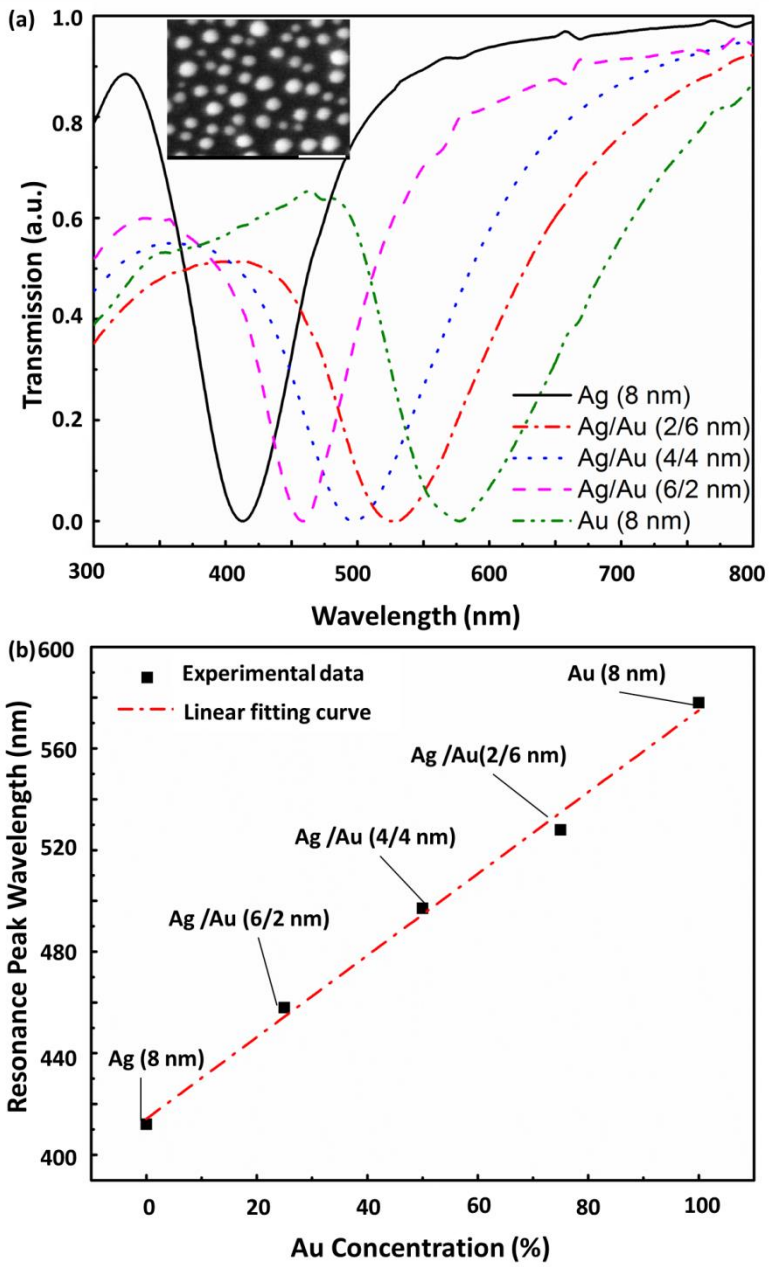


Figure 4.2 (a) Measured transmission spectra of bimetallic Ag/Au nanoparticles with different Au concentrations. (b) Resonance wavelength shift as a function of Au concentration. The SEM image of Ag/Au nanoparticles patterned by annealing the bimetallic Ag/Au thin film with the thicknesses of 4 and 4 nm is inserted in the top-left of the plot (a) with the scale bar of 100 nm.

### 4.2.2. Fabrication and characterization of quasi-ordered bimetallic Ag/Au nanodot array by LIL and thermal annealing

Thermal annealing provides a good way of forming nanodots with diameter of sub-50 nm (Fig. 4.1), but size dimension and particle distribution of nanodots are randomized on the substrate. In particular, it has been reported that the random nanoparticles with constant size can lead to a broad resonant quality and more plasmon loss due to the destructive interactions between nanoparticles [20]. In addition, it was also pointed out that the random size distribution leads to even broader resonant features. Therefore, we propose a hybrid nanofabrication technique to form quasi-ordered nanodot array with a good uniformity over a large area. This method is the combination of LIL and thermal annealing, which can reduce the randomness of the nanodots in both terms of size distribution and particle location. By properly controlling Au concentration, the LSPR of bimetallic nanodot array can be tuned.

#### 4.2.2.1 Fabrication procedures

Nanodot array was fabricated by the combination of LIL and thermal annealing. LIL can form a periodic nanodisk array over a large area, which can be used to form a good template for thermal annealing. Compared to the annealing of a whole thin film, the annealing of nanodisk array is easier to achieve nanodot array with better uniformity both in terms of size dimension and particle distribution. Therefore, the fabrication consists of two main steps: (1) fabricating a periodic array of nanodisk by LIL and then (2) annealing the nanodisk array at high temperatures.

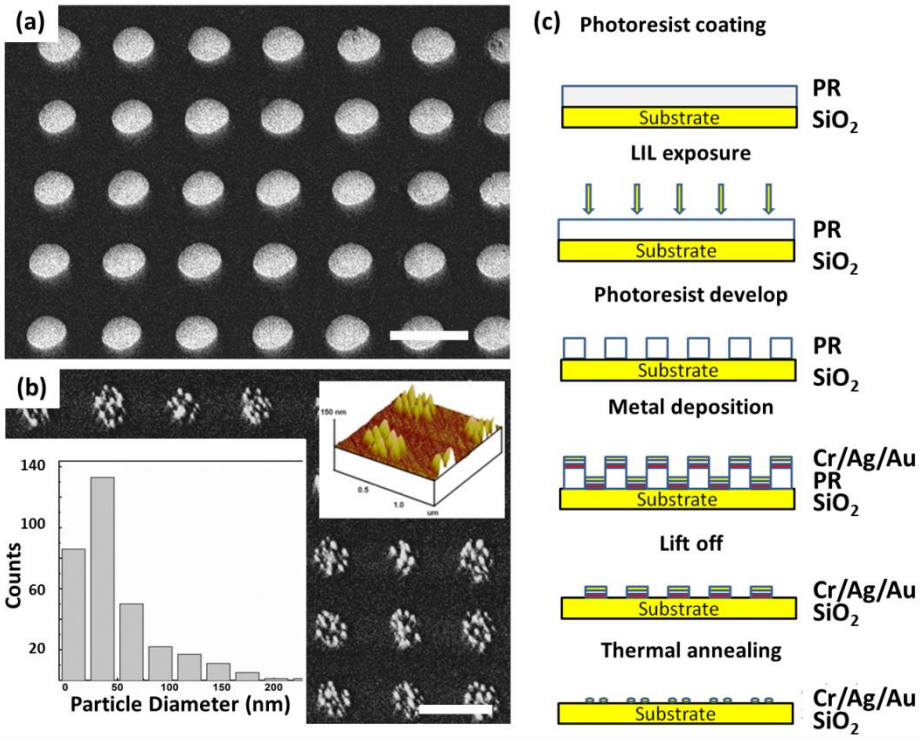


Figure 4.3 SEM images of $Ag_{0.75}/Au_{0.25}$ nanodisk array (a) before and (b) after annealing. AFM image of Ag/Au nanodot array is inserted in the top-right of the plot (b). (c) Schematic diagram of the corresponding fabrication process.

Figure 4.3 displays the SEM image of a bimetallic nanodot array formed by LIL and thermal annealing. The bimetallic $Ag_{0.75}/Au_{0.25}$ nanodisk array was formed by the double exposure of LIL at an incident angle ($\theta$) of 10 °. The Ag and Au films were deposited in sequence with thicknesses of 6 and 2 nm, respectively. After lift-off, the Ag/Au nanodisk array was annealed at a temperature of 500 ℃ for 4 hrs.. The term $Ag_{1-x}/Au_x$ indicates that the Au concentration ($x$), which is controlled during the metal films deposition. Before thermal annealing ( as shown in Fig. 4.3 (a)), it is observed that the bimetallic $Ag_{0.75}/Au_{0.25}$ nanodisk array with a diameter of 538 ± 18 nm was formed with a period of ~ 930 nm on the quartz substrate. The structure exhibits a good uniformity of nanodots over an area of 8 × 8 $mm^2$. During thermal annealing at 500 ℃ for 4 hrs., the $Ag_{0.75}/Au_{0.25}$ bimetallic nanodisk

array was heated above the melting temperature, so the originally continuous bimetallic thin films broke up into isolated nanodots. The nanodots were agglomerated due to a high surface-to-volume ratio [21]. The SEM image of the nanodot array was analyzed by the software ImageJ, which indicates that the nanodots have a spheroidal shape, with size dimension of $50 \pm 30$ nm, interparticle spacing of $45 \pm 15$ nm. The height of the nanodisk increases from $8 \pm 2$ nm to $45 \pm 15$ nm, which was shown by the AFM image of the nanodot array in Fig. 4.3 (b). The results confirm that the combination of LIL and thermal annealing is a straightforward method to form nanodot array with a good uniformity both in terms of size dimension and particle distribution.

#### 4.2.2.2. Characterization procedures

The optical properties of the $Ag_{0.75}/Au_{0.25}$ and $Ag_{0.25}/Au_{0.75}$ nanodot array fabricated by the combination of LIL and thermal annealing were measured in the transmission mode, as shown in Fig. 4.4. The $Ag_{0.75}/Au_{0.25}$ (black solid line) and $Ag_{0.25}/Au_{0.75}$ (red solid line) nanodots were formed by LIL and thermal annealing of bimetallic Ag/Au nanodisk array with thicknesses of 6/2 nm and 2/6 nm, respectively. The transmission spectrum (black dashed line) of Ag/Au nanodots was also plotted in Fig. 4.4 as the reference. These nanodots were only processed by the thermal annealing of bimetallic Ag/Au thin films with thicknesses of 2/6 nm.

As seen in Fig. 4.4, only one transmission dip is observed in the UV-visible range for each measured spectrum, which corresponds to the excitation of LSPR induced by the bimetallic nanostructures. It is found that the plasmon resonance of $Ag_{0.25}/Au_{0.75}$ nanodot array and Ag/Au nanodots are located at

518 nm and 529 nm with the linewidths of 174 and 182 nm, respectively, as analyzed using a Lorentzian function. The difference in the plasmon wavelength and linewidth is ascribed to the degree of the randomness in both sizes and particle distribution. This fact was been confirmed by the study of surface plasmon resonance in periodic and random patterns of gold nanodisks previously, demonstrating that the randomness can reduce the electric field enhancement so as to make broader spectra [20]. Our SEM images of nanodot array and nanodots also support this conclusion, showing the uniformity in their sizes and particle distributions. It is also clearly observed that the resonance wavelength of Ag/Au nanodot array shifts towards a longer wavelength with an increase of Au concentration in the bimetallic nanostructures, which is attributed to the difference in the complex dielectric functions of the two metals [22]. For the same size dimension, LSPR of Ag nanodisk is normally located in a shorter wavelength than that of the Au nanodisk, supporting that LSPR of nanodots with a higher Au concentration is located at a longer wavelength than that of a lower Au concentration.

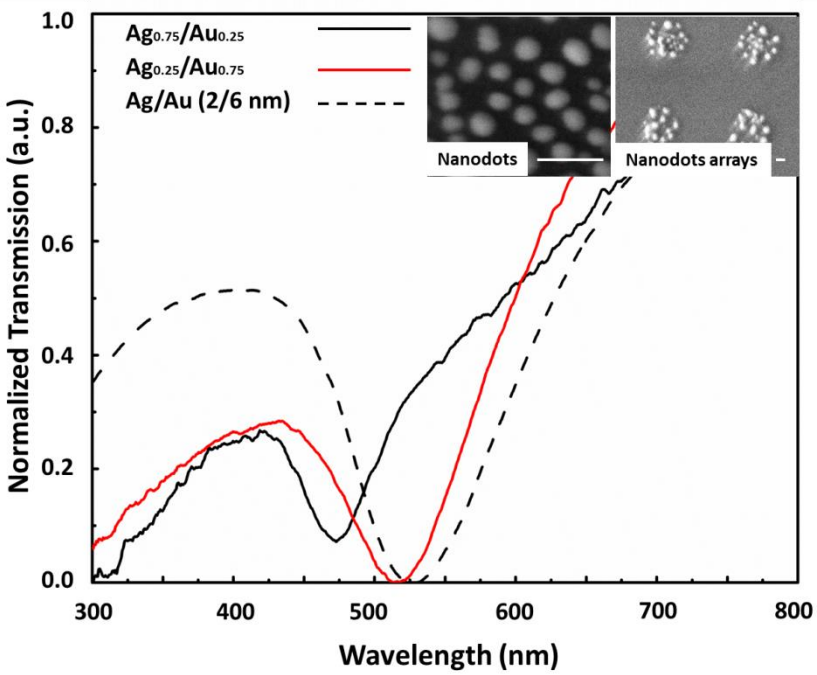


Figure 4.4 Measured transmission spectra of bimetallic $Ag_{0.75}/Au_{0.25}$ and $Ag_{0.25}/Au_{0.75}$ nanodot array (black and red solid lines) formed by LIL and thermal annealing, as well as $Ag_{0.25}/Au_{0.75}$ (black dashed line) formed only by thermal annealing. The corresponding SEM images of $Ag_{0.25}/Au_{0.75}$ nanodots and $Ag_{0.25}/Au_{0.75}$ nanodot array are inserted in the top-right of the figure.

### 4.3. Localized surface plasmon sensing and spectroscopy

Localized surface plasmon resonances of noble metal nanostructures have been shown be a powerful technique for chemical and biological sensing arising from their capabilities to generate highly intense electromagnetic field on the metal surface. This electromagnetic field enhancement can be used to detect the refractive index (RI) change of the surrounding or also to enhance the Raman intensity of the molecules, which can act as plasmonic RI sensors or surface enhanced Raman spectroscope (SERS). In this section, we offer the feasibility that our fabricated nanostructures can be applied as potential label-free RI sensors and also functionalized substrates to enhance Raman signals of the molecules R6G.

### 4.3.1. Refractive index sensing for bimetallic nanodots and nanodot array

To evaluate the sensing performance of the $Ag_{0.75}/Au_{0.25}$ nanodot array on quartz substrates, extinction spectra at different environments are plotted in Fig. 4.5 (a). It is observed that the LSPR peak positions in methanol and ethanol are red-shifted from 508 (air), 529 (methanol) to 532 nm (ethanol) due to an increase in the refractive index of the surroundings from 1.0000, 1.3290 to 1.3614 [23]. The plasmon spectral shifts of the nanodot array are ascribed to the variation in the dielectric constants induced by the environment. In particular, the sensitivity of the nanostructures are experimentally determined by the slope of a linear fit in the plot of LSPR peak wavelength versus the refractive index as shown in Fig. 4.5 (b). The $Ag_{0.75}/Au_{0.25}$ nanodots are formed by the thermal annealing of Ag/Au bimetallic thin films with the thicknesses of 6/2 nm at 500 °C for 4 hrs.. The LSPR peak shift per refractive index of the $Ag_{0.75}/Au_{0.25}$ nanodot array is calculated as 64 nm/RIU, which is 94% higher than the nanodots formed by only thermal annealing. It shows that the nanostructures fabricated by the combination of LIL and thermal annealing can improve the performance of LSPR sensing.

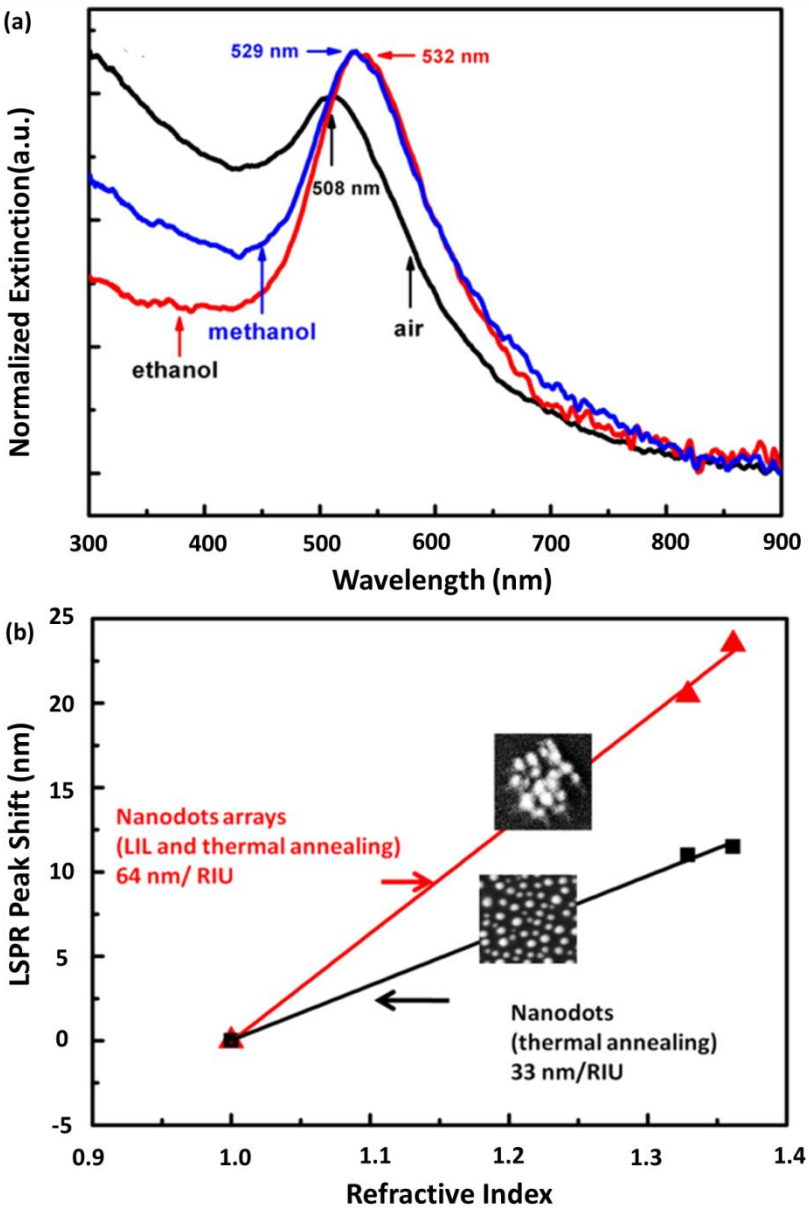


Figure 4.5 (a) Measured extinction spectra of the $Ag_{0.75}/Au_{0.25}$ nanodot array in the environments with different refractive indices (air, methanol and ethanol) and (b) the spectral shift of $Ag_{0.75}/Au_{0.25}$ nanodot array as a function of the refractive index. The refractive indices of air, methanol, and ethanol are 1.0000, 1.3290, and 1.3614, respectively.

### 4.3.2. Surface enhanced Raman spectroscopy using bimetallic nanodot array with tunable LSPR

Raman spectroscopy is a powerful analytical tool which can identify

fingerprints of the molecules, but their intensities are very weak due to an inefficient inelastical scattering [5]. It has been found that the Raman intensity can be improved by the excitation of LSPR from metallic nanostructures [14]. However, there is a critical excitation condition for LSPR to enhance the Raman signals: only when the LSPR wavelength of metallic nanostructures matches well with the excitation wavelength of the laser and also overlaps with an electronic absorption band of interest [24]. Therefore, tuning LSPR resonance wavelength of SERS substrates in a specific range is of importance to improve the Raman intensity of the molecules.

Here we report a simple and efficient approach to flexibly tune the LSPR of quasi-ordered hybrid nanostructures over a large area. This approach is applied to optimize Raman scattering intensity of the molecule R6G. Ag/Au nanodot array was fabricated by LIL and thermal annealing of 12 nm bimetallic Ag/Au thin films [25]. Tuning of LSPR was accomplished by controlling the thicknesses of the Ag/Au film in the configuration of bimetallic nanodisks, arising from the variation of permittivity in nanodots. This is confirmed in Fig 4.6 (a) where the LSPR of $Ag_{0.75}/Au_{0.25}$ is located at a shorter wavelength than that of $Ag_{0.5}/Au_{0.5,}$ which is attributed to more Au materials in the $Ag_{0.5}/Au_{0.5}$ nanodot array. $Ag_{0.75}/Au_{0.25}$ means that the bimetallic nanodisk arrays fabricated by LIL before the thermal annealing consists of 9 nm thick Ag and 3 nm thick Au thin films, respectively.

Figure 4.6 (b) shows the SERS spectra of the molecule R6G ($10^{-4}$ mol/L) coated on the pure glass substrate, $Ag_{0.75}/Au_{0.25}$ and $Ag_{0.5}/Au_{0.5}$ nanodot array, respectively. The SERS spectra were measured at an excitation wavelength of 514 nm under a 50X objective lens. Firstly, we note that the Raman intensity

of the molecule R6G coated on both Ag/Au nanodot array increases significantly, especially at the 1657 $cm^{-1}$ band, compared to that on the pure glass substrate. Ag/Au nanodot array can act as hot spots to concentrate the incident electric field into these small volumes where the field becomes very intense, resulting in the Raman intensity scaling with the fourth power of the local field at the metal surface [26]. Secondly, the Raman intensity at the 1657 $cm^{-1}$ band on $Ag_{0.5}/Au_{0.5}$ nanodot array has been enhanced by two times as compared to that on $Ag_{0.75}/Au_{0.25}$ nanodot array. This is because the relaxation and re-emission of Raman scattered radiation of the molecules can be modified and even enhanced by the local electric field [5]. When the LSPR wavelength position of the metallic nanostructures is tuned to match well with the excitation wavelength of the laser beam and also to overlap with the Raman wavelength of the interested band, the Raman intensity of the molecules can be further enhanced [27]. Our results agree well with this conclusion because the LSPR wavelength of $Ag_{0.5}/Au_{0.5}$ nanodot array is located at 539 nm, which is in the range between the excitation wavelength ($\lambda_{ext}$ = 514 nm) and the wavelength that Raman-scattered by the R6G ($\lambda_{vib}$ = 745 nm) at the 1657 $cm^{-1}$ band. The wavelength of the Raman scattered photon ($\lambda_{vib}$) at the 1657 $cm^{-1}$ band is calculated by the formula, $\Delta\omega = 1/\lambda_{ext} - 1/\lambda_{vib}$, where the excitation wavelength $\lambda_{ext}$ and the Raman shift $\Delta\omega$ are 514 nm and 1657 $cm^{-1}$, respectively. In contrast, a weaker Raman intensity on $Ag_{0.75}/Au_{0.25}$ nanodot array is noted. Therefore, the Raman intensity of the molecules R6G can be optimized by using a tunable Ag/Au nanodot array.

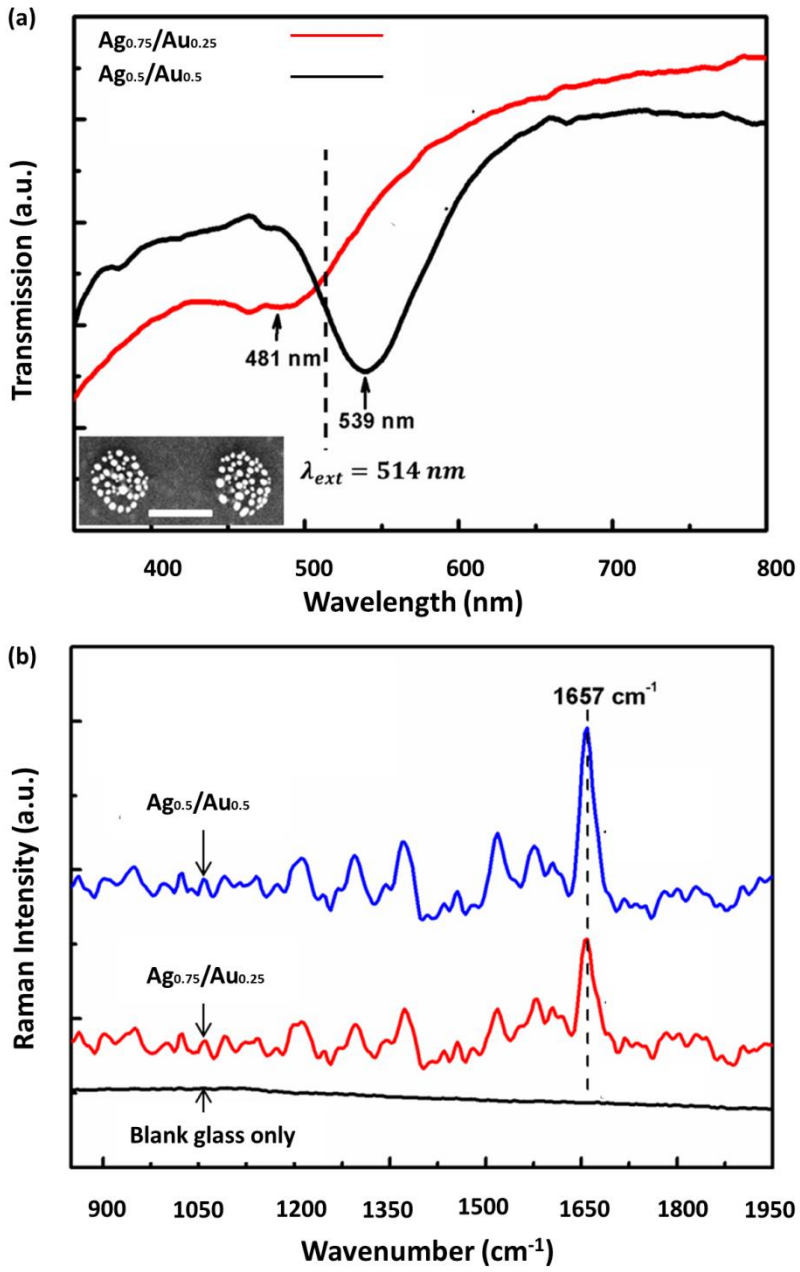


Figure 4.6 (a) Measured UV-Vis spectra of $Ag_{0.75}/Au_{0.25}$ (red solid line) and $Ag_{0.5}/Au_{0.5}$ (black solid line) nanodot array formed by the thermal annealing of Ag/Au nanodisk array with the thicknesses of 9/3 and 6/6 nm, respectively. (b) Measured Raman spectra of glass substrate only (black solid line) $Ag_{0.75}/Au_{0.25}$ (red solid line) and $Ag_{0.5}/Au_{0.5}$ (blue solid line) nanodot array covered by the molecules R6G. SEM image of $Ag_{0.5}/Au_{0.5}$ nanodot array is inserted in the bottom-left of the plot (a) with the scale bar of 500 nm.

## 4.4. Summary

To sum up, a scalable, rapid and inexpensive approach based on laser interference lithography (LIL) and thermal annealing has been demonstrated to fabricate the disordered and quasi-ordered metallic nanodots on glass substrates with tunable localized surface plasmon resonances (LSPR). These nanostructures give the abilities to detect the variation of the refractive index change from the surrounding media and also enhance the Raman intensity of the molecules R6G. It is found that the sub-50 nm quasi-ordered nanodot array can provide better refractive index sensitivity than disordered nanodots. In addition, tunable LSPR is achieved by controlling the Au concentration in Ag/Au nanodots, thus allowing us to further enhance the Raman intensity of R6G due to the optimal coupling between localized plasmon and the incident laser.

## 4.5. References

[1] D. Gramotnev and S. Bozhevolnyi, “Plasmonics beyond the diffraction limit,” Nat. Photon. **4**, 83-91 (2010).

[2] S. A. Maier and H. A. Atwater, “Plasmonics: localization and grating of electromagnetic energy in metal/dielectric structures,” J. App. Phys. **98**, 011101-1-011101-10 (2005).

[3] A. J. Haes and R. P. Van Duyne, “A nanoscale optical biosensor: sensitivity and selectivity of an approach based on the localized surface plasmon resonance spectroscopy of triangular silver nanoparticles,” J. Am. Chem. Soc. **124**, 10596-10604 (2002).

[4] K. A. Willets, and R. P. Van Duyne, “Localized surface plasmon resonance spectroscopy and sensing,” Annu. Rev. Phys. Chem. **58**, 267-297 (2007).

[5] H. Wei, F. Hao, Y. Z. Huang, W. Z. Wang, P. Nordlander, and H. X. Xu, “Polarization dependence of surface-enhanced Raman scattering in gold nanoparticle-nanowire systems,” Nano Lett. **8**, 2497-2502 (2008).

[6] N. C. Lindquist, P. Nagpal, K. M. McPeak, D. J. Norris and S. H. Oh, “Engineering metallic nanostructures for plasmonics and nanophotonics,” Rep. Prog. Phys. **75**, 036501 (2012).

[7] G. A. Ozin, K. Hou, B. V. Lotsch, L. Cademartiri, D. P. Puzzon, F. Scotognella, A. Ghadimi, J. Thomson, “Nanofabrication by self-assembly,” Mater. Today **12**, 12-23 (2009).

[8] D. Mijatovic, J. C. T. Eijkel, and A. V. den Berg, “Technologies for nanofluidic systems: top-down vs. bottom-up – a review,” Lab Chip **5**, 492-500 (2005).

[9] C. H. Liu, M. H. Hong, H. W. Cheung, F. Zhang, Z. Q. Huang, L. S. Tan, and T. S. A. Hor, “Bimetallic structure fabricated by laser interference lithography for tuning surface plasmon resonance,” Opt. Express **16**, 10701-10709 (2008).

[10] S. Strobel, C. Kirkendall, J. B. Chang, and K. K. Berggren, “Sub-10 nm structures on silicon by thermal detwetting of platinum,” Nanotechnology **21**, 505301 (2010).

[11] M. Khorasaninejad, N. Abedzadeh, J. Walia, S. Patchett, and S. S. Saini, “Color matrix refractive index sensors using coupled vertical silicon nanowire arrays,” Nano Lett. **12**, 4228-4234 (2012).

[12] E. J. Smythe, E. Cubukcu, and F. Capasson, “Optical properties of surface plasmon resonances of coupled metallic nanorods,” Opt. Express **15**, 7439-7447 (2007).

[13] J. Yao, A. P. Le, S. K. Gray, J. S. Moore, J. A. Rogers, and R. C. Nuzzon, “Functional nanostructured plasmonic materials,” Adv. Mater. **22**, 1102-1110 (2010).

[14] A. D. McFarland, M. A. Young, J. A. Dieringer, and R. P. Van Duyne, “Wavelength-scanned surface-enhanced Raman excitation spectroscopy,” J. Phys. Chem. B **109**, 11279-11285 (2005).

[15] G. M. Alonzo-Medina, A. Gonzalez-Gonzalez, J. L. Sacedon and A. I. Oliva, “Understanding the thermal annealing process on metallic thin films,” IOP Conf. Series: Mater. Sci. Eng. **45**, 012013 (2012).

[16] V. Svorcik, J. Siegel, P. Sutta, J. Mistrik, P. Janicek, P. Worsch, Z. Kolska, “Annealing of gold nanostructures sputtered on glass substrate,” Appl. Phys. A **102**, 605-610 (2011).

[17] V. Svorcik, O. Kvitek, O. Lyutakov, J. Siegel, Z. Kolska, “Annealing of sputtered gold nanostructures,” Appl. Phys. A. **102**, 747-751 (2011).

[18] A. Serran, O. Rodriguez de la Fuente, and M. A. Garcia, “Extended and localized surface plasmons in annealed Au films on glass substrates,” J. Appl. Phys. **108**, 074303 (2010).

[19] M. D. Abramoff, P. J. Magelhaes, S. J. Ram, “Image processing with ImageJ,” Biophotonics Int. **11**, 36-42 (2004).

[20] Y. Nishijima, L. Rosa, and S. Juodkazis, “Surface plasmon resonances in periodic and random patterns of gold nano-disks for broadband light harvesting,” Opt. Express **20**, 11466-11477 (2012).

[21] H. Krishna, N. Shirato, S. Yadavali, R. Sachan, J. Strader and R. Kalyanaraman, "Self-Organization of Nanoscale Multilayer Liquid Metal Films: Experiment and Theory", ACS Nano **5**, 470-476 (2010).

[22] N. P. Hylton, X. F. Li, V. Giannini, K. H. Lee, N. J. Ekins-Daukes, J. Loo, D. Vercruysse, P. Van Dorpe, H. Sodabanlu, M. Sugiyama, and S. A. Maier, "Loss mitigation in plasmonic solar cells: aluminum nanoparticles for broadband photocurrent enhancements in GaAs photodiodes," Sci. Rep. **3**, 2784 (2013).

[23] D. R. Lide, "Handbook of Chemistry and physics", 87$^{th}$ ed., CRC Press, Florida (2006).

[24] N. Félidj, J. ubard, and G. Lévi, "Optimized surface-enhanced Raman scattering on gold nanoparticle arrays," App. Phys. Lett. **82**, 3095-3097 (2003).

[25] L. Xu, L. S. Tan, and M. H. Hong, "Tuning of localized surface plasmon resonance of well-ordered Ag/Au bimetallic nanodot arrays by laser interference lithography and thermal annealing," App. Opt. **50**, G74-G79 (2011).

[26] M. Moskovits, "Surface-enhanced Raman spectroscopy: a brief retrospective," J. Raman Spectrosc. **36**, 485-496 (2005).

[27] Jon A. Dieringer, Kristin L. Wustholz, David J. Masiello, and Jon P. Camden, "Surface-enhanced Raman excitation spectroscopy of single Rhodamine 6G molecule," J. Am. Chem. Soc. **131**, 849-854 (2008).

# Chapter 5 High Performance Refractive Index Sensing through the Surface Lattice Resonance of Nanorod Array

In this chapter, a new approach to improve refractive index (RI) sensing will be investigated theoretically and experimentally. By illuminating periodic array of nanorods with the incident light polarized along the long axis of the nanorods, collective diffractive interaction between dipolar resonances of the individual nanorods can be observed, known as the surface lattice resonance (SLR). Dramatic improvement in the narrowing of the far-field extinction spectra and near-field enhancement can be achieved, arising from the partial cancellation in the radiative damping of the dipoles.

In Section 5.1, an introduction on different approaches of improving RI sensitivity will be presented, followed by an explanation of new design on high performance RI sensing through a periodic array of nanorods. The detailed resonant features will be investigated using FDTD simulation, and RI sensitivity based on these resonant modes will be evaluated in Section 5.2. In Section 5.3, the fabrication and characterization procedures of the designed nanorod array will be presented. In Section 5.4, the physics behind SLR mode and RI sensing performance of the fabricated nanosensors will be described. At the end of this chapter in Section 5.5, the conclusions of this work will be summarized.

## 5.1. Introduction

Plasmonic sensing has been successfully applied to detect bio/chemical molecule-binding events in molecular conformation [1]. In general, two types of plasmonic nanosensors have been widely discovered: (1) Surface Plasmon Resonances (SPR) at metal-dielectric interfaces and (2) Localized Surface Plasmon Resonances (LSPR) on nanostructured noble-metal surfaces [1-2]. SPR sensors have been shown to have an extremely low detection limit exceeding $10^{-5}$ refractive-index unit (RIU) using phase-sensitive interferometry schemes [3], but they are difficult to be integrated into portable and low-cost devices for high throughput systems [4]. LSPR sensors, on the other hand, have drawn immense research interests due to their nanoscale-level dimensions, spectra tunability [5] and strong enhancements of the local electrical fields [6]. However, the drawbacks of LSPR based sensors are low sensitivities and broad resonance features, which are still challenging issues until now [2].

Improvements in LSPR sensing performance can be achieved by increasing light-matter interactions through high field enhancement on sharp nanoparticle vertices or closely spaced nanoparticle assemblies. The strong field confinements make the nanoparticles more sensitive to the changes in their dielectric environment [7-9]. For example, by increasing the aspect ratio (length/width) or sharpening nanoparticle features, it has been shown that RI sensitivities based on LSPR sensor is improved up to 288 nm/RIU for gold nanorods with aspect ratio of 2.4, and 540 nm/RIU for gold nanobipyramids possessing sharp edges at the ends and high aspect ratio reaching to 4.7 [7].

However, while chemical synthesis has the advantage of precisely controlling the dimensions of the nanoparticles, which their plasmon resonances usually display broad features in the spectra, resulting in low detection resolution. To solve this issue, many efforts have been concentrated on optimizing the nanoparticle geometries to improve near-field enhancements as well as to control the resonance linewidth. One solution is to generate high intensity near-field interactions at “hotspots” by using closely-space nanoparticle arrays [8, 9]. For example, it has been demonstrated that the RI sensitivity of nanoring trimers is nearly three times larger than that of nanodisk trimers at comparable sizes. Alternatively, high resolution sensors can also be achieved using coherent coupling of bright and dark plasmon modes, leading to high quality factor subradiant Fano resonances. This idea was experimentally realized by a complex asymmetric nanocavity, supporting Fano resonances in an XI arrangement with strongly reduced linewidths [9]. However, it is difficult to fabricate nanostructures over a large area using current nanofabrication techniques such as electron beam lithography or focused ion beam, thus rendering high fabrication cost and low throughput [10]. Therefore, it is highly desirable to have a simple method to fabricate large area plasmonic nanostructures with highly concentrated fields. The discovery of the surface lattice resonance (SLR) provides new opportunities to achieve this goal, through the diffractive coupling of LSPR driven by the individual nanoparticles. In other words, this resonance is generated as the consequence of the dipolar-dipolar interactions [11]. These resonances can efficiently suppress the radiative damping associated with the individual nanorod [12], narrowing linewidth to the order of tens of nanometers and resulting in Q-

factors exceeding 150 in the near infrared range [13, 14]. In addition, far-field coupling does not require complex nanostructures with sub-100 nm gaps, but it needs a periodic array of nanostructures to generate the diffraction features. These properties offer a new opportunity to fabricate them by laser interference lithography over a large area, which will be presented below.

## 5.2. Design and simulation for high performance sensing via a periodic array of nanorods

From the previous discussion of different approaches to improve RI sensitivities, it is known that SLR supported by a periodic array of nanostructures is an attractive candidate for high performance RI sensing. It is because this coupling can generate intense electromagnetic fields and narrow spectral shapes, which provides good sensitivity and high resolution for nanosensors [15-20]. Therefore, the fundamentals of SLR will be presented first, followed by the design and simulation of periodic nanostructures to generate SLR. In particular, a direct quantitative numerical simulation using three-dimensional (3D) finite-difference time-domain (FDTD) method is conducted by qualitatively modeling the plasmonic nanostructures. The design of plasmonic nanostructures and the details of the numerical model will be described below.

### 5.2.1. Fundamentals of surface lattice resonances

Based on the previous studies [15-20], surface lattice resonance is the result of collective plasmonics arising from the retarded dipolar interactions

among nanoparticles. Plasmonic behavior of the nanoparticles in an array may strongly differ from that of the individual constituent nanoparticles [8, 9]. This phenomenon can be explained by using a coupled dipole (CD) method. For an individual nanoparticle, the acting field is the simple incident field exciting LSPR ($E_{act} = E_{inc}$). A nanoparticle responds to this electric field with an induced dipole moment $P = \alpha E_{act}$. On the other hand, for an array of nanoparticles, the acting field on the individual particle includes both the incident field and the sum of the retarded dipolar fields due to the other particles [8, 9, 22-24]:

$$E_{act,i} = E_{inc,i} + \sum_{\substack{j=1 \\ j \neq i}}^{N} e^{ikr_{ij}} C_{ij} p_j \,, \qquad \text{(Eq. 5.1)}$$

where $C_{ij}$ is the dipolar interaction matrix without the phase term. The indices $i$ and $j$ label the $i_{th}$ and $j_{th}$ particles, $r_{ij}$ is the distance between them, and $N$ is the total number of particles. The sum in Eq. 5.1 strongly depends on the phase delay experienced by the retarded dipolar interactions among particles. Hence, for a periodically arranged nanoparticle array, the scattered fields add in phase at a specific wavelength when $kr_{ij} = 2\pi m$, where $m$ is an integer, predicting the appearance of a new grating order. For wavelengths shorter/longer than this transition wavelength ($\lambda_g$), the grating order becomes radiative or evanescent. This phenomenon results in the narrowing of the plasmonic resonances and the enhanced near-fields around the transition wavelength. In particular, SLR resonance ($\lambda_{SLR}$) is located at slightly longer than the grating transition wavelength, and has a narrow line shape. The narrowing of the far-field spectra arises from a partial cancellation in a

radiative damping of the individual nanoparticle. In addition, near-field intensity is also increased and confined in the array plane. In well-engineered arrays, significant improvements in near-field intensities are possible [9].

### 5.2.2. Excitation of SLR mode

According to the theoretical analysis of SLR mode, it is known that the excitation of SLR mode is associated with the diffraction provided by the grating and LSPR features induced by the individual nanoparticle. Three factors will be considered in our design: (1) the geometries of nanostructures, (2) lattice shape and (3) lattice period. Moreover, a simple design with the possibility to be reproducibly implemented by our nanofabrication techniques is required. To achieve this target and satisfy both theoretical and experimental requirements, an array of nanorods with a rectangular lattice shape is designed. Firstly, the nanorod for an individual nanostructure is selected because it not only offers less radiative damping than the nanodisk, but also provides larger local-field enhancement factors [7, 26]. Secondly, the rectangle lattice shape is a good candidate and has been also confirmed by the previous study that nanorod array in rectangular shape has successfully supported SLR [10-12]. In addition, in view of the fabrication procedure, LIL is a straightforward fabrication tool to generate periodic nanostructures over a large area. Thirdly, the lattice constant is an important factor to influence the coupling strength of the diffractive interaction between the dipoles. This factor will be discussed in the next chapter. Moreover, light polarization needs to be considered due to the geometric properties of nanorods. Nanorods can provide two LSPR modes: the longitudinal and transversal modes, corresponding to two different axes of

the nanorods [7, 26]. The observations of SLR mode under light polarization along the long or short axis of nanorods were reported in previous studies [10-12]. Therefore, considering the requirements mentioned above and the fabrication techniques we have, we designed a periodic array of nanorods on the glass substrate, with the length ($l$) 520 nm, the width ($w$) 420 nm, and lattice periods ($P_x$ and $P_y$) of 550 and 900 nm in $x$ and $y$ directions, as shown in Fig. 5.1.

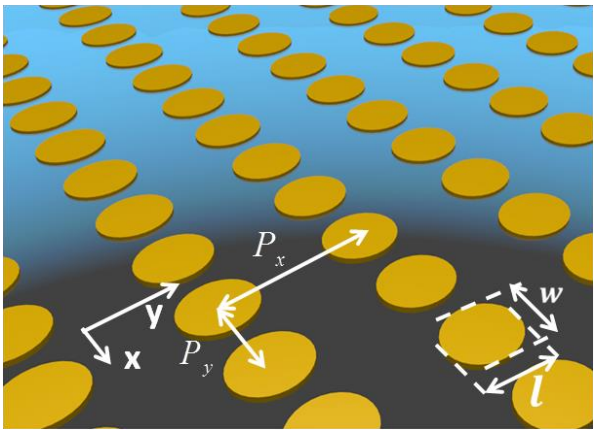


Figure 5.1 Schematic diagram of a periodic array of nanorods on glass substrate. An array of nanorods has length $l$, width $w$, and periods $P_x$ and $P_y$ in $x$ and $y$ directions.

### 5.2.3. Far-field optical properties of nanorod array

A finite-difference time-domain (FDTD solution 7, Lumerical Inc.) optical simulation was performed to study the resonance features of nanorod array. The work is focused on the far-field optical spectra and field profiles of the structures. The setup of three-dimensional (3D) FDTD simulation is shown in Fig. 5.2. The setup includes four main parts: (1) the material structure, (2) the FDTD simulation area, (3) the source, and (4) monitors. Firstly, an elliptical

shaped gold nanorod with a dimension of 420×520×30 $nm^3$ is placed on the top of a glass substrate. The refractive index of the glass substrate is set as 1.45, the dielectric parameters of gold material is based on the experimental data from Johnson and Christy [28]. Secondly, a plane wave source is placed on the top of the simulation area at a distance of 500 nm away from the sample. The light polarization direction and the incident angle can be tuned in the source plane. In our case, we use the normal incident light to illuminate the sample, and the light polarization can be set up parallel along *x* and *y* directions, respectively. Thirdly, the geometry of FDTD simulation is fixed at 550 and 900 nm in *x* and *y* directions, respectively, and it also matches the lattice periods of the designed nanorod array. Periodic boundary conditions are applied in *x* and *y* directions, while perfectly matched layers (PML) boundary is set in *z* direction. A mesh step size to refine the simulation is used with the value of 6 nm for *x* and *y* directions, and 2 nm for z direction. Finally, frequency-domain power monitors are positioned on both the top and the bottom of the nanorod at a distance of 800 nm, respectively. These monitors act as detectors to collect power flow information in the frequency domain from simulation results, and they are also used to calculate transmittance, reflectance and absorption of the structure. The frequency-domain profile monitor is placed in the middle of the nanorod, to collect the field profile in the frequency domain.

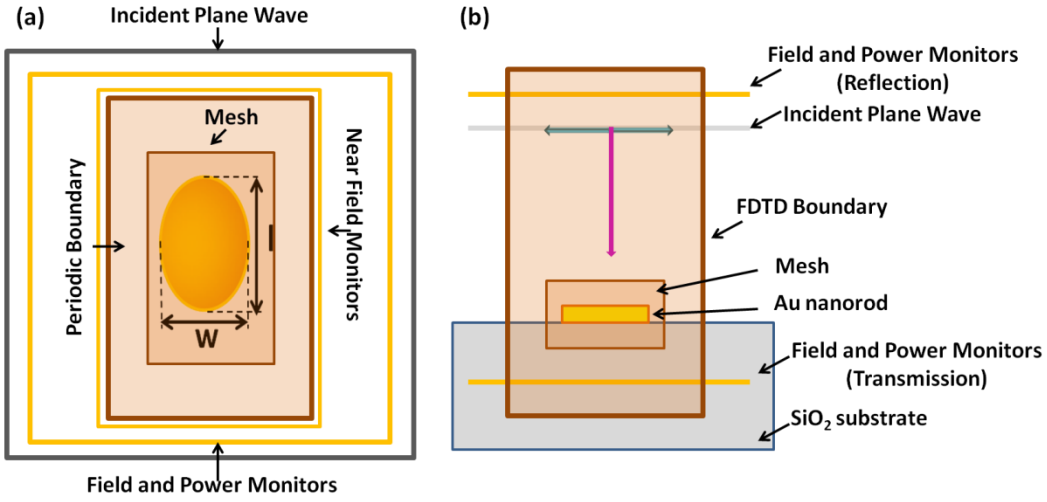


Figure 5.2 Schematic diagrams of FDTD simulation for the optical properties of nanorod array: (a) top and (b) cross-sectional, views.

Figure 5.3 displays the simulated far-field optical responses of nanorod array and a single nanorod in air environment ($n$ = 1) under light illumination along $x$ and $y$ directions. With light polarization along the long axis of the nanorod ($y$ direction), a periodic array of nanorods shows two obvious resonances located at $\lambda_I = 920$ nm and $\lambda_{II} = 1340$ nm, corresponding to a local minimum in transmission and a maximum in reflection (Fig. 5. 3(a)). When the light polarization is along the short axis of the nanorod ($x$ direction), two resonances are also clearly observed at the wavelength positions of 806 and 1333 nm, respectively (Fig. 5.3 (b)). To compare the difference in the optical properties between a single nanorod and an array of nanorods, the extinction spectra of a single nanorod are plotted in a black dashed line (Figs. 5.3 (a) and (b)). The resonances of LSPR for a single nanorod are located at 1676 and 1387 nm, respectively, which are responsible for the longitudinal and transversal modes induced by the single nanorod.

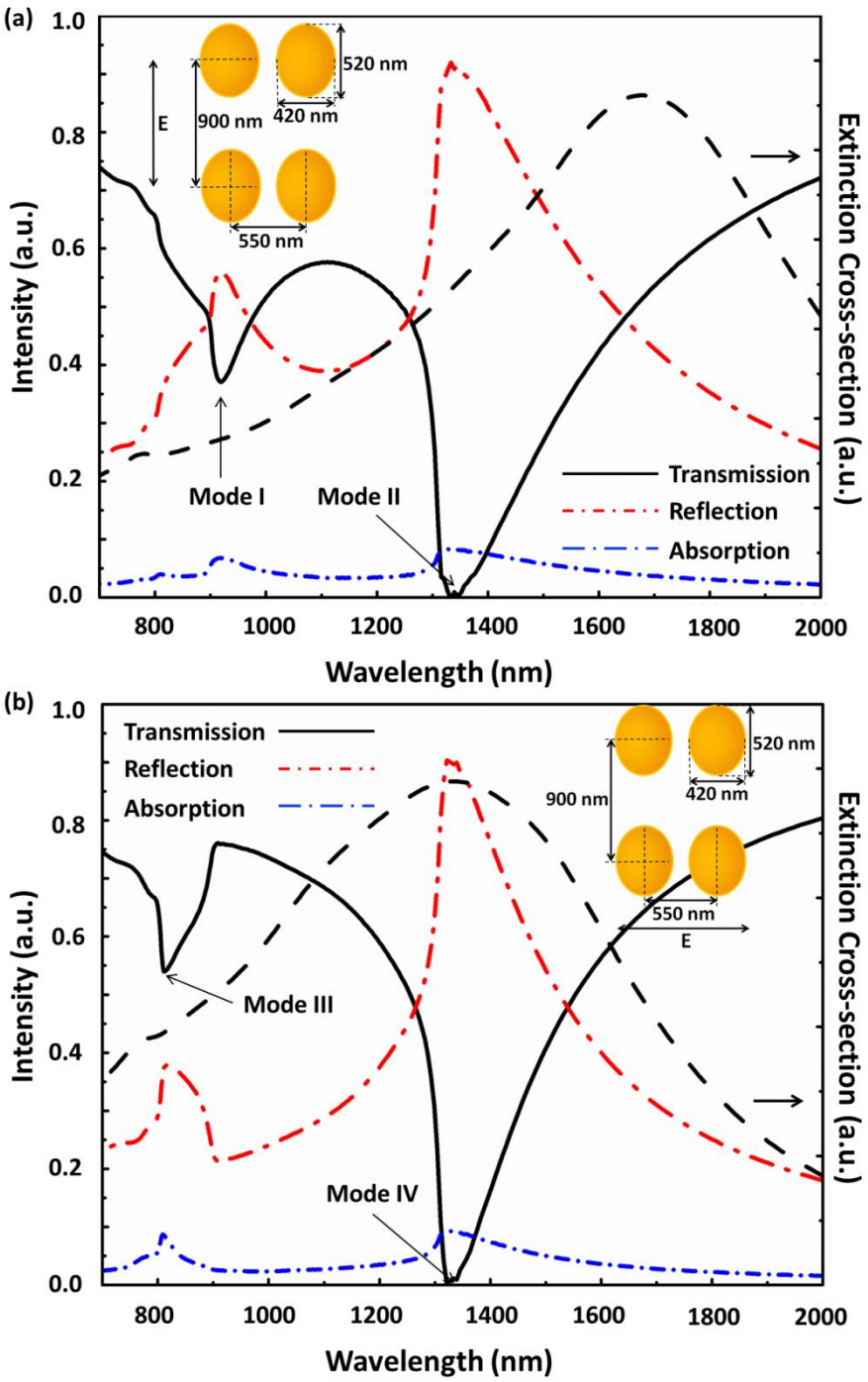


Figure 5.3 Simulated spectra of Au nanorod array at polarization along (a) *y* and (b) *x* directions, respectively. The nanorod array in the simulation has the dimension of 420×520×30 $nm^3$ and the periods of 550 and 900 nm along *x* and *y* directions, respectively.

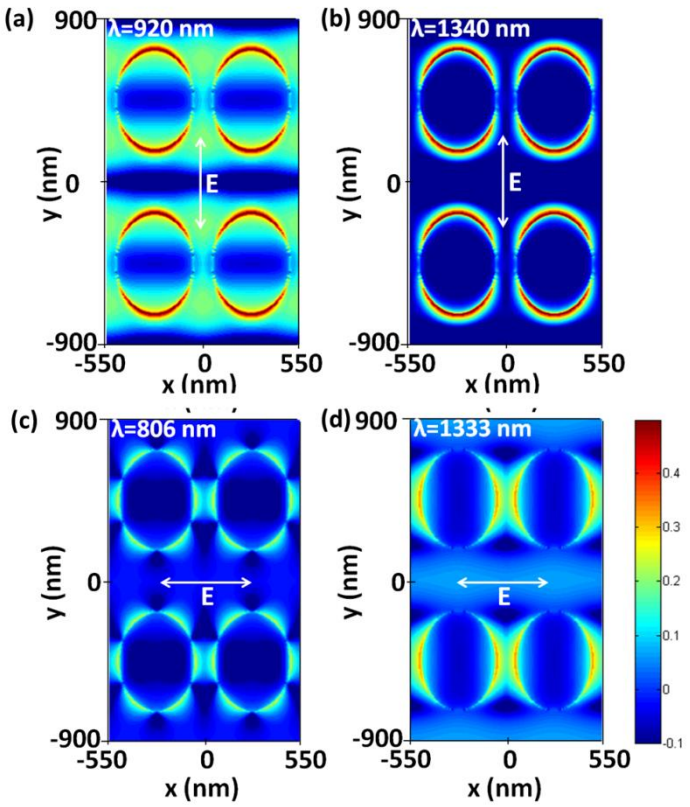


Figure 5.4 Simulated electric field intensity in log scale distribution at different resonance wavelengths under different light polarization directions. Plots (a) and (b) show log-scale electric field intensity distribution at the resonance wavelengths of 920 and 1340 nm under the light polarization along y direction. Plots (c) and (d) display log-scale electric field intensity distribution at the resonance wavelengths of 806 and 1333 nm under the light polarization along *x* direction. Field intensity profiles are captured by the *z*-normal plane at the middle height of the nanorod.

The electric-field intensity distribution at different resonance wavelengths is plotted in the log-scale in Figs. 5.4 (a)-(d). Near-field intensities at wavelengths of 920 and 806 nm are normalized to the maximum field intensities at the resonance wavelengths of 1340 and 1333 nm, respectively. For the mode I (Fig. 5.4 (a)), near-field intensities not only are highly concentrated at the edges of the nanorods, but also show the signatures of the standing waves of the surface plasmon polaritons with strong resonance intensity in the plane of an array. On the other hand, for the mode II (Fig. 5.4

(b)), the electric field intensity is only confined at the edges of the nanorods for the resonance, which is attributed to a dipole resonance. In addition, another dipole resonance for mode IV induced by the geometry of the nanorod is also observed in Fig. 5.4 (d) and coupled with neighbors. The mode III positioned at 806 nm corresponds to a higher order multipolar resonances arising from the phase retardation of the incident wave within a single particle [29]. Six-lobe pattern around the edge of the nanorods with weaker intensity is clearly observed in Fig. 5.4 (c).

Table 5.1 is a summary of resonances and linewidths for nanorod array induced by the light polarization along the long and short axes of nanorods, respectively.

Table 5.1 Simulated resonance wavelength and FWHM for nanorod array and a single nanorod.

| No. | Resonance Mode | Resonance Wavelength (nm) | FWHM (nm) |
|---|---|---|---|
| Nanorod array | Mode I (SLRs) | 920 | 85 |
| | Mode II (LSPR) | 1340 | 195 |
| | Mode III (Higher Order Resonance) | 806 | 61 |
| | Mode IV (LSPR) | 1333 | 199 |
| Single nanorod | Longitudinal | 1676 | 692 |
| | Transversal | 1387 | 930 |

To measure the width of the spectra, we used a Lorentzian line shape in the frequency domain:

$$L(f) = L_0 + \frac{2A}{\pi}\left[\frac{w}{4(f-f_0)^2+w^2}\right] . \quad \text{(Eq. 5.2)}$$

To fit the peaks, $f$ is the frequency, $f_0$ is the peak position, and $w$ is the full width at half maximum (FWHM) of the frequency. The calculated results are displayed in Table 5.1.

### 5.2.4. Evaluation of RI sensing performance

The simulated spectra of a periodic array of nanorods reveal that four resonance modes can be excited by the normal incident with the light polarization along *x* and *y* directions. These resonance modes make it possible to concentrate light into a small volume and generate high intense electric fields, which could be applied to plasmonic sensing. In order to study the response of these resonance modes to the refractive index of the surrounding medium, we have simulated the transmission spectra of nanorod array in the media with a gradual change in the refractive index (Fig. 5.5). The refractive indices of the surrounding media vary from 1 to 1.5 at a step of 0.1, which can be set up in the FDTD simulation. First of all, it is found that all resonance modes shift to a longer wavelength. This trend in the spectra arises from a gradual increase in the dielectric function of the media. Secondly, resonance wavelength shifts of Au nanorod array can be linearly fitted to obtain their bulk RI sensitivity, which is defined in Chapter 2, Eq. 2.10. It is clearly observed that the RI sensitivity of SLR (mode I) is 837 nm/RIU, while modes II and III have the RI sensitivity of 233 and 464 nm/RIU, respectively. In addition, higher-order multiple mode provides the lowest RI sensitivity with

the value of 219 nm/RIU. The calculated results are summarized in Table 5.2. In conclusion, nanorod array for the SLR mode displays greater RI sensitivity than LSPR and higher-order multiple modes. It indicates that the SLR mode can be a good choice to detect small changes in the refractive index, which is also reported by Zou [30]. In addition, SLR mode can both propagate on the surface and localize near-field energy around the edges of the nanorod, thus providing a larger contact area for the detection of small molecules (Fig. 5.4 (a)). Finally, the figure of merit (FOM) of these modes is calculated by dividing the refractive index sensitivity by the FWHM of resonance peak, which is widely used to characterize a nanoparticle's sensing capability [6].

Table 5.2 Simulated spectral shift and RI sensitivity of different resonance modes of nanorod array.

| **Resonance Mode** | **Resonance Wavelength (nm)** | **FWHM (nm)** | **RI sensitivity (nm/RIU)** | **Figure of Merit** |
|---|---|---|---|---|
| Mode I (SLRs) | 920 | 85 | 837 | 9.85 |
| Mode II (LSPR) | 1340 | 195 | 233 | 1.19 |
| Mode III (Higher Order Resonance) | 806 | 61 | 219 | 3.59 |
| Mode IV (LSPR) | 1333 | 199 | 464 | 2.33 |

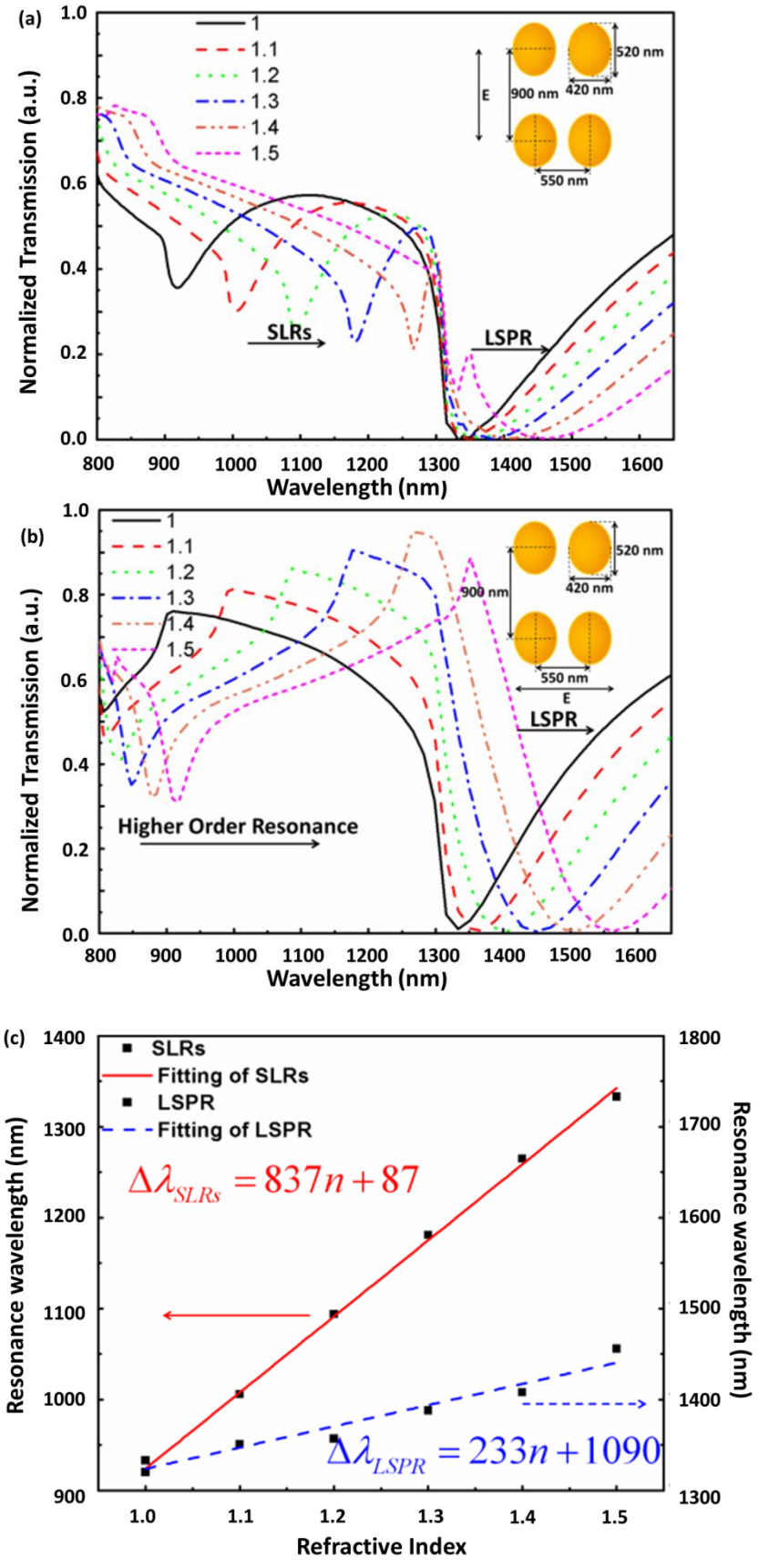
(a)
Normalized Transmission (a.u.)
Wavelength (nm)
1
1.1
1.2
1.3
1.4
1.5
E
900 nm
520 nm
420 nm
550 nm
SLRs
LSPR
(b)
Normalized Transmission (a.u.)
Wavelength (nm)
Higher Order Resonance
LSPR
(c)
SLRs
Fitting of SLRs
LSPR
Fitting of LSPR
$\Delta\lambda_{SLRs} = 837n + 87$
$\Delta\lambda_{LSPR} = 233n + 1090$
Resonance wavelength (nm)
Refractive Index

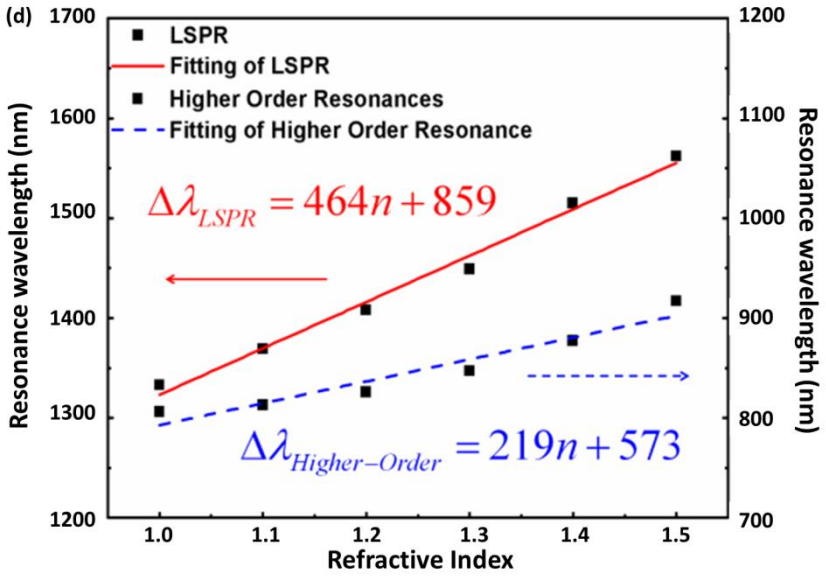


Figure 5.5 Simulated refractive index sensing sensitivities of nanorod array for different resonance modes (e.g. I, II, III, IV) under the light polarization along *y* (plots (a) and (c)) and *x* (plots (b) and (d)) directions. Plots (a) and (b) display the simulated far-field optical transmission spectra of nanorod array in different surrounding media with refractive indices ranging from 1 to 1.5 at a step of 0.1. Plots (c) and (d) indicate resonance wavelength shift as a function of the refractive index (*n*) as well as their corresponding refractive index sensing sensitivities obtained by fitting the linear function.

### 5.3. Experimental details

Based on the simulation mentioned above, a periodic array of nanorods can provide surface lattice resonance (SLR) with a narrow line shape in the far-field optical spectra, with much better resonance quality compared to the single nanoparticle case. This designed nanorod array can provide high RI sensing sensitivity in the simulation. In this section, the detailed fabrication and characterization of nanorod array will be presented, followed by the experimental results and sensing measurement of nanorod array.

### 5.3.1. Fabrication process of the designed nanorod array

The desired two-dimensional (2D) gold nanorod array was fabricated by laser interference lithography [31]. The method of preparation involves the double exposure of the coated photoresist on a glass substrate to the interference pattern. After the exposure, the photoresist is chemically developed and the resulting profile is transferred to the substrate by RIE etching. This produces a robust and large area periodic nanostructure with a well-defined pitch. The pitch is determined by the incident angle, given by Eq. 2.14. The subsequent deposition of Cr/Au films and the lift-off produce 2D gold nanostructures.

In the exposure, the sample is exposed twice with two different incident angles ($\theta$ and $\theta'$) and a rotation angle ($\alpha$) of $90\,^{\circ}$ between them, in order to realize periodic nanorod hole arrays in the resist arranged in the rectangular lattice shape. Firstly, the sample is exposed for 90 s by the interference patterning under an incident angle ($\theta$) of $17\,^{\circ}$. The sample is then rotated $90\,^{\circ}$ on the sample holder and exposed for another 90 s again with an incident angle ($\theta'$) of $10\,^{\circ}$. The periodicities of 550 and 900 nm in *x* and *y* directions can be obtained by the double exposure of the interference patterns, as shown in Fig. 5.6. The dimension of the nanorod array is $420 \times 520 \times 30$ nm$^3$.

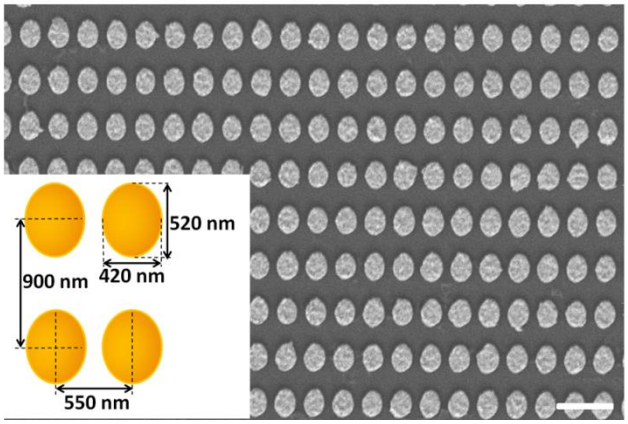


Figure 5.6 SEM image of a nanorod array with the periodicities ($P_x$ and $P_y$) of 550 and 900 nm, respectively. The schematic diagram of the nanorods is inserted in the bottom-left of the figure.

### 5.3.2. Characterization of the fabricated nanorod array

Far-field transmission spectra of the nanorod array were characterized using the variable angle spectroscopic ellipsometer (VASE) under the *p*- and *s*-polarized light irradiation at normal incidence. Figure 5.7 displays the measured optical far-field transmission spectra of the nanorod array under light polarization along *y* (black solid line) and *x* (black dashed line) axes of the nanorods. The measured spectra were normalized to focus on the spectral shift. As seen in Fig. 5.7, two resonances are observed when light is illuminated along *y* direction, with a good agreement with the simulated result. They are located at 915 nm and 1310 nm, respectively. These resonances correspond to the SLR and LSPR modes, which can be analyzed using the electric field distribution in Figs. 5.4 (a)-(b).

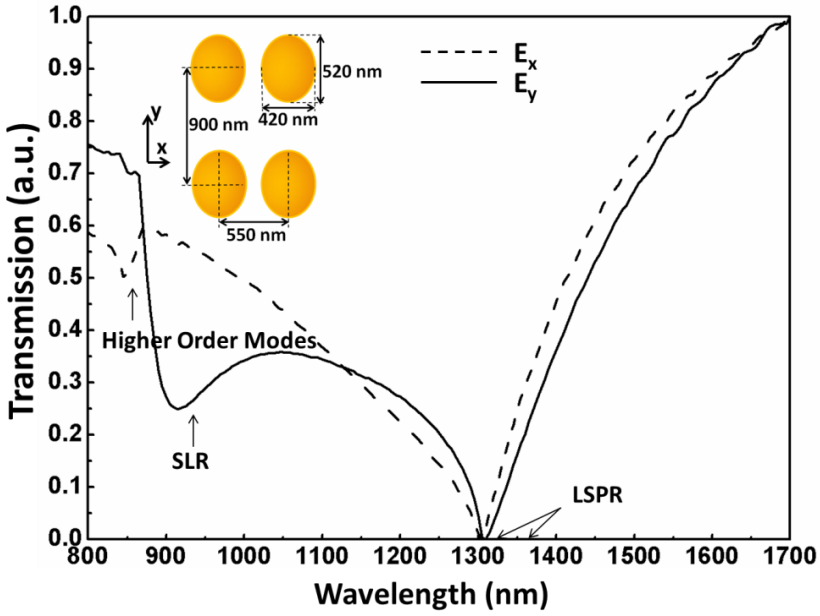


Figure 5.7 Measured optical transmission spectra of a gold nanorod array under light polarization along *y* (black solid line) and *x* (black dashed line) directions. The nanorod array has the dimension of 420×520×30 $nm^3$ and the periods of 550 and 900 nm in *x* and *y* directions, respectively.

On the other hand, other two resonances are observed under light polarization along *x* direction corresponding to a higher-order multiple mode and LSPR mode (Figs. 5.4 (c) and (d)), with the peak positions at 845 and 1305 nm. This phenomenon indicates that the SLR resonance is selected by the light polarization and can only be induced by the light polarization parallel to *y* direction. The LSPR mode is also determined by the geometry of the nanorods, resulting in broad dipolar resonance observed under both light polarization along *x* and *y* directions. Table 5.3 summarizes the resonance properties of these modes.

Table 5.3 Measured resonance wavelength and FWHM for nanorod array and a single nanorod.

| Polarization Direction | Resonance Mode | Resonance Wavelength (nm) | FWHM (nm) |
|---|---|---|---|
| Ex | SLR (Mode I) | 915 | 76 |
| | LSPR (Mode II) | 1305 | 182 |
| Ey | Higher-order Multiple (Mode III) | 845 | 27 |
| | LSPR (Mode IV) | 1310 | 246 |

### 5.3.3. Evaluation of RI sensitivity of nanorod array

According to our simulation, the SLR mode could provide the maximum RI sensitivity in all these different modes. In our experiment, the SLR mode's response to the refractive index change is our focus in this work. The measurements of RI sensitivity for the SLR mode were performed through immersing the sample inside the sealed quartz chamber in the surroundings media of different refractive indices, e.g. air (black solid line), water (red dash line), acetone (green dot line) and IPA (blue dash dot line), as shown in Fig. 5.8. Their corresponding refractive indices are 1.0000, 1.3228, 1.359, 1.3776, respectively [14]. It can be seen that resonance wavelength for the SLR mode red-shifts from 915 to 1215 nm when the refractive index varies from 1.0000 to 1.3776. The experimental data for the SLR mode were linearly fitted to determine its RI sensitivity, as shown in Fig. 5.8 (b). The measured sensitivity for SLR is 799 nm/RIU, which is a good agreement with the simulated results.

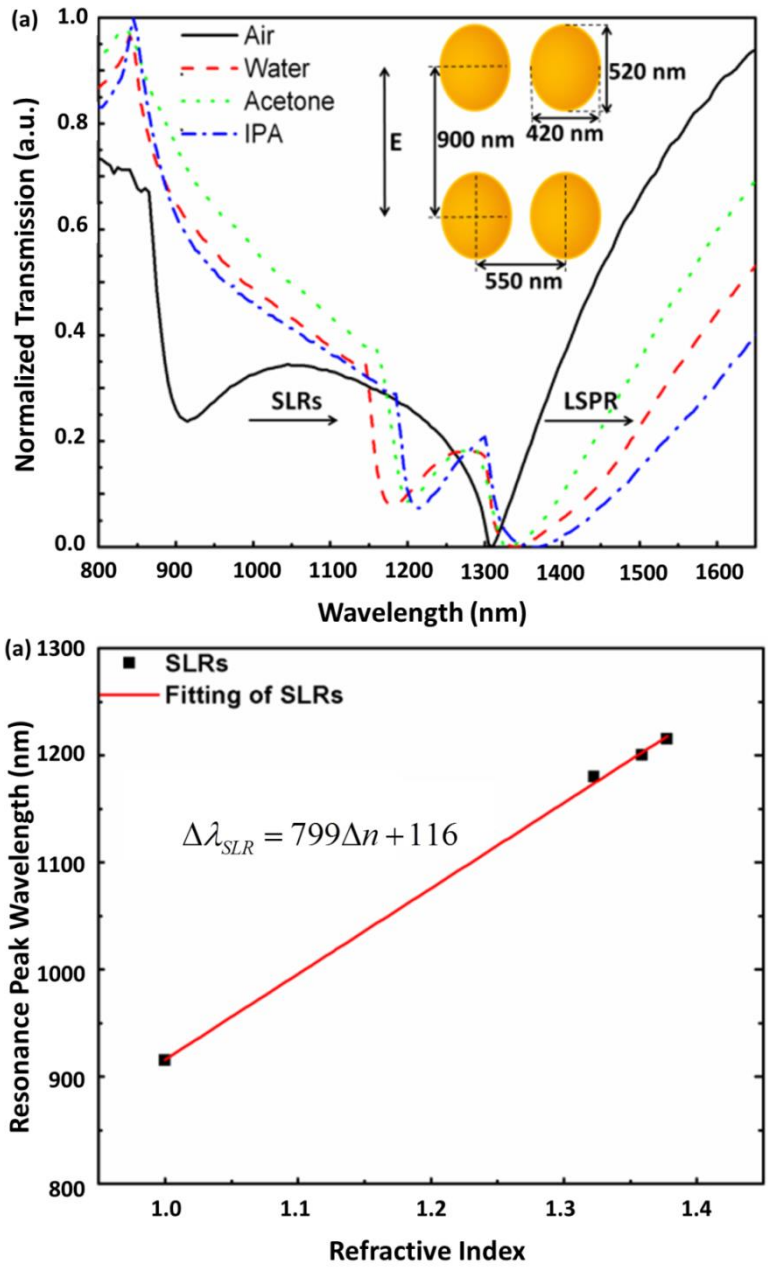


Figure 5.8 (a) Measured optical transmission spectra of nanorod array in different surrounding media under light polarization along the long axis of the nanorod and (b) its corresponding refractive index sensitivity. The transmission dips of the SLR red-shift from 915, 1180, 1200 to 1215 nm, respectively. Black square dots are experimental points. Red solid line linearly fits to the data, giving a RI sensitivity of 799 nm/RIU for the SLR mode.

## 5.4. Discussion

### 5.4.1. Excitation of surface lattice resonance in an array of gold nanorods

In an array of nanorods, collective plasmonic excitations are observed both in the simulated and experimental results, as shown in Figs. 5.3 (a) and 5.7, respectively. There are two transmission dips that are located at 920 and 1340 nm in Fig. 5.3 (a), corresponding to two important resonance modes: SLR mode and LSPR mode. This SLR mode is dispersive and spectrally narrow collective resonance arising from the diffractive coupling of the localized surface plasmon of the individual particles [16-26]. This coupling generally occurs near the critical condition at which a grating diffraction changes from radiating to evanescent [18]. This condition is determined by the first grating order at gazing angles (i.e. in the sample plane), which is closely associated with the Rayleigh anomalies. According to the theory [16-26], the Rayleigh anomalies [31] are solutions to the equation:

$$k_{out}^2 = k_{in}^2 sin^2(\theta) + m_1^2\left(\frac{2\pi}{a_x}\right) + m_2^2\left(\frac{2\pi}{a_y}\right) + 2k_{in}\sin(\theta)\, m_1(2\pi/a_x) \text{ , (Eq. 5.3)}$$

where $k_{in}$ and $k_{out}$ are the modules of the incident and scattered wave vectors, $m_j$ ($j$ = 1, 2) are the integers defining the order of diffraction, $a_x$ and $a_y$ are the lattice periods along *x* and *y* directions. In our case, the first grating order is calculated by this equation and is equal to 900 nm, where $\theta$ = 0 °, $a_x$ = 550 nm and $a_y$ = 900 nm. In Fig. 5.3 (a), the resonance positioned at 920 nm can be confirmed by the SLR mode according to the theory, displaying a narrow

linewidth. Moreover, the appearance of the SLR mode results in a slight blue-shift for the LSRP mode, compared to that of the single nanorod. This phenomenon is also reported by the previous study [18]. The retarded dipole interaction among nanoparticles leads to the redistribution of near-field energy. Near-field energy located at the edges of the nanorods is reduced due to the conservation of energy in the system, consequently, the resonance wavelength of the LSPR mode shifts towards a shorter wavelength.

### 5.4.2. Radiative damping in Au nanorod array

It is clearly observed that the linewidths of the SLR and LSPR modes for nanorod array are both reduced, which are determined by the radiative and non-radiative damping of nanostructures. Nonradiative damping processes both electron scattering in the metal and dissipate oscillation energy into heat [33]. Radiative damping processes are caused by energy radiated into the optical far-field by the collective electron oscillation, and increases with particle size. For a small single particle, the radiation damping is small. While for the particle dimension become comparable to the incident light wavelength, the effect of radiation damping becomes important [34]. The damping due to the radiation can decrease the enhancement by many orders of magnitude and causes a significant broadening of the particle plasmon resonance. In our case, nanorods with the dimension close to the light wavelength possess a large radiative damping of the dipole induced by the individual nanorod. When they are arranged in array, the dipoles of the individual collectively couple with the radiated fields of the other dipoles, resulting in a partial cancellation of the radiative damping of the individuals as well as narrow linewidths for the

resonances. Therefore, the collective plasmonic excitation opens a new door to narrow the linewidths, and provides an good opportunity to improve the detection resolution for the RI sensing.

### 5.4.3. RI sensing performance for SLR mode

It is found that an array of nanorods provides a high performance in the RI sensing. RI sensitivity for the SLR mode reaches to 799 nm/RIU and FOM exceeding 9. Our nanosensors can be a good choice for near-infrared biosensing, which working wavelength range is from 920 to 1300 nm. Compared to the previous studies, our results can be superior over many other sensors, such as single silver spherical nanoparticle [35], gold nanodisk trimers [36] and silver nanodisk arrays [37]. For example, single silver spherical nanoparticle at a diameter of 35 nm displays the RI sensitivity of 161 nm/RIU for the LSPR mode [35] and FOM of 2.2 [38]. Gold nanodisk trimers fabricated by EBL can deliver the RI sensitivity up to 373 nm/RIU and FOM of around 1.2 in the near-IR range [36]. In addition, a periodic array of Ag nanoparticles at a diameter of 50 nm and a spacing of 420 nm can shift from 432.5 to 566.3 nm in water, with RI sensitivity up to 406 nm/RIU and FOM of 6.69 [32]. Planar metamaterials using extraordinary induced transmission (EIT) provide a similar RI sensitivity of 725 nm/RIU using the EBL and FOM of 7.4 [37]. Compared to previous results, we demonstrate a straightforward method to design and fabricate large area nanosensors with a high RI sensitivity and FOM, providing a new chance to detect small bio/chemical molecules.

## 5.5. Summary

In conclusion, we demonstrate the high sensitivity sensing via a large area of gold arrays. High spectral shifts for the SLR mode were obtained in the surrounding media with the gradually variation of refractive index. SLR mode can be selected by the incident polarization direction along the long axis of the nanorod. A refractive index sensitivity of around 800 nm/RIU is achieved in experiment. This proposed approach to utilize surface lattice resonance for the sensing is simple and easy to realize for chip-scale biological and chemical sensing.

## 5.6. References

[1] J. N. Anker, W. P. hall, O. Lyandres, N. C. Shah, J. Z., and R. P. V. Duyne, "Biosensing with plasmonic nanosensors", Nat. Mater. **7**, 442-453 (2008).

[2] A. V. Kabashin, P. Evans, S. Pastkovsky, W. Hendren, G. A. Wurtz, R. Atkinson, R. Pollard, V. A. Podolskiy, and A. V. Zayats, "Plasmonic nanorod metamaterials for biosensing", Nat. Mater. **8**, 867-871 (2009).

[3] A. V. Kabashin and P. I. Nikitin, "Surface plasmon resonance interferometer for bio- and chemical-sensors", Opt. Commun. **150**, 5-8 (1998).

[4] N. Nath and A. Chilkoti, "A colorimetric gold nanoparticle sensor to interrogate biomolecular interactions in real time on a surface", Anal. Chem. **74**, 504-509 (2002).

[5] L. Xu, L. S. Tang, and M. H. Hong, "Tuning of localized surface plasmon resonance of well-ordered Ag/Au bimetallic nanodot arrays by laser interference lithography and thermal annealing", App. Opt. **50**, G74-9, (2011).

[6] K. A. Willets and R. P. V. Duyne, “Localized surface plasmon resonance spectroscopy and sensing”, Annu. Rev. Phys. Chem. **58**, 267-97 (2007).

[7] H. J. Chen, X. S. Kou, Z. Yang, W. H. Ni, and J. F. Wang, “Shape- and size-dependent refractive index sensitivity of gold nanoparticles,” Langmuir **24**, 5233-5237 (2008).

[8] S. L. Teo, V. K. Lin, R. Marty, N. Large, E. A. Lload, A. Arbouet, C. Girard, J. Aizpurua, S. Tripathy, and A. Mlayah, “Gold nanoring timers: a versatile structure for infrared sensing,” Opt. Express **18**, 22271-22282 (2010).

[9] N. Verellen, P. V. Dorpe, C. Huang, K. Lodewijks, G. A. E. Vandenbosch, L. Lagae, and V. V. Moshchalkov, “Plasmon line shaping using nanocrosses for high sensitivity localized surface plasmon resonance sensing,” Nano Lett. **11**, 391-397 (2011).

[7] R. Bukasov and J. S. Shumaker-Parry, “Highly tunable infrared extinction properties of gold nanocrescents”, Nano Lett. **7**, 1113-1118 (2007).

[8] B. Lamprecht, G. Schider, R. T. Lechner, H. Ditlbacher, J. R. Krenn, A. Leitner, and F. R. Aussenegg, “Metal nanoparticle gratings: influence of dipolar particle interaction on the plasmon resonance”, Phys. Rev. Lett. **84**, 4721-4724 (2000).

[9] S. L. Zou and G. C. Schatz, “Theoretical studies of plasmon resonances in one-dimensional nanoparticle chains: narrow lineshapes with tunable widths”, Nanotechnology **17**, 2813-2820 (2006).

[10] G. Vecchi, V. Giannini, and J. G. Rivas, “Surface modes in plasmonic crystals induced by diffractive coupling of nanoantennas”, Phys. Rev. B **80**, 201401-1–201401-4 (2009).

[11] G. Vecchi, V. Giannini, and J. G. Rivas, “Shaping the fluorescence emission by lattice resonances in plasmonic crystals of nanoantennas”, Phys. Rev. Lett., **102**, 146807-1−146807-4 (2009).

[12] B. Ng, S. M. Hanham, V. Giannini, Z. C. Chen, M. Tang, Y. F. Liew, N. Klein, M. H. Hong, and S. A. Maier, “Lattice resonances in antenna arrays for liquid sensing in the terahertz regime”, Opt. Express **19**, 14653-14661 (2011).

[13] T. B. O’Reilly and H. I. Smith, “Linewidth uniformity in Lloy’s mirror interference lithography systems”, J. Vac. Sci. Technol. B **26**, 2131-2134 (2008).

[14] D. R. Lide, Handbook of Chemistry and physics, 87$^{th}$ ed., CRC Press, Florida (2006).

[15] K. T. Carron, W. Fluhr, M. Meier, and A. Wohaun, “Resonances of two-dimensional particle gratings in surface-enhanced Raman scattering,” J. Opt. Soc. Am. B **3**, 430-440 (1986).

[16] V. A. Markel, “Coupled-dipole approach to scattering of light from a one-dimensional periodic dipole structure,” J. Mod. Opt. **40**, 2281 (1993).

[17] S. Zou, N. Janel, and G. C. Schatz, “Silver nanoparticle array structures that produce remarkable narrow plasmon lineshapes,” J. Chem. Phys. **120**, 10871-10875 (2004).

[18] L. L. Zhao, K. L. Kelly, and G. C. Schatz, “The extinction spectra of silver nanoparticle arrays: influence of array structures on plasmon resonance wavelength and width,” J. Phys. Chem. B **107**, 7343-7350 (2003).

[18] R. Adato, A. A. Yanik, C. H. Wu, G. Shvets, and H. Altug, “Radiative engineering of plasmon lifetimes in embedded nanoantennas arrays,” Opt. Express **18**, 4526-4537 (2010).

[19] V. Giannini, G. Vecchi, and J. G. Rivas, “Light up multipolar surface plasmon polaritons by collective resonances in arrays of nanoantennas,” Phys. Rev. Lett. **105**, 266801-1 – 266801-4 (2010).

[20] J. N. Anker, W. P. Hall, O. Lyandres, N. C. Shan, J. Zhao, and R. P. V. Duyne, “Biosensing with plasmon nanosensors,” Nat. Mater. **7**, 442-453 (2008).

[21] V. Giannini, A. I. Fernandez-Dominguez, S. C. Heck, and S. A. Maier, “Plasmonic nanoantennas: fundamentals and their use in controlling the radiative properties of nanoemitters,” Chem. Rev. 111, 3888-3912 (2011).

[22] V. A. Markel, “Divergence of dipole sums and the nature of non-Lorentzian exponentially narrow resonances in one-dimensional periodic arrays of nanospheres,” J. Phys. At. Mol. Opt. Phys. **38**, L115-L121 (2005).

[23] B. Auguie, and W. L. Barnes, “Collective resonances in gold nanoparticle arrays,” Phys. Rev. Lett. **101**, 143902 (2008).

[24] V. G. Kravets, F. Schedin, and A. N. Grigorenko, “Extremely narrow plasmon resonances based on diffraction coupling of localized plasmons in arrays of metallic nanoparticles,” Phys. Rev. Lett. **101,** 087403 (2008).

[25] X. M. Bendana and F. J. G. de Abajo, “Confined collective excitations of self-standing and supported planar periodic particle arrays,” Opt. Express **17**, 18826 (2008).

[26] C. Sonnichsen, T. Franzl, T. Wilk, G. von Plessen, and J. Feldmann, “Drastic reduction of plasmon damping in gold nanorods,” Phys. Rev. Lett. **88**, 077402-1- 077402-4 (2002).

[27] Lumerical FDTD Solutions. http:// www.lumerical.com.

[28] P. B. Johnson and R. W. Christy, “Optical constants of the noble metals,” Phys. Rev. B **6**, 4370-4379 (1972).

[29] S. A. Maier and H. A. Atwater, “Plasmonics: localization and guiding of electromagnetic energy in metal/dielectric structures,” J. Appl. Phys. **98**, 011101 (2005).

[30] S. Zou and G. C. Schatz, “Narrow plasmonic/photonic extinction and scattering line shapes for one and two dimensional silver nanoparticle arrays,” J. Chem. Phys. **121**, 12606 (2004).

[31] J. de Boor, N. Geyer, J. V. Wittemann, U. Gosele and V. Schmidt, “Sub-100 nm silicon nanowires by laser interference lithography and metal-assisted etching,” Nanotechnology **21**, 095302 (2010).

[32] L. Rayleigh, “On the dynamical theory of gratings,” Proc. R. Soc. Lond., A Contain Pap. Math. Phys. Character **79**, 399-416 (1907).

[33] C. Novo, D. Gomez, J. P. Juste, Z. Zhang, H. Petrova, M. Reismann, P. Mulvaney, and G. V. Hartland, “Contributions from radiation damping and surface scattering to the linewidth of the longitudinal plasmon band of gold nanorods: a single particle study,” Phys. Chem. Chem. Phys. **8**, 3540-3546 (2006).

[34] A. Wokaun, J. P. Gordon and P. F. Liao, “Radiation damping in surface-enhanced Raman scattering,” Phys. Rev. Lett. **48**, 957-960 (1982).

[35] A. D. McFarland, R. P. Van Duyne, “Single silver nanoparticles as real-time optical sensors with zeptomole sensitivity,” Nano Lett. **3**, 1057-1062 (2003).

[36] S. Tripathy, A. Mlayah, “Dual wavelength sensing based on interacting gold nanodisk trimers,” Nanotechnology **21**, 305501 (2010).

[37] N. Liu, T. Weiss, M. Mesch, L. Langguth, U. Eigenthaler, M. Hirscher, C. Sonnichsen, H. Giessen, “Planar metamaterial analogue of electromagnetically induced transparency for plasmonic sensing,” Nano Lett. **10**, 1103-1107 (2010).

[38] K. M. Mayer, and J. H. Hafner, “Localized surface plasmon resonance sensors,” Chem. Rev. 111, 3828-3857 (2011).

# Chapter 6 Tuning Surface Lattice Resonance by Lattice Period of Nanorod Array for Refractive Index Sensing

The previous chapter has shown that the diffraction coupling of the localized plasmons in an array of nanorods can induce a strong modification in the transmission characteristics, leading to a narrow line shape in the transmission spectra and strong near-field spatial distribution extending in the plane of the array. This resonance gives the ability to achieve a large refractive index sensitivity and high figure of merit, which has been confirmed by our simulation and experimental results. This chapter will demonstrate the tuning of the surface lattice resonance through varying the lattice constant of gold nanorods arrays. By detailed comparison of the optical properties and near-field intensity distribution at plasmon resonances for nanorod array with different lattice constants, we demonstrate that the spectral wavelengths of the surface lattice resonance (SLR) and the localized surface plasmon resonance (LSRP) can be flexibly tuned by proper control of the diffractive coupling of dipoles. The spectral width of the LSPR induced by the individual nanorod is gradually reduced with an increase in the lattice constant. This provides us with a strategy to tune the spectral wavelength over a broad range by a subtle change in the lattice constant. In addition, the refractive index sensitivity (RI) of nanorod array with a lattice constant of 1100 nm along the long axis of the nanorod is measured, showing a high RI sensitivity reaching 1055 nm/RIU and a figure of merit (FOM) around 9.

In Section 6.1, the interplay between the grating diffraction and the localized surface plasmons among plasmonic crystals will be introduced. The optical properties and near-field enhancements of nanorod array with the various lattice constants along the long axis of the nanorod will be discussed in Section 6.2. In Section 6.3, we employ simple and easily producible structure parameters to realize nanorod array over a large area by LIL and lift-off, followed by the measurement of the optical properties and RI sensitivity. At the end of this chapter in Section 6.4, the conclusions of this work will be summarized.

## 6.1. Introduction

Localized plasmon resonances in small metallic nanostructures have attracted interests in the scientific community over a century, due to their ability to support collective electron oscillations (plasmons). These resonances allow us to spectrally tune absorption and scattering, electromagnetic couple to nanoscale objects, locally enhance and strongly confine the electromagnetic field at length scales much smaller than the optical diffraction limit [1]. Along with the development of nanofabrication techniques, more attention has been paid to the enhanced local electromagnetic fields in well-controlled structures [2, 3], giving rise to the improvement in the sensitivity of various spectroscopic techniques, such as Raman scattering or infrared absorption spectroscopy and refractive index sensing [4-7]. Plasmonic sensing has recently been the subject of intense research efforts due to its numerous applications in the area of the diagnosis and monitoring of diseases, drug

discovery, proteomics, and the environmental detection of pollutants and/or biological agents [8].

One of main challenges in the field of plasmonic sensing in the last decade is how to engineer nanostructures for the effective amplifications of refractive index (RI) sensitivity and figure of merit [9]. Many efforts have been devoted to increase light-matter interaction through high field enhancements on sharp nanoparticle vertices, closely spaced nanoparticle assemblies [10-12] or a periodic array of nanostructures. Among these methods, far-field coupling in an ensemble of metal nanoparticles can excite surface lattice resonance (SLR) by the diffractive coupling of dipoles, allowing for the improvement of the resonant quality and the achievement of higher electric field enhancement factors, compared with the single nanoparticle case [16-19]. It has been found that this coupling can achieve narrow resonant features and highly intense fields at plasmon resonances, resulting in a significant density of optical states as a result of pronounced improvement in light extraction [10]. In addition, these resonant features can be realized using simple and straightforward nanostructures, such as 1D and 2D nanoparticles [16-21] or nanorods [22-24] as well as plasmonic grating [25-28]. It is extremely useful to fabricate them by using laser interference lithography and integrate them into the lab-on-chip, thus rendering it possible for the detection of bio/chemical molecules in real time.

Attempts at exciting and tuning the surface lattice resonance have been studied [16-28]. It has been shown that tuning the radiative coupling of surface plasmons to diffracted orders can be achieved by altering the shapes and dimensions of metal nanostructures [24], providing evidence that the

properties of the SLR mode is strongly dependent on the geometry of the individual nanoparticles. Moreover, active tuning of the lattice resonance has also been demonstrated by baking phase-change materials sandwiched between a nanodisk array and the quartz substrate [29], which is due to the variation of the dielectric constant of the surrounding media. However, the mechanisms and regimes of interactions of the nanoparticles in the lattice are not yet well understood. A recent article showed that the optical properties of the lattice resonance in the ensemble of nanoparticles are influenced by the degree of disorder in the geometrical arrangement from a periodic to a disordered lattice [30], revealing the strong connection between the lattice arrangement and the surface lattice resonance. Tuning the surface lattice resonance in the array of nanostructures and optimizing the related electric field enhancements under different array parameters are important for many applications, such as plasmonic sensing and surface enhanced Raman spectroscopy. In this chapter, we study numerically how to tune spectral wavelengths and spectral widths of the surface lattice resonance as well as localized surface plasmon resonance through the variation of lattice constants of nanorod array. Near-field enhancements of nanorod array with different lattice constants are simulated to determine the critical distance between nanorods so as to obtain the most efficient coupling between the dipoles. After that, we experimentally demonstrate the sensing sensitivity of nanorod array, revealing that the RI sensitivity of nanorod array is strongly linked with the lattice constant.

## 6.2. Design and simulation of tuning surface lattice resonance with various lattice constants for nanorod array

In Chapter 5, we demonstrated that the collective plasmon interactions of nanorod array with the light field can cause the interesting diffraction phenomena, which can strongly modify the optical properties of the nanorod array with respect to the single nanorod case. Nanorod array exhibits optical responses dramatically different from those of an isolated nanorod, especially when the grating order is transformed from radiative to evanescent, because the optical energy scattered by one nanorod can be collected by a neighboring nanorod as plasmons, instead of decaying as free-space light [16-20]. The strongly coupled nanorods in a two-dimensional array produce narrow lattice plasmon resonances, due to the suppression of the radiative loss. Based on our previous design, nanorod array arranged in a rectangular lattice can narrow the lattice resonance. Therefore, tuning the surface lattice resonance can be accomplished by using the same geometry of the individual nanorod, but we achieve the tuning process through varying the lattice constant along the long axis of the nanorod. The lattice constant along the short axis of the nanorod is retained to the same value. In addition, the polarization of the normal incident light is oriented along the long axis of the nanorod, because only this polarization direction can excite the surface lattice resonance for our design, as reported in the previous chapter. Far-field optical properties and near-field enhancement of nanorod array with various lattice constants will be simulated, with special attention on the spectral positions and widths of the lattice

resonances and LSPR. RI sensing performance of nanorod array will be numerically calculated as presented below.

### 6.2.1. Far-field optical properties of nanorod array with various lattice constants

In Chapter 5, the designed nanorods have a dimension of 420×520×30 $nm^3$ and are arranged in the rectangular lattice shape, with the lattice period of 550 and 900 nm along the short ($P_x$) and the long axes ($P_y$) of the nanorod, respectively. Here, we retain the lattice period ($P_x$) as 550 nm, but the lattice period in *y* direction ($P_y$) is gradually changed from 800 to 1400 nm in steps of 100 nm. The sample is illuminated at normal incident with the light polarized in *y* direction. The wavelength range is varied from 700 to 1700 nm, which is a detectable range for the characterization by using our ellipsometer. Far-field optical transmission spectra are simulated using three-dimensional FDTD with periodic boundaries. In the calculation, we used dielectric constants measured and tabulated by Palik [31]. Figure 6.1 displays the simulated transmission spectra of nanorods with different lattice constants in *y* direction.

In Fig. 6.1, a collection of the calculated transmission spectra for nanorod array on glass substrate are depicted. Nanorod array exhibits two types of resonances: (1) a broad transmission dip located in a longer wavelength ranging from 1300 to 1900 nm due to the geometry of the individual nanorod; and (2) a narrow resonance feature positioned at a shorter wavelength ranging from 800 to 1400 nm, resulting from the diffractive coupling of dipoles. As the lattice constant ($P_y$) of the nanorod array gradually increases, the strong

modification of the spectra is clearly observed, leading to red-shifts of these two types of plasmon resonances. These phenomena highlight the fact that pronounced spectral features are strongly dependent on the lattice constant ($P_y$). We also note that the wavelengths of the surface lattice resonances (corresponding to local minima in transmission) for different nanorod arrays are directly linked to the first grating order, in which the dipole interactions occur under the condition that a first grating order changes from evanescent to radiative in air or the substrate layers [32]. In this case, the first grating order is equal to the lattice constant, and the normal incident light and air atmosphere are applied. According to Eq. 5.3, the wavelength of SLR occurs around the lattice periods of the nanorod array as shown in Fig. 6.2 (a). In particular, the SLR shifts towards longer wavelengths accompanying a gradual increase in the lattice constant ($P_y$), which is due to a modification of the plasmon resonance condition.

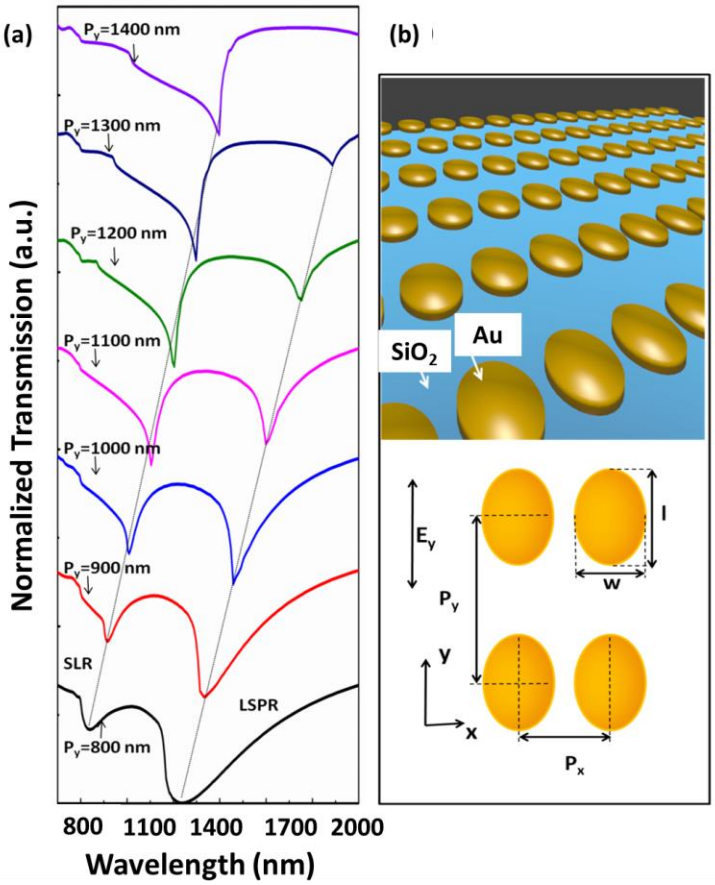


Figure 6.1 (a) Simulated transmission spectra of a nanorod array on glass substrate with various lattice constants in *y* direction. The sample is illuminated at normal incident light with the incident polarization along *y* direction. The schematic diagram of the nanorod array is shown in plot (b). The nanorod array has a dimension of 420×520×30 $nm^3$ and a fixed lattice period of 550 nm in *x* direction. The lattice period $P_y$ changes from 800 to 1400 nm in steps of 100 nm. Black, red, blue, magenta, green, olive, and violet solid lines correspond to the lattice periods of $P_y$ = 800, 900, 1000, 1100, 1200, 1300, and 1400 nm, respectively.

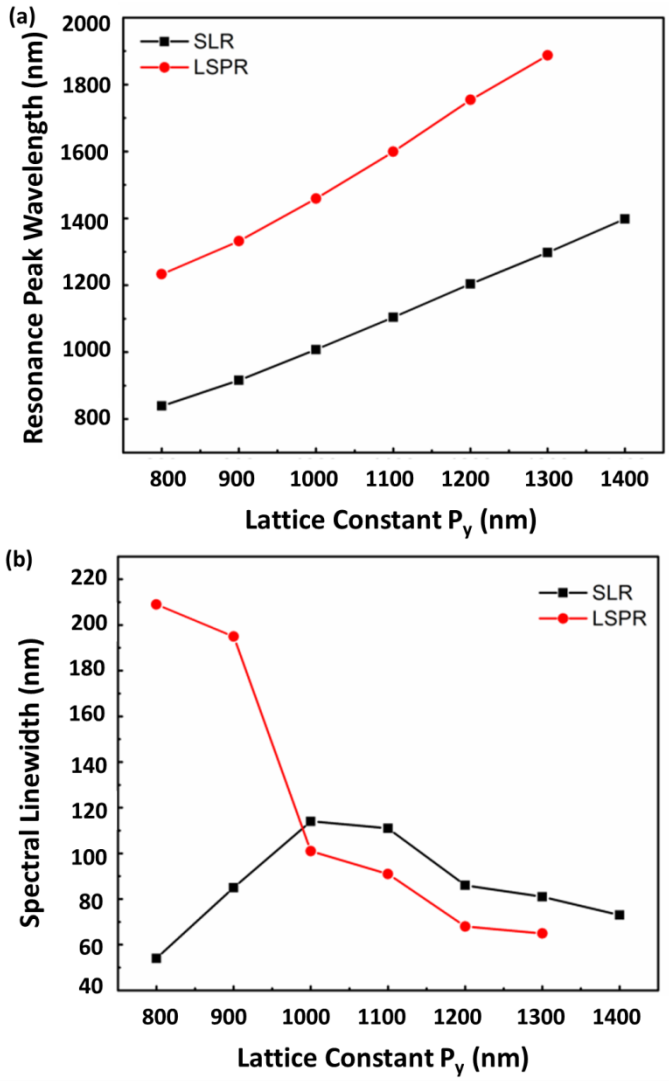


Figure 6.2 Resonance wavelength and spectral width as a function of the lattice constant in *y* direction: SLR mode (red circle) and LSPR mode (black square).

To further understand the interaction between these dipoles, our attention is then focused on the linewidths of these two resonances. Figure 6.2 (b) displays the spectral widths of the SLR and LSPR modes as functions of the lattice constant of nanorod array ($P_y$). The spectral width is calculated by fitting the transmission spectra using a Lorentzian profile. It is clearly observed that the linewidth of the LSPR mode is greatly reduced from 209 ($P_y = 800$ nm) to 65 nm ($P_y = 1300$ nm) with a gradual increase in the lattice

constant ($P_y$) of the nanorod array. This can be explained by the partial suppression of the radiative damping in the individual nanorods, which is strongly influenced by the diffractive interaction of the dipoles. This opens up new possibilities to reduce the radiative loss of the individual nanoparticles by manipulating the grating constants, which provides the potential to improve the quality factor of the resonance for application in high-resolution nanosensors. In contrast, the spectral width of the lattice resonance rises up to 114 nm when the lattice constant ($P_y$) is increased to 1000 nm, but drops to 65 nm for the lattice constant ($P_y$) at 1400 nm. This implies that the radiative damping of the lattice resonance is linked to the lattice constant ($P_y$), but the amplitude of this variation is not obvious as compared to the LSPR of the individual nanorod.

### 6.2.2. Near-field enhancements of nanorod array with various lattice constants

Far-field characteristics, such as transmission efficiency and spectral width, are strong indicators of the near-field behavior of the interactions between the diffractive coupling and the localized plasmons of the nanorods. Due to the suppression of radiation damping through the confinement of the electromagnetic field within the array, narrowing of the lattice resonances is observed. It has been shown that varying the lattice constants of the nanorod array can lead to strong modification of the optical response of the nanorod array. However, it is still not clear how near-field enhancements are

influenced by the lattice constant. In this part, numerical studies of near-field electromagnetic interactions in the array will be performed.

The lattice periods ($P_y$) of the nanorod array of 800, 1100, and 1300 nm are applied in the studies of near-field enhancements. The electric field intensity distribution in the *z*-normal, *x*-normal and *y*-normal at the lattice resonances and the dipole resonances is the subject of study in the interactions. Figure 6.3 presents the schematic diagram of the nanorods to indicate the coordinate system and the cutting planes.

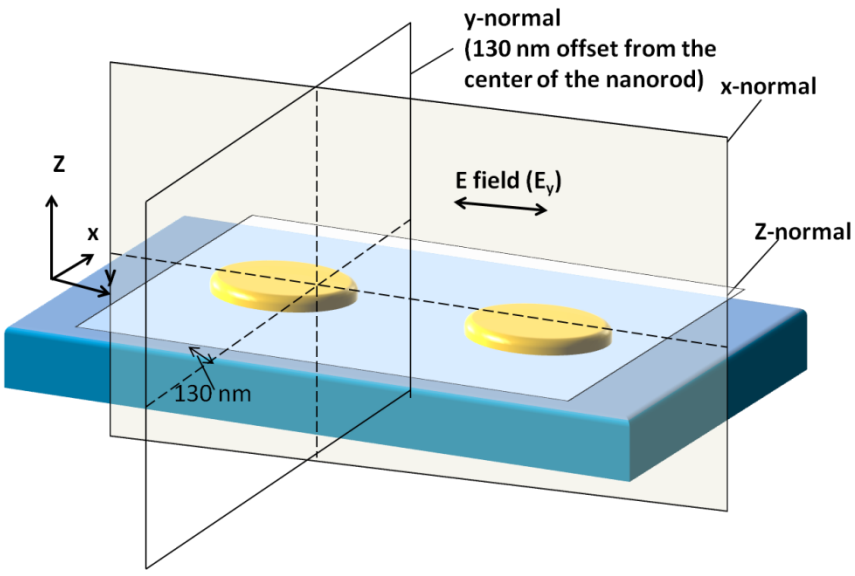


Figure 6.3 Schematic diagram of a nanorod array to indicate the coordinate system and the cutting planes used in the numerical simulation.

Figure 6.4 displays the log-scale electric field intensity distributions in the *z*-normal plane at the lattice resonances ($\lambda_{SLR}$=839, 1104, and 1298 nm) and the dipole resonances ($\lambda_{LSPR}$=1233, 1599, and 1877 nm) for nanorod array with various lattice constants ($P_y$ = 800, 1100, and 1300 nm), respectively. Firstly, dipole-like field distributions are depicted in Figs. 6.4 (b), (d) and (f),

in which the electric field intensities are concentrated at the edges of the nanorods. In contrast, at the lattice resonances (Figs. 6.4 (a), (c) and (e)), delocalized field distributions are observed, where the field intensities are enhanced in almost the whole unit cell. From the perspective of sensing, the delocalized nature of the lattice mode has advantages over LSPR owing to the fact that a large number of the molecules can efficiently couple to this mode due to its large contact area. Secondly, intense electric field intensities between nanorods in *x* direction can also be observed (Figs. 6.4 (a), (c) and (e)), indicating a coupling in the *x*-direction of the diffractive mode and LSPR mode. This fact is further confirmed by plotting the electric field intensity distributions in the *y*-normal plane cutting through the nanorod at its center (Figs. 6.5 (a)-(f)) and a 130 nm offset from the center (Figs. 6.6 (a)-(f)). Thirdly, among three different lattice constants in *y* direction, the diffractive coupling strength of the nanorod array at the lattice constant ($P_y$) of 1100 nm is more significant than those of other lattice constants. This is because the lattice constant of 1100 nm is close to the critical grating constant. If the lattice constant of the nanorod array satisfies the critical grating constant, a much stronger diffractive coupling between the dipoles can be achieved. Otherwise, a weaker coupling between the dipoles is obtained. Here, we will calculate the critical grating constant. According to the theory, the critical grating constant is given by the equation $\lambda_c = m\lambda_0/(n_1 sin\theta + n_2)$, where $\theta$ is the light incident angle in the medium of refractive index $n_1$, and $n_2$ is the refractive index of the array substrate; $m$ is an integer defining the grating [33]. For nanorod array on the glass substrate illuminated at the normal incident in air, the equation can be simplified to $\lambda_c = \lambda_{LSPR}/n_2$, as the first grating order

is responsible for exciting the lattice resonance. In this case, the critical grating constant is equal to 1102 nm in which the longitudinal mode ($\lambda_{LSPR}$) for a single nanorod is 1686 nm and the refractive index of the glass substrate is 1.53 [33]. Figures 6.4 (a), (c) and (e) display the electric field intensity distributions among three different lattice constants, showing a significant diffractive coupling of dipoles for the lattice constant of 1100 nm (Fig. 6.4 (b)), which matches well with our analysis mentioned above. When the lattice constant of the nanorod array is smaller than the critical grating constant, the grating order is still evanescent, leading to a less efficient diffractive coupling (Fig. 6.4 (a)). On the other hand, more intense diffractive coupling is shown for nanorod array with a larger lattice constant, as shown in (Fig. 6.4 (e)). This is because the first grating order becomes radiative for the whole spectral range of the plasmon band.

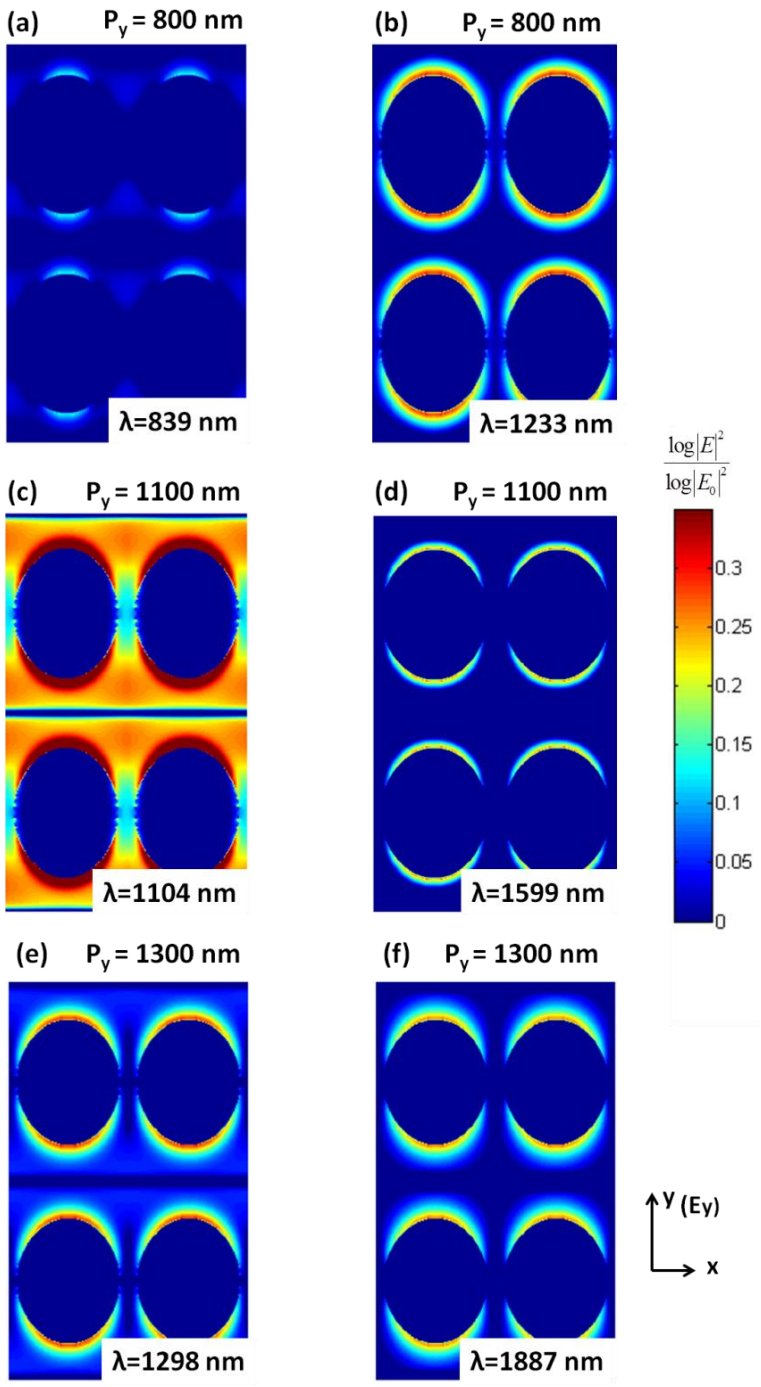


Figure 6.4 Log-scale electric field intensity distributions in the *z*-normal plane at different wavelengths for the lattice resonances ((a) λ = 839 nm, (c) λ = 1104 nm, and (e) λ = 1298 nm) and the dipole resonances ((b) λ = 1233 nm, (d) λ = 1599 nm, and (f) λ = 1887 nm). The lattice constants of the nanorod array are 800 nm for (a) and (b), 1100 nm for (c) and (d), 1300 nm for (e) and (f), respectively.

Figure 6.5 displays the log-scale electric field intensity distributions in the *x*-normal plane cutting through the nanorod at its center. Note that when the lattice constant is tuned smaller than the critical grating constant (1102 nm), the diffractive coupling becomes weaker, but the LSPR dominates (Figs 6.5 (a) and (b)). In contrast, the diffractive coupling between the dipoles becomes dominant when the lattice constant is close to the critical grating constant, while the LSPR is getting weaker (Figs 6.5 (c) and (d)). When the lattice constant is greater than the critical grating constant, the localized electric field intensities of the lattice resonance and LSPR become similar at the edges of the nanorods (Fig. 6.5 (e) and (f)). The difference in the field distributions is that the radiated fields can be observed on the top of nanorods for the lattice resonance (Fig 6.5 (e)). This spatial nature is also observed in the electric field distributions on the *y*-normal plane (Fig. 6.6).

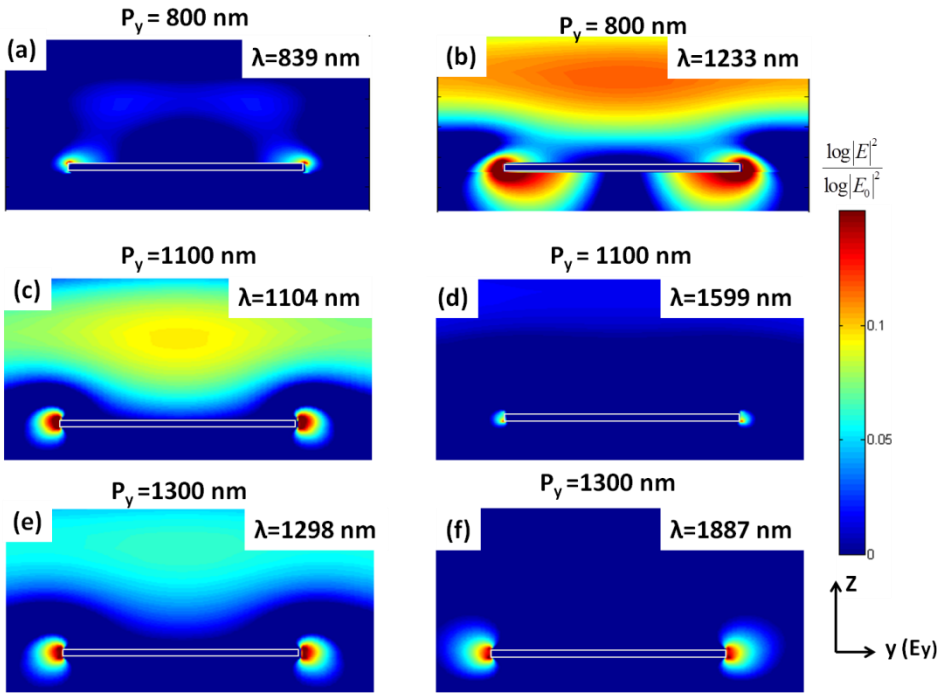


Figure 6.5 Log-scale electric field intensity distributions in the *x*-normal plane cutting through the nanorod center at different wavelengths for the lattice resonances ((a) λ = 839 nm, (c) λ = 1104 nm, and (e) λ = 1298 nm) and the dipole resonance ((b) λ = 1233 nm, (d) λ = 1599 nm, and (f) λ = 1887 nm). The lattice constants for nanorod array are 800 nm for (a) and (b), 1100 nm for (c) and (d), 1300 nm for (e) and (f), respectively.

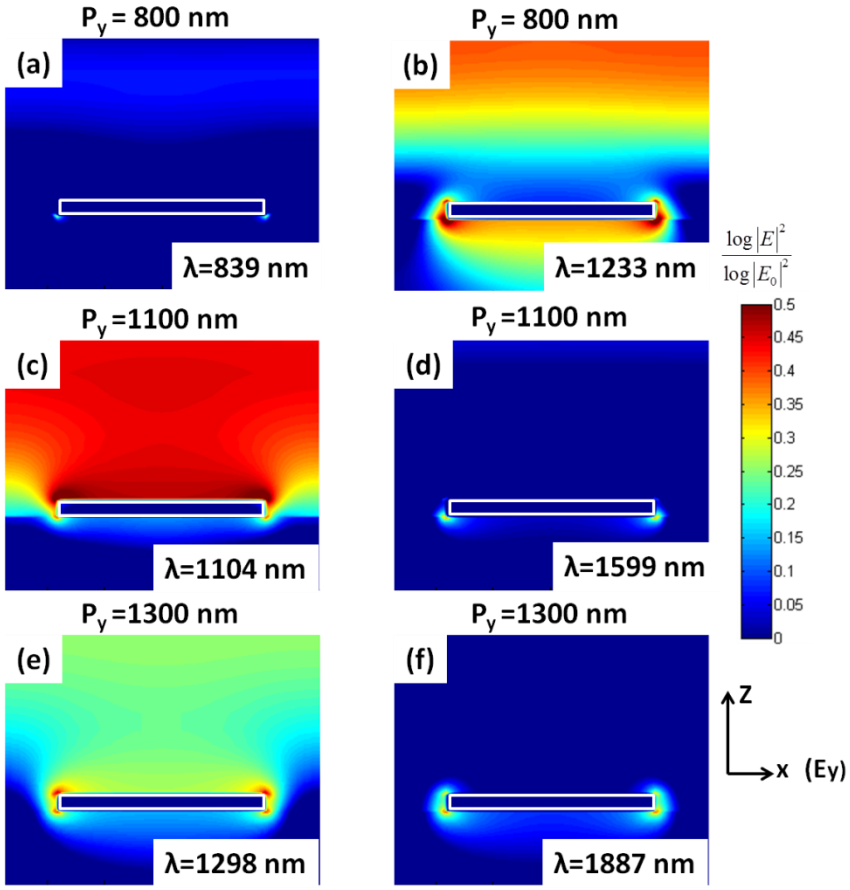


Figure 6.6 Log-scale electric field intensity distributions in the *y*-normal plane cutting through a 130 nm offset from the nanorod center at different wavelengths for the lattice resonance ((a) λ = 839 nm, (c) λ = 1104 nm, and (e) λ = 1298 nm) and the dipole resonance ((b) λ = 1233 nm, (d) λ = 1599 nm, and (f) λ = 1887 nm). The lattice constants for nanorod array are 800 nm for (a) and (b), 1100 nm for (c) and (d), 1300 nm for (e) and (f), respectively.

By comparing the spatial field distributions of the lattice resonance and LSPR among the nanorod array with different lattice constants ($P_y$), it is found that tuning the lattice constants can redistribute near-field energy in the whole plane of the array and extend it into far field.

### 6.2.3. Evaluation of RI sensing performance

From the above discussion, nanorod array with the lattice constant ($P_y$) of 1100 nm produces the most pronounced redistribution of the near field energy with a much larger field concentration in the plane of the nanorods at the lattice resonance wavelength. The delocalized nature of the lattice resonance with a large field intensity distribution between the nanorods is an advantage over LSPR because of the large contact area, thus providing a high possibility for the small molecules to couple with this resonance. Therefore, we focus on the RI sensing performance of nanorod array with a lattice constant ($P_y$) of 1100 nm. The optical response of nanorod array in various refractive indices of the surrounding media is simulated using FDTD. Figure 6.7 displays the simulated transmission spectra of nanorods arrays with a lattice period ($P_y$) of 1100 nm illuminated by normal incident light under a polarization in *y* direction. The refractive indices of the surrounding media are varied from 1 to 1.5 in steps of 0.1.

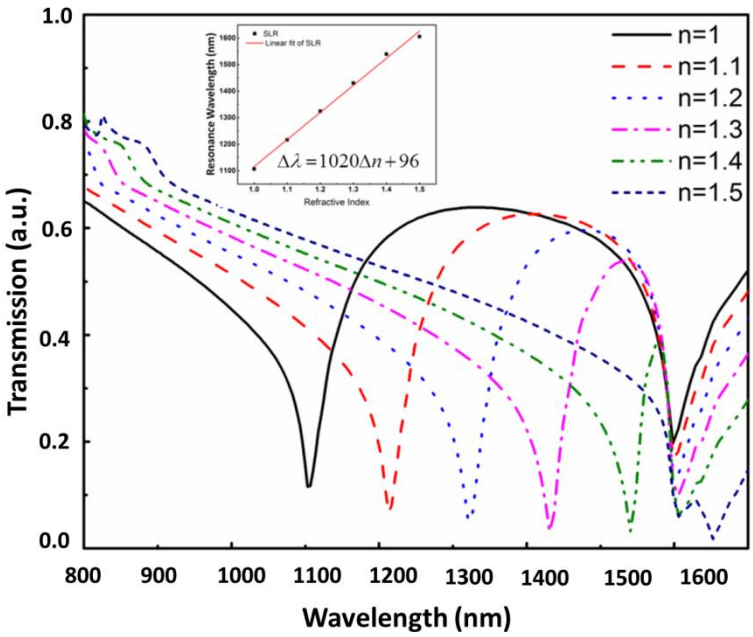


Figure 6.7 Simulated transmission spectra of nanorod array with a lattice constant of 1100 nm in *y* direction and the corresponding RI sensitivity for SLR mode (inset). The dimension of nanorod array is 420×520×30 $nm^3$ with a fixed lattice period of 550 nm in *x* direction.

As seen from Fig. 6.6 (a), the lattice resonance at 1104 nm rapidly shifts towards a longer wavelength with an increase of the refractive index (RI) compared with the LSPR mode at around 1599 nm. After a linear fitting of the resonance shifts based on the variation of the refractive index, the RI sensitivity for the SLR mode is 1020 nm/RIU with the FOM reaching to 24.

## 6.3. Experimental details

### 6.3.1. Fabrication process of nanorod array by LIL

Two-dimensional (2D) gold nanorod array with different lattice constants in *y* direction were prepared by laser interference lithography [31] and lift-off process. During LIL, the sample was exposed twice at two different incident

angles so as to generate nanorod array in a rectangular lattice shape. Tuning the lattice constants of the nanorod array can be achieved by using different incident angles for the second exposure. Therefore, we fabricated two types of nanorod array with the lattice periods of (1) 900 and (2) 1100 nm in *y* direction. For sample (1), the photoresist was exposed for 90 s by the interference patterns under an incident light angle of 17 °. The sample was then rotated by 90 ° on the holder and exposed for 90 s again with an incident light angle of 10 °. For sample (2), the photoresist was exposed following the same parameters for the first exposure of sample (1). At the second exposure, the photoresist was exposed for longer time (120 s) under an incident light angle of 8.5 ° so that the dimension of the individual nanorod was the same for both samples. Figure 6.8 displays the SEM image of these two types of nanorod array with the lattice period in *y* direction of 900 and 1100 nm, respectively. The dimension of nanorod array was $420 \times 520 \times 30$ nm$^3$.

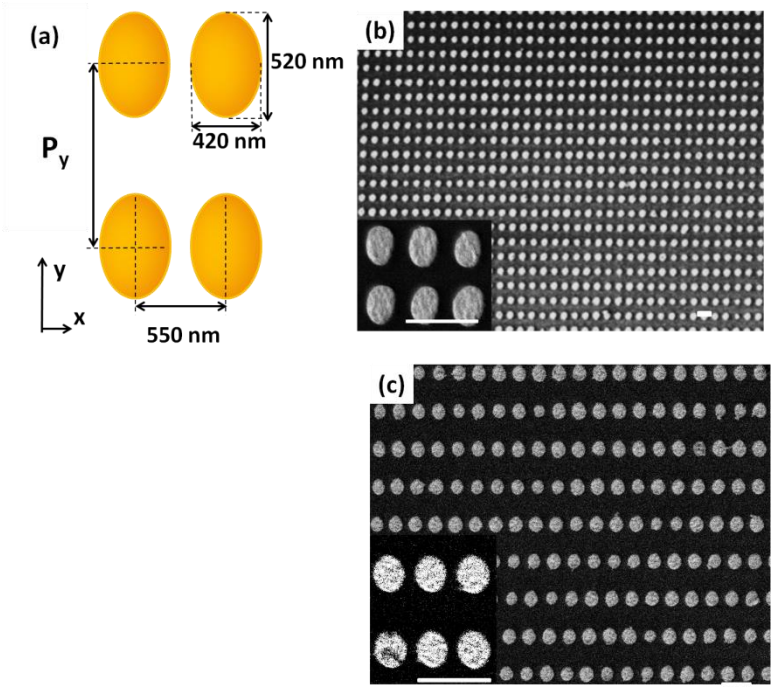


Figure 6.8 (a) Schematic diagram of nanorod array and SEM images of nanorod array with two different lattice constants in *y* direction: (b) $P_y = 900$ nm and (c) $P_y = 1100$ nm. The scale bar is 1 μm.

### 6.3.2. Characterization of the fabricated nanorod array

Far-field transmission spectra of the nanorod array were characterized using the variable angle spectroscopic ellipsometer (V-VASE) at normal incidence. Figure 6.9 shows the measured optical transmission spectra of the two different nanorod arrays under light polarization along *y* direction. The measured spectra were normalized to focus on the spectral shift. Firstly as expected, both nanorod arrays display two different resonance modes: the narrow surface lattice resonance (SLR) located close to the lattice constant $P_y$, and the broad localized surface plasmon resonance (LSPR) positioned at longer wavelengths than the SLR mode. The appearance of the lattice resonance arises from the in-phase addition of the radiation fields of the

neighboring nanorods. This has been confirmed by simulation of the electric field intensities, as shown in Fig. 6.4. Secondly, it is clearly observed that the lattice resonance shifts from 920 to 1130 nm and the LSPR shifts from 1320 to 1650 nm. Correspondingly, the spectral widths of the SLR and LSPR modes are reduced from 159 to 114 nm and 227 to 107 nm, respectively, through fitting of Lorentzian profiles. This demonstrates that the narrow spectral widths for both resonances are decreased with increasing the lattice constant, emphasizing the important role played by the lattice constant of nanorod array.

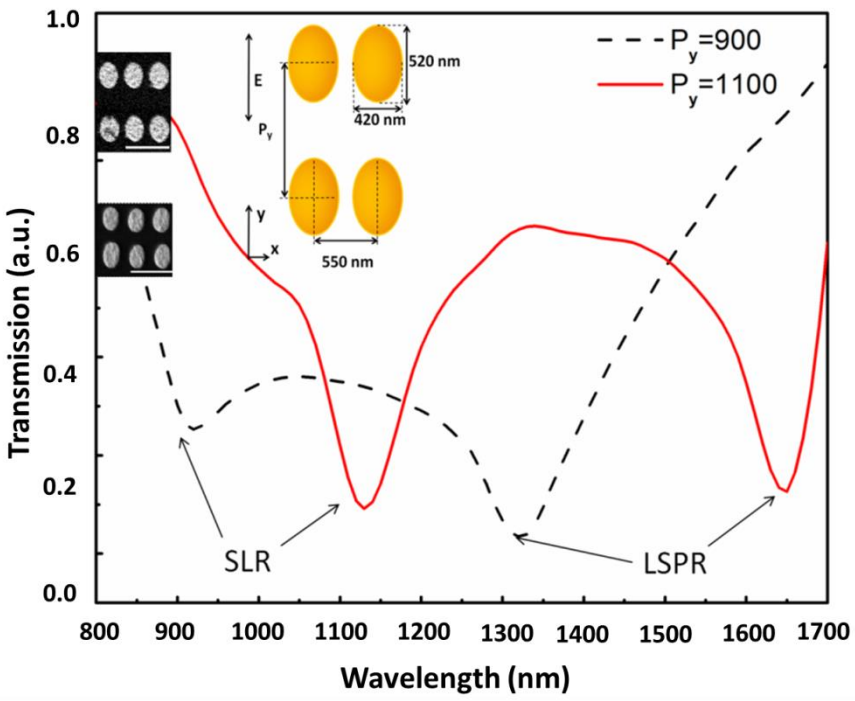


Figure 6.9 Measured optical transmission spectra of gold nanorod array with the lattice constants ($P_y$) of 900 (black dashed line) and 1100 nm (red solid line) under light polarization along *y* direction. The nanorod array has the dimension of 420×520×30 $nm^3$ and a fixed period of 550 nm in *x* direction.

### 6.3.3. Evaluation of RI sensing performance for nanorod array

According to our simulation, the lattice resonance can provide high refractive index sensitivity compared to the localized surface plasmon resonance in an array of nanorods with the lattice constant of 1100 nm along the long axis of the nanorod. The measurement of RI sensitivity for the lattice mode is demonstrated in Fig. 6.10. The sample was immersed inside commercialized liquids with refractive indices of 1.3400, 1.3600 and 1.3700, which was sealed inside a quartz chamber. The whole chamber was placed on the stage of the ellipsometer, and illuminated by normal incident light under light polarization along the long axis of the nanorod. It is clearly observed that the lattice resonance shifts from 1130 nm in air to 1510 nm in the liquid with the refractive index of 1.3700. The refractive index sensitivity is linearly fitted in Fig. 6.10. RI sensitivity and the figure of merit for the lattice resonance are calculated to be 1056 nm/RIU and 9.3, respectively. The working wavelength is at the near infrared, ranging from 1130 to 1550 nm.

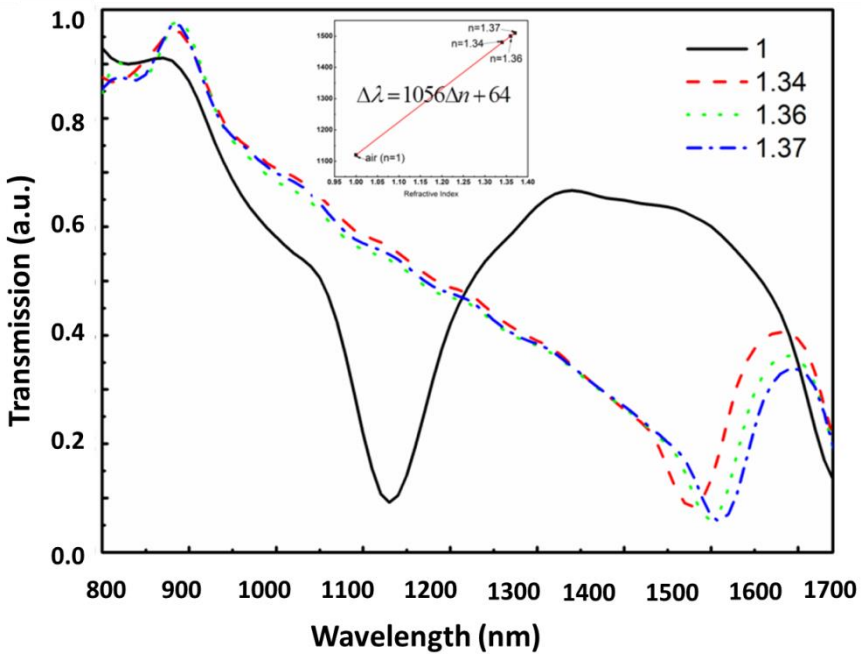


Figure 6.10 Measured optical transmission spectra of nanorod array in different surrounding media at incident polarization along the long axis of the nanorod. RI sensitivity is linearly fitted to the data, giving a RI sensitivity of 1056 nm/RIU for the SLR mode.

### 6.4. Summary

To conclude, we have demonstrated that lattice resonance can be tuned by engineering the lattice constants, due to the strong modification of the diffractive coupling conditions between the dipoles. This result provides for significant improvement in refractive index sensing. Through detailed comparison of the far-field optical properties and near-field enhancements given by three different Au nanorod arrays with different lattice constants, we have revealed that the diffractive coupling strength can be manipulated through a careful choice of the lattice constant. The spatial field distributions of the lattice resonance and LSPR modes have also been studied in three dimensions, providing evidence that the electric fields of the lattice resonance

are concentrated in the plane of the nanorods and near-field energy is extended on the top of the nanorods, leading to strong far-field scattering coupling. Finally, it has been shown that experimentally tuning the lattice resonance can be achieved by patterning nanorod array over a large area through a low-cost and high throughout fabrication tool: laser interference lithography. These fabricated nanorods highlight the crucial role played by the lattice constant of the nanorod array for high RI sensitivity.

### 6.5. References


[1] U. Kreibig and M. Vollmer, *Optical properties of metal clusters*, Springer: Berlin (1995).

[2] J. P. Camden, J. A. Dieringer, J. Zhao, and R. P. Van Duyne, "Controlled plasmonic nanostructures for surface-enhanced spectroscopy and sensing," Acc. Chem. Res. **41**, 1653-1661 (2008).

[3] S. A. Maier and H. A. Atwater, "Plasmonics: localization and guiding of electromagnetic energy in metal/dielectric structures," J. Appl. Phys. **98**, 01101 (2005).

[4] S. J. Lee, Z. Guan, H. Xu, and M. Moskovits, "Surface-enhanced Raman spectroscopy and nanogeometry: the plasmonic origin of SERS," J. Phys. Chem. C **111**, 17985-17988 (2007).

[5] M. J. Banholzer, J. E. Millstone, L. Qin, C. A. Mirkin, "Rationally designed nanostructures for surface-enhanced Raman spectroscopy," Chem. Soc. Rev. **37**, 885 (2008).

[6] F. Le, D. W. Brandl, Y. A. Urzhumov, H. Wang, J. Kundu, N. J. Halas, J. Aizpuruz, P. Nordlander, "Metallic nanoparticle arrays: a common substrate

for both surface-enhanced Raman scattering and surface enhanced infrared absorption," ACS Nano **2**, 707-718 (2008).

[7] J. Zhao, X. Y. Zhang, C. R. Yonzon, A. J. Haes, R. P. V. Duyne, "Localized surface plasmon resonance biosensors," Nanomedicine **1**, 219-228 (2006).

[8] M. Mascini, I. Palchetti and G. Marrazza, "DNA electrochemical biosensros," Fres. J. Anal. Chem. **369**, 15-22 (2001).

[9] K. M. Mayer, and J. H. Hafner, "Localized surface plasmon resonance sensors," Chem. Rev. **111**, 3828-3857 (2011).

[10] H. J. Chen, X. S. Kou, Z. Yang, W. H. Ni, and J. F. Wang, "Shape- and size-dependent refractive index sensitivity of gold nanoparticles," Langmuir **24**, 5233-5237 (2008).

[11] S. L. Teo, V. K. Lin, R. Marty, N. Large, E. A. Lload, A. Arbouet, C. Girard, J. Aizpurua, S. Tripathy, and A. Mlayah, "Gold nanoring timers: a versatile structure for infrared sensing," Opt. Express **18**, 22271-22282 (2010).

[12] N. Verellen, P. V. Dorpe, C. Huang, K. Lodewijks, G. A. E. Vandenbosch, L. Lagae, and V. V. Moshchalkov, "Plasmon line shaping using nanocrosses for high sensitivity localized surface plasmon resonance sensing," Nano Lett. **11**, 391-397 (2011).

[13] A. Lovera, B. Gallinet, P. Nordlander, and O. J. F. Martin, "Mechanisms of fano resonances in coupled plasmonic systems," ACS Nano **7**, 4527-4536 (2013).

[14] G. Das, M. Chirumamilla, A. Toma, A. Gopalakrishnan, R. P. Zaccaria, A. Alabastri, M. Leoncini and E. D. Fabrizio, "Plasmon based biosensor for distinguishing different peptides mutation states," Sci. Rep. **3**, 1792 (2013).

[15] S. A. Maier, P. G. Kik, H. A. Atwater, S. Meltzer, E. Harel, B. E. Koel and A. A. G. Requicha, "Local detection of electromagnetic energy transport below the diffraction limit in metal nanoparticle plasmon waveguides," Nat. Mater. **2**, 229-232 (2003).

[16] V. A. Markel, "Coupled-dipole approach to scattering of light from a one-dimensional periodic dipole structures," J. Mod. Opt. **40**, 2281-2291 (1993).

[17] V. A. Markel, "Divergence of dipole sums and the nature of non-Lorentzian exponentially narrow resonances in one-dimensional periodic arrays of nanospheres," J. Phys. B: At. Mol. Opt. Phys. **38**, L115-L121 (2005).

[18] R. L. Chern, and Y. C. Lan, "Collective modes in metallic photonic crystals with subwavelength grooves," Phys. Rev. B **80**, 033107 (2009).

[19] S. Zou, N. Janel, and G. C. Schatz, "Silver nanoparticle array structures that produce remarkable narrow plasmon lineshapes," J. Chem. Phys. **120**, 10871-10875 (2004).

[20] B. Lamprecht, G. Schider, R. T. Lechner, H. Ditlbacher, J. R. Krenn, A. Leitner, and F. R. Aussenegg, "Metal nanoparticle gratings: influence of dipolar particle interaction on the plasmon resonance," Phys. Rev. Lett. **84**, 4721-4724 (2000).

[21] B. Auguie, and W. L. Barnes, "Collective resonances in gold nanoparticle arrays," Phys. Rev. Lett. **101**, 143902-1 – 143902-4 (2008).

[22] B. Ng, S. M. Hanham, V. Giannini, Z. C. Chen, M. Tang, Y. F. Liew, N. Klein, M. H. Hong, and S. A. Maier, "Lattice resonances in antenna arrays for liquid sensing in the terahertz regime," Opt. Express **19**, 14653-14661 (2011).

[23] G. Vecchi, V. Biannini, and J. G. Rivas, “Shaping the fluorescent emission by lattice resonances in plasmonic crystals of nanoantennas,” Phys. Rev. Lett. **102**, 146807-1 – 146807-4 (2009).

[24] S. R. K. Rodriguez, O. T. A. Janssen, A. Abass, B. Maes, G. Vecchi, and J. G. Rivas, “Opening stop-gaps in plasmonic crystals by tuning the radiative coupling of surface plasmons to diffracted orders,” arXiv:1110.3260v1.

[25] N. Felidj, G. Laurent, J. Aubard, and G. Levi, “Grating-induced plasmon mode in gold nanoparticle arrays,” J. Chem. Phys. **123**, 221103-1 – 221103-5 (2005).

[26] K. T. Carron, W. Fluhr, M. Meier and A. Wokaun, “Resonances of two-dimensional particle grating in surface-enhanced Raman scattering,” J. Opt. Soc. Am. B **3**, 430-440 (1986).

[27] L. Chen, J. T. Robinson, and M. Lipson, “Role of radiation and surface plasmon polaritons in the optical interactions between a nano-slit and a nano-groove on a metal surface,” Opt. Express **14**, 12629-12636 (2006).

[28] H. C. Guo, D. Nau, A. Radke, X. P. Zhang, J. Stodolka, X. L. Yang, S. G. Tikhodeev, N. A. Gippius, and H. Giessen, “Large-are metallic photonic crystal fabrication with interference lithography and dry etching,” Appl. Phys. B **81**, 271-275 (2005).

[29] Y. G. Chen, T. S. Kao, B. Ng, X. Li, X. G. Luo, B. Lukyanchuk, S. A. Maier, and M. H. Hong, “Hybrid phase-change plasmonic crystals for active tuning of lattice resonances,” Opt. Express **21**, 13691-13698 (2013).

[30] B. Auguie, and W. L. Barnes, “Diffractive coupling in gold nanoparticle arrays and the effect of disorder,” Opt. Lett. **34**, 401-403 (2009).

[31] E. D. Palik, “Handbook of optical constants of solid,” Academic Press: Orlando (1985).

[32] V. Giannini, A. I. Fernandez-Dominguez, S. C. Heck, and S. A. Maier, “Plasmonic nanoantennas: fundamentals and their use in controlling the radiative properties of nanoemitters,” Chem. Rev. 111, 3888-3912 (2011).

[33] P. Offermans, M. C. Schaafsma, S. R. K. Rodriguez, Y. Zhang, M. C. Calama, S. H. Brongersma, and J. G. Rivas, “Universal scaling of the figure of merit of plasmonic sensors” ACS Nano **6**, 5151-5157 (2011).

# Chapter 7 Conclusions & Future Work

## 7.1. Conclusions

Three main research topics of plasmonic nanostructures have been investigated. The first one is the design and modeling of metallic nanostructures with straightforward and reproducible parameters. The economical and highly efficient nanofabrication techniques capable of generating plasmonic nanostructures over a large area are investigated. Finally, the potential to apply these nanostructures for plasmonic sensing and spectroscopy is studied.

In previous works, attempts on plasmonic sensing are devoted to generating the sophisticate nanostructures. However, engineering them with low-cost and highly efficient nanofabrication tools over a large area is challenging. To overcome these weaknesses, this thesis has accomplished a number of theoretical and experimental contributions.

- A novel hybrid nanofabrication technique is proposed for the first time. By combining laser interference lithography and thermal annealing, metallic nanodot array with a size of sub-50 nm can be achieved. The fabricated area of plasmonic nanostructures can be as large as a few square centimeters, or even larger if a larger mirror and higher laser power are applied in LIL. The significance of the nanofabrication method, in view of its excellent performance in both efficiency and cost, is that it provides the feasibility to

realize plasmonic nanostructures over a large area with good uniformity, and also to tune their plasmon resonance wavelengths in the UV-visible range.

- The nanodot array fabricated by LIL and thermal annealing can effectively improve the refractive index sensing sensitivity of the surrounding media compared to nanodots formed only by thermal annealing. The sensing ability of nanodot array is increased up to 96% higher than nanodots. This is because the nanodot array has a better uniformity both in terms of size and particle distribution than nanodots. This result provides clear evidence that the fabricated nanodots can be applied potentially refractive index sensors due to the excitation of LSPR and this ability can be further improved if the degree of the randomness of size dimension and particle distribution is reduced.
- Tunable localized surface plasmon resonance of the metallic nanodot array fabricated by LIL and thermal annealing can be experimentally achieved by proper control of the Au concentration of the Ag/Au nanodot array. By tuning the LSPR of nanodot array, the Raman intensity of the molecules R6G on the surface of the $Ag_{0.5}/Au_{0.5}$ nanodot array is increased by two times than those on the surface of the $Ag_{0.75}/Au_{0.25}$ nanodot array. This is because the plasmon resonance wavelength of the first nanodot array well matches with the excitation wavelength of the laser and also overlaps the absorption spectrum of the interested Raman band. This finding demonstrates a simple approach to flexibly tune the LSPR wavelength by controlling the concentration of one of the elements of a bimetallic nanodot structure. The result also provides a guideline to enhance the Raman scattering of other molecules by metallic nanoparticles.

- The diffractive coupling of localized plasmons in an array of nanorods can induce a strong modification in the transmission characteristics, leading to a narrow line shape in the transmission spectrum and strong near-field spatial distribution extending in the plane of the array. This resonance has provided large refractive index sensitivity up to 800 nm/RIU and high figure of merit of 11, as demonstrated in the experiment. One major advantage of our work is the design of nanostructures with straightforward and reproducible parameters as well as the feasibility to realize them over a large area by laser. The fabricated nanostructures can significantly improve the refractive index sensitivity due to the excitation of the surface lattice resonance.
- Tuning the surface lattice resonance has been accomplished by varying the lattice constant of Au nanorod array. Through detailed comparisons of the optical properties and near-field intensity distributions at the plasmon resonance given by three different nanorod arrays, it was shown that the spectral wavelengths of the SLR and LSPR modes can be flexibly tuned in the near infrared range. The refractive index sensitivity for nanorod array with a lattice constant of 1100 nm in *y* direction can be as high as 1000 nm/RIU in the experiment, which is due to good control of the diffractive coupling of dipoles. This finding provides the important insight that the optimized lattice resonance can further enhance refractive index sensing.

### 7.2. Future work

This research has proposed a novel nanofabrication technique and demonstrated the design and fabrication of plasmonic nanostructures over a

large area as well as the feasibility to realize potential applications in plasmonic sensing and Raman spectroscopy. However, there still remain a few challenges for further studies. A brief outlook is given on future work and potential applications to make the most use of the findings inspired by the recent study.

- **Refractive index sensing for the real-time detection of bio/chemical molecules**

With regarding to plasmonic sensing, especially for refractive index sensing, it has been demonstrated in this thesis that plasmonic nanostructures can be used to detect the refractive index change of the surroundings. It would be interesting to extend this technique for the real-time detection of the bio/chemical molecules [1]. This can be achieved by developing a micro-fluidic detection system with our plasmonic sensors [2], leading to quantitatively analysis of the concentration of the molecules or the interactions between the molecules and sensors. It is believed that these efforts will make great contributions to applications such as the quantification of environmental pollutants [3], medical research [4], diagnostics [5], drug discovery [6] and fundamental molecular biology studies [7].

- **Photocurrent enhancements with a periodic array of metallic nanostructures**

In this thesis, it has been demonstrated that nanodots or nanodot array can localize the light at the nanoscale, well below the scale of the light wavelength in free space. It would be interesting to design a new solar-cell based on plasmonics and photovoltaics [8]. Plasmonic nanostructures can be used to

improve the absorption in photovoltaic devices [9], allowing a considerable reduction in the physical thickness of solar photovoltaic absorber layers.

- Fluorescence imaging with an array of nanorods

It has been demonstrated that a periodic array of nanorods can provide strong field enhancement and narrow spectral shape, arising from the excitation of SLR induced by the diffractive coupling of dipoles. It would be an interesting area for future research, using this method to enhance fluorescence imaging [10]. The emission light of the fluorescent molecules could be strongly modified by placing them at suitable distances from a periodic array of nanorods, owing to the fact that the radiative decay rates of the molecules are modified by plasmonic nanostructures [11]. As a result, the emission rate and the quantum yield of the fluorescent molecules will be increased.

### 7.3. References

[1] H. D. Song, I. Choi, S. Lee, Y. I. Yang, T. Kang and J. Yi, "On-chip colorimetric detection of $Cu^{2+}$ ions via density-controlled plasmonic core-satellites nanoassembly," Annal. Chem. **85**, 7980-7986 (2013).

[2] S. Y. Lee, G. F. Walsh, and L. D. Negro, "Microfluidics integration of aperiodic plasmonic arrays for spatial-spectral optical detection," Opt. Express **21**, 4945-4957 (2013).

[3] P. H. Rogers, G. Sirinakis and M. A. Carpenter, "Plasmonic-based detection of $NO_2$ in a harsh environment," J. Phys. Chem. C **112**, 8784-8790 (2008).

[4] J. Z. Zhang, “Biomedical applications of shape-controlled plasmonic nanostructures: a case study of hollow gold nanospheres for photothermal ablation therapy of cancer,” J. Phys. Chem. Lett. **1**, 686-695 (2010).

[5] J. Hottin, J. Moreau, G. Roger, J. Spadavecchia, M. Millot, M. Gossens, M. Canva, “Plasmonic DNA: toward genetic diagnosis chips,” Plasmonics **2**, 201-215 (2007).

[6] W. K. Fong, T. L. Hanley, B. Thierry, N. Kirby, and B. J. Boyd, “Plasmonic nanorods provide reversible control over nanostructure of self-assembled drug delivery materials,” Langmuir **26**, 6136-6139 (2010).

[7] V. López-Puente, S. Abalde-Cela, P. C. Angelomé, R. A. Alvarez-Puebla, and L. M. Liz-Marzán, “Plasmonic mesoporous composites as molecular sieves for SERS detection,” J. Phys. Chem. Lett. **4**, 2715-2720 (2013).

[8] N. P. Hylton, X. F. Li, V. Giannini, K. H. Lee, N. J. Ekins-Daukes, J. Loo, D. Vercuysse, P. Van Dorpe, H. Sodabanlu, M. Sugiyama, and S. A. Maier, “Loss mitigation in plasmonic solar cell aluminum nanoparticles for broadband photocurrent enhancements in GaAs photodiodes,” Sci. Rep. **3**, 2874 (2013).

[9] B. Lamprecht, G. Schider, R. T. Lechner, H. Ditlbacher, J. R. Krenn, A. Leitner, and F. R. Aussenegg, “Metal nanoparticle gratins: influence of dipole particle interaction on the plasmon resonance,” Phys. Rev. Lett. **84**, 4721-4724 (2000).

[10] F. Tam, G. P. Goodrich, B. R. Johnson, and N. J. Halas, “Plasmonic enhancement of molecular fluorescence,” Nano Lett. **7**, 496-501 (2007).

[11] O. L. Muskens, V. Giannini, J. A. Sánchez-Gil, and J. G. Rivas, “Strong enhancement of the radiative decay rate of emitters by single plasmonic nanoantennas,” Nano Lett. **7**, 2817-2875 (2007).